N69-16689

NASA CR-99218

NATIONAL AERONAUTICS AND SPACE ADMINISTRATION

Space Programs Summary 37-53, Vol. II

The Deep Space Network

For the Period July 1 to August 31, 1968

JET PROPULSION LABORATORY
CALIFORNIA INSTITUTE OF TECHNOLOGY
PASADENA, CALIFORNIA

September 30, 1968

NATIONAL AERONAUTICS AND SPACE ADMINISTRATION

Space Programs Summary 37-53, Vol. II

The Deep Space Network

For the Period July 1 to August 31, 1968

JET PROPULSION LABORATORY
CALIFORNIA INSTITUTE OF TECHNOLOGY
PASADENA, CALIFORNIA

September 30, 1968

SPACE PROGRAMS SUMMARY 37-53, VOL. II

Prepared Under Contract No. NAS 7-100
National Aeronautics & Space Administration

Preface

The Space Programs Summary is a multivolume, bimonthly publication that presents a review of technical information resulting from current engineering and scientific work performed, or managed, by the Jet Propulsion Laboratory for the National Aeronautics and Space Administration. The Space Programs Summary is currently composed of four volumes:

Vol. I. *Flight Projects* (Unclassified)

Vol. II. *The Deep Space Network* (Unclassified)

Vol. III. *Supporting Research and Advanced Development* (Unclassified)

Vol. IV. *Flight Projects and Supporting Research and Advanced Development* (Confidential)

Page intentionally left blank

Contents

Contents (contd)

I. Introduction

A. Description of the DSN

The Deep Space Network (DSN), established by the NASA Office of Tracking and Data Acquisition under the system management and technical direction of JPL, is responsible for two-way communications with unmanned spacecraft traveling approximately 10,000 mi from earth to interplanetary distances. It supports, or has supported, the following NASA deep space exploration projects: *Ranger, Surveyor, Mariner* Venus 1962, *Mariner* Mars 1964, *Mariner* Venus 67, and *Mariner* Mars 1969 (JPL); *Lunar Orbiter* (Langley Research Center); *Pioneer* (Ames Research Center); and *Apollo* (Manned Spacecraft Center), as backup to the Manned Space Flight Network (MSFN). The DSN is distinct from other NASA networks such as the MSFN, which has primary responsibility for tracking the manned spacecraft of the *Apollo* Project, and the Space Tracking and Data Acquisition Network (STADAN), which tracks earth-orbiting scientific and communications satellites.

The three basic functions performed by the DSN in support of each flight project are as follows:

(1) *Tracking.* Accomplished by radio communication with the spacecraft, tracking provides such metric data as angles, radial velocity, and range (distance from the earth to the spacecraft).

(2) *Data acquisition.* Using the same radio link, the data acquisition function consists of the recovery of information from the spacecraft in the form of telemetry, namely, the engineering measurements recorded by the spacecraft and the scientific data obtained by the onboard instruments.

(3) *Command.* Using the same radio link, the command function involves sending information to the spacecraft to initiate equipment which, for example, operates propulsion systems for changing the trajectory of the spacecraft, changes data transmission rate to earth, or reprograms onboard computers which determine the sequence of spacecraft engineering events.

The DSN can be characterized as a set of the following systems: (1) telemetry, (2) tracking, (3) command, (4) monitoring, (5) simulation, and (6) operations control. Alternately, it can be considered as being comprised of three facilities: the Deep Space Instrumentation Facility (DSIF), the Ground Communications Facility (GCF), and the Space Flight Operations Facility (SFOF).

The DSIF is a worldwide set of deep space stations (DSSs) that provide basic radio communications with spacecraft. These stations and the deep space communications complexes (DSCCs) they comprise are as follows:

Pioneer, Echo, and Mars DSSs (and Venus DSS, described later), comprising the Goldstone DSCC in California; Woomera, Tidbinbilla, and Booroomba[1] DSSs, comprising the Canberra DSCC in Australia; Johannesburg DSS in South Africa; and Robledo, Cebreros, and Rio Cofio[1] DSSs, comprising the Madrid DSCC in Spain. The overseas stations are normally staffed and operated by government agencies of the respective countries, with some assistance from U.S. support personnel.

In addition, the DSIF operates a compatibility test station at Cape Kennedy, which is used for verifying flight-spacecraft/DSN compatibility prior to launch, and a flight-project/tracking and data system interface laboratory at JPL, which is used during the development of the spacecraft to assure a design compatible with the network. A spacecraft guidance and command station on Ascension Island serves to track the spacecraft in the latter part of the launch trajectory while the spacecraft is relatively low in altitude.

To enable continuous radio contact with spacecraft, the stations are located approximately 120 deg apart in longitude; thus, a spacecraft in flight is always within the field-of-view of at least one station, and for several hours each day may be seen by two stations. Furthermore, since most spacecraft on deep space missions travel within 30 deg of the equatorial plane, the stations are located within latitudes of 45 deg north or south of the equator.

Radio contact with a spacecraft usually begins when the spacecraft is on the launch vehicle at Cape Kennedy, and it is maintained throughout the mission. The early part of the trajectory is covered by selected network stations of the Air Force Eastern Test Range (AFETR) and selected stations of the MSFN which are managed by Goddard Space Flight Center. Normally, two-way communications are established between the spacecraft and the DSN within 30 min after spacecraft injection into lunar, interplanetary, or planetary flight. The Cape Kennedy DSS, having supported the preflight compatibility tests, monitors the spacecraft continuously during the launch phase until it passes over the local horizon. The deep space phase begins with acquisition by either the Johannesburg, Woomera, or Tidbinbilla DSS. These stations, with large antennas, low-noise phase-lock receiving systems, and high-power transmitters, provide radio communications to the end of the flight. By international agreement, the radio frequencies assigned for these functions are 2290–2300 MHz for spacecraft-to-earth downlink data transmission and 2110–2120 MHz for earth-to-spacecraft command and uplink data transmission.

To maintain a state-of-the-art capability, research and advanced development work on new components and systems has been conducted continuously at JPL since the establishment of the DSN. To support this work, the Goldstone DSCC has a research and development facility designated the Venus DSS, at which the feasibility of new equipment and techniques to be introduced into the operational network is demonstrated. When a new piece of equipment or new technique has been accepted for integration into the network, it is classed as Goldstone duplicate standard (GSDS), thus standardizing the design and operation of identical items throughout the network.

The GCF, using, in part, facilities of the worldwide NASA Communications Facility (NASCOM, managed and directed by the Goddard Space Flight Center), provides voice, high-speed data, and teletype communications between all stations of the network. Communications between the Goldstone DSCC and the SFOF are provided by a microwave system leased from common carriers. This microwave link has made possible the transmission, in real time, of video data received at the Goldstone DSCC to the SFOF and then to commercial TV systems, as was done during the *Ranger* and *Surveyor* missions.

The SFOF, located at JPL, receives data from all of the tracking stations and processes that information required by the flight project to conduct flight operations. Voice and data channels are distributed throughout the facility, and the following equipment and services are provided: (1) data-processing equipment for the real-time handling and display of tracking and telemetry data; (2) real-time and non-real-time telemetry processing; (3) simulation equipment for flight projects, as well as for network use in training of personnel; (4) monitoring equipment for evaluation of network performance in near-real time; (5) operations control consoles and status and operational display facilities required for the conduct of flight operations; and (6) technical areas for flight project personnel who analyze spacecraft performance, trajectories, and generation of commands, as well as support services required to carry out those functions, such as internal communications by telephone, intercom, public address, closed-circuit TV, documentation, and

---

[1] Not yet authorized.

reproduction of data packages. The SFOF is equipped to support many spacecraft in flight and those under test in preparation for flight; e.g., over a 24-h period during 1967, as many as eight spacecraft in flight or in operational-readiness tests for flight were supported by the SFOF.

Thus, the DSN simultaneously conducts research and development for support of future flight projects, implements demonstrated capabilities for support of the more immediate flight projects, and provides direct support for the currently active missions, while accommodating differences in the individual projects. In this and future issues of the SPS, Vol. II, the current technical activities of the DSN in these three general categories will be reported under the following subject areas:

- Introduction
  - Description of the DSN
  - Description of DSN Systems
- Mission Support
  - Introduction
  - Interplanetary Flight Projects
  - Planetary Flight Projects
  - Manned Space Flight Project
- Advanced Engineering
  - Tracking and Navigational Accuracy Analysis
  - Communications System Research
  - Tracking and Data Acquisition Elements Research
  - Supporting Research
- Network Development and Operations
- Facility Development and Operations
  - Space Flight Operations Facility
  - Ground Communications Facility
  - Deep Space Instrumentation Facility
- Design and Implementation of Technical Structures and Utilities

In the section entitled "Description of DSN Systems," the status of recent developments for each of the six DSN systems listed above will be described. The more fundamental research carried out in support of the DSN is reported in Vol. III of the SPS, and JPL flight project activities for missions supported by the DSN are reported in Vol. I.

B. Description of DSN Systems: Monitoring System, *R. W. Linnenkohl*

1. Functions

The DSN monitoring system consists of those elements of the DSN that provide monitoring data for the real-time evaluation and permanent recording of the performance, configuration, and status of the active DSN physical systems. The general functions performed to provide these data are data collection, transmission, processing, display, and analysis. The monitoring system is constrained to not interrupt the normal track, command, and telemetry data flow to the users. Installation of the DSN interim monitoring system, phase I, is nearing completion, at which time system tests will be performed. The anticipated system configuration for the *Mariner* Mars 1969 missions is shown in Fig. 1.

2. System Elements

The monitoring system is composed of a monitor and control subsystem for each facility (DSIF, GCF, and SFOF) and a DSN monitor area subsystem in the SFOF. The hardware and software of the DSIF that are part of, or contribute significantly to the operation of, the DSN monitoring system are:

(1) Digital instrumentation subsystem, phase II (DIS II).

(2) Station monitor console, phase II (SMC II).

(3) DSIF monitor program, phase I, within DIS II.

(4) All object subsystems (i.e., those instrumented to report to the monitoring system).

Those of the GCF are:

(1) Teletype and high-speed data lines of NASCOM.

(2) GCF monitor program within the SFOF communications processor (CP).

(3) DSIF/GCF and SFOF/GCF interface equipment.

Those of the SFOF are:

(1) IBM 7044 input/output computer.

(2) IBM 7044 mission-dependent processor.

(3) Display buffer.

(4) IBM 7094 criteria-generation program.

(5) Input/output and display devices.

3. System Operation/Subsystem Description

a. DSIF monitor and control subsystem. The DIS II samples analog and digital signals and converts the analog signals to digital form. In identifying and processing station data, such functions as scaling, editing, normalizing, formatting, data comparison, and limit monitoring are performed. The data processing function requires the determination of subsystem performance through comparison with predicted data, validation of the system operating configuration, and identification of subsystem failures by limit-checking against predicted data values. Subsystem performance indices are computed, and data messages for overall mission monitoring are assembled.

A recording is made of station performance history and calibration data in digital form on magnetic tape. Capabilities for generation of a printer record of selected station parameters and for playback are provided. Monitor criteria data are received from the DSN monitor area subsystem. These data are labelled to facilitate playback and data retrieval. The DSIF monitor criteria data consist of critical-parameter limit conditions, tracking data predictions, station performance criteria, system conditions, and system configuration specifications.

The SMC II and interfacing subsystems supply inputs of interrupts and sense switches. The DIS II output data are provided to the paper tape punch, console electric typewriter, monitor printer, high-speed data line printer, subsystem console displays, audible and visible alarm systems, graph plotters, and station monitor displays for the recording and display of subsystem performance data.

Teletype-compatible and high-speed data are formatted and transmitted to the SFOF through the GCF. These data include subsystem performance indices and subsystem operational status.

b. GCF monitor and control subsystem. Error signals are acquired from the automatic data switching system (ADSS) decoders in the SFOF. The CP senses the presence of incoming blocks on a per-circuit basis (via the decoders). An activity indication is generated only if: (1) the total number of blocks during a specified interval exceeds a predetermined minimum, and (2) the CP program has been properly loaded. (If the latter condition is not satisfied, an operator alarm is generated.) Given the required input data, the CP calculates the reciprocal of the error ratio (i.e., the number of good bits divided by the number of erroneous bits). If this ratio does not exceed a predetermined minimum (specified on a per-DSS per-pass basis), an alarm is generated. Input criteria for this alarm generation is either directly from the IBM 7044 monitor program using the 40.8-kbits/s channel or from an operator manual input. (The IBM 7044 inputs override the manual inputs.) The activity indication, calculated error rate, and alarms are forwarded on a per-DSS basis to the IBM 7044 DSN monitor program.

Communications displays are generated in video form for distribution using the SFOF closed-circuit television system. The display generator utilizes timing signals provided by the television system and provides a noncomposite video output of the above data suitable for direct insertion into the television-system switcher.

c. SFOF monitor and control subsystem. Error signals are acquired from the data processing subsystem (DPS) instrumentation and from telemetry and tracking data processing software. The SFOF monitor and control subsystem (basically a modified version of the existing data processing control console) can operate either as a part of the DSN monitoring system or independently. In either case, a complete set of SFOF configuration, status, and alarm data is presented on this subsystem's displays; a compressed set is available for the DSN monitor area subsystem's displays. Operation is independent of the content of mission data to the maximum possible extent.

An equipment status display shows the interconnections and status of the various pieces of DPS equipment. The information is used to: (1) warn operational personnel of actual or impending failures, (2) aid in failure isolation, (3) facilitate rapid recovery from failures, (4) aid in evaluating the validity of DPS outputs, and (5) aid in control of the DPS under standard and non-standard conditions. All data (including out-of-tolerance measurements) are displayed in an on/off manner. A subset of measurements that is of an alarm nature results in an input to the overall DSN monitoring system.

The primary source of information for the processing status and data status displays is the SFOF monitor program. The data status display is a real-time display in tabular format showing the status of all teletype and high-speed data entering the DPS. There is one such display for each IBM 7044-7094 string. All data are identified, data being processed are noted, and alarm conditions in the data format are signaled.

The processing status display is a data-flow-diagram type of display. All significant IBM 7044 processing events from input to output are noted in real time. Data flow paths in use are evident, and blockages in data flow are easily isolated. A single set of indicators is provided to identify the current operating program. There is one processing status display switchable to any IBM 7044-7094 string.

One administrative printer per IBM 7044-7094 string is located in the data processing control area as part of

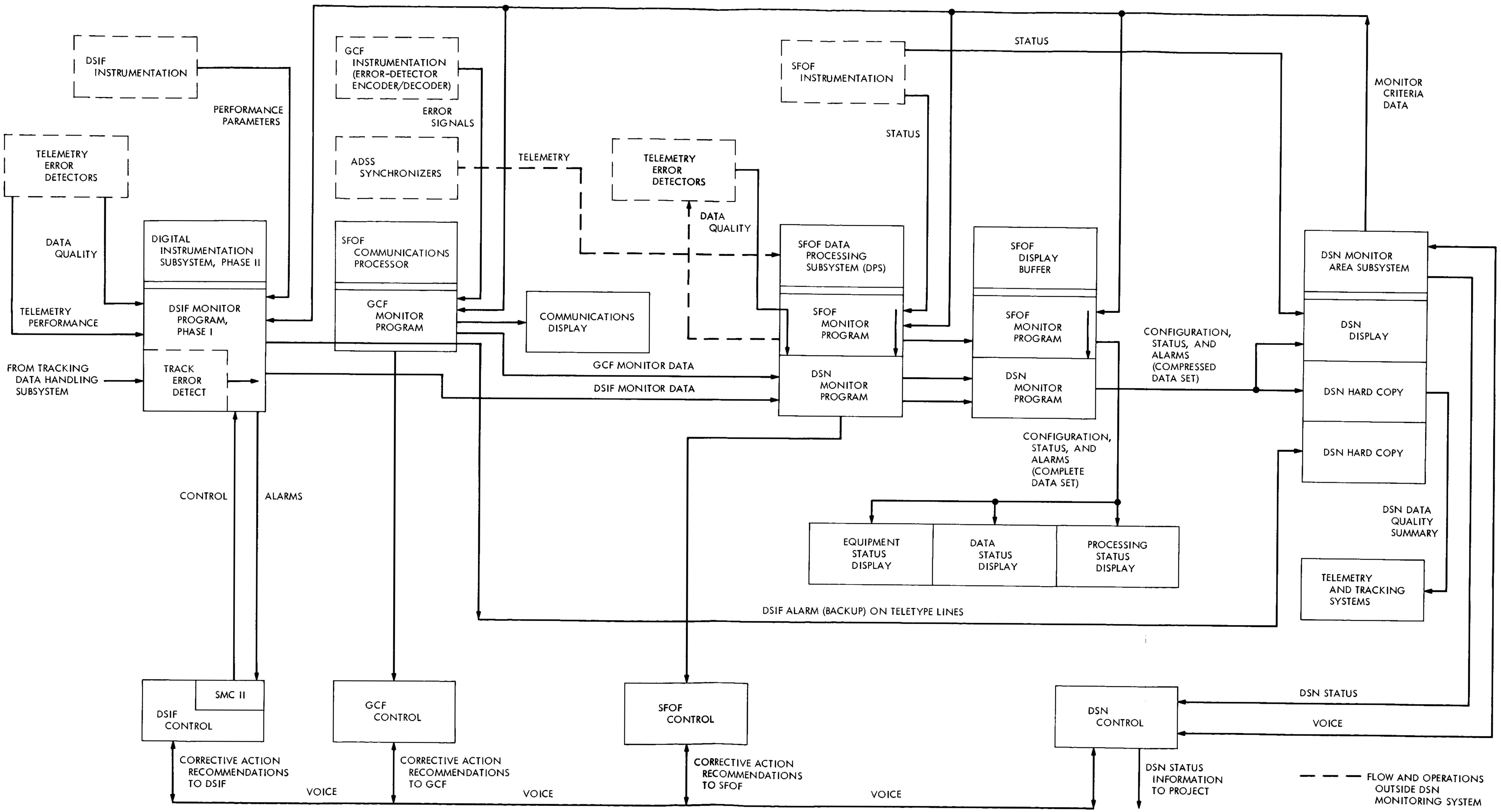

Fig. 1. DSN monitoring system

Page intentionally left blank

the SFOF monitor and control subsystem. This printer indicates the existence of program-detected failures, improper interfacing of computers, and inoperable or incorrectly configured critical pieces of equipment.

d. DSN monitor area subsystem. The major elements of the DSN monitor area subsystem are the DSN monitor area with its associated hardware elements, a DSN monitor and analysis team, and the DSN monitor area subsystem software in the IBM 7044 input/output computer and the display buffer. The monitor area, located in the SFOF, utilizes monitor data outputs from the DSN monitor and control subsystems; hence, it is the primary user subsystem for data processed and provided for overall DSN performance monitoring.

Data monitoring and data validation capabilities are also provided for use by the telemetry and tracking systems. Telemetry data monitoring is accomplished primarily by format checking or by performing continuous measurements on the number of successfully decommutated telemetry frames in the DPS. Tracking data evaluation is performed based on tracking data noise measurements and through comparison of observables with predictions transmitted to the DSN monitor area subsystem.

The input/output computer and the display buffer play a major role in the function of the DSN monitor area subsystem. The input/output computer contains the DSN monitor program for recording, minimal formatting, and outputting to the display buffer all monitor data from the DSIF, GCF, and SFOF monitor and control subsystems and for outputting to printers for monitor data alarms. The display buffer contains the software for driving the monitor area displays (Fig. 1). Monitor criteria data are controlled and provided by the DSN monitor area subsystem.

Page intentionally left blank

II. Advanced Engineering: Tracking and Navigational Accuracy Analysis

A. Introduction, *T. W. Hamilton and D. W. Trask*

The DSN Inherent Accuracy Project was formally established by the DSN Executive Committee in July 1965. The objectives of the project are:

(1) Determination (and verification) of the inherent accuracy of the DSN as a radio navigation instrument for lunar and planetary missions.

(2) Formulation of designs and plans for refining this accuracy to its practical limits.

Achievement of these goals is the joint responsibility of the Telecommunications and Systems Divisions of JPL. To this end, regular monthly meetings are held to coordinate and initiate relevant activities. The project leader and his assistant (from the Systems and Telecommunications Divisions, respectively) report to the DSN Executive Committee, and are authorized to task project members to (1) conduct analyses of proposed experiments, (2) prepare reports on current work, and (3) write descriptions of proposed experiments. The project is further authorized to deal directly with those flight projects using the DSN regarding data-gathering procedures that bear on inherent accuracy.

The various data types and tracking modes provided by the DSIF in support of lunar and planetary missions are discussed in SPS 37-39, Vol. III, pp. 6–8. Technical work directly related to the Inherent Accuracy Project is presented in SPS 37-38, Vol. III, and in subsequent *Deep Space Network* SPS volumes, and is continued in the following sections of this chapter.

The correlations between major visible lunar features and systematic variations in the radio tracking data obtained from *Lunar Orbiter III* are reported in SPS 37-52, Vol. II, pp. 20–24. The analysis has been extended in the following *Section B* to supply a qualitatively consistent gravimetric map of the lunar nearside by processing a doppler data sample that spans a 10-day period with 80 consecutive orbits of the *Lunar Orbiter V*. While this extended analysis is still preliminary and a simplified model was employed, the results reveal large mass concentrations beneath the center of all five nearside ringed maria. In addition, there exists one other mass concentration that probably represents an ancient ringed maria, which has become partially obliterated with the passage of time.

Generally, reductions from earth-satellite tracking data result in high correlations between the gravitational mass of the earth ($GM_\oplus$) and the scale of the coordinate system (i.e., linear coordinates of the tracking stations). This is especially true in the case of optical data that relies on an independent determination of $GM_{\oplus}$ to provide the scale of quantities that involve linear dimensions. To date, the most accurate $GM_{\oplus}$ determinations have been provided from radio tracking of deep space probes such as those reported in SPS 37-43, Vol. III, pp. 3–18 and SPS 37-44, Vol. III, pp. 11–28. At present, these $GM_{\oplus}$ determinations from deep space probe data have no close competitors in that their claimed uncertainty is an order of magnitude less than that provided by previous techniques.

Section C investigates the feasibility of checking the deep space probe results by determining a $GM_{\oplus}$ of competitive accuracy as a check through tracking a medium-altitude satellite with a tracking system comparable to that used for the deep space probes. For the case investigated, which is a high-inclination orbit similar to the one planned for the LIDO project, $GM_{\oplus}$ solutions comparable in accuracy to those obtained from a lunar or planetary flight can be obtained if high-precision ranging data is taken. Furthermore, these solutions are obtained after only 3–4 orbits, thus minimizing the effect of long-term systematic errors such as atmospheric drag, solar-radiation pressure, altitude control thrust, etc.

The systematic trends of 1 mm/s amplitude in the doppler residuals for *Surveyor VII* having a diurnal signature were presented in SPS 37-51, Vol. II, pp. 42–50. This amplitude is significant when compared to the 0.1 mm/s noise normally visible on doppler data sampled once per minute. The suspected causes include lunar ephemeris errors, tropospheric refraction, and ionospheric charged particle effects where the first two are discussed in SPS 37-51, Vol. II. *Section D* further investigates the role played by the ionosphere. Based on electron-content data available from the Faraday rotation experiment being performed at Stanford University, the corrections to doppler data were computed for a 2-wk doppler tracking period during the postlunar touchdown phase of *Surveyor V*. These corrections exceed the uncorrected doppler residuals 2 or 3 fold indicating that the least-squares minimization technique used to fit the *Surveyor* doppler data is providing erroneous DSS and *Surveyor* location solutions.

Section E analyzes the continuous estimation of the state of a distant spacecraft being perturbed by a random acceleration such as would be expected during a low thrust or continuous propulsion mission. The presence of the continuously operating propulsion device in the spacecraft system gives rise to large random non-gravitational forces that influence the trajectory and, hence, the DSN tracking data. These forces result primarily from errors in the thrust and performance; i.e., errors in the magnitude of the thrust and in the thrust direction orientation. *Section E* is concerned with a comprehensive study of the accuracy of state-estimation techniques for powered-flight trajectories and is an extension of the work reported in SPS 37-52, Vol. II, pp. 37–44, which ignored these random accelerations. As before, empirical formulas are presented that are accurate for reasonable lateral velocities and valid up to about 10 successive passes of data when the probe is relatively free from planetary gravitational forces and at an appreciable distance from the sun.

Section F discusses data compression and its application to orbit determination. A technique is described that substantially reduces the amount of data that must be handled without significantly reducing the information contained in the data. Simulated data corresponding to realistic spacecraft missions are processed both in the SPODP and via this data compression technique; the resulting covariance matrices were compared and found to be in good agreement.

B. Mascons: Lunar Mass Concentrations,[1]

P. M. Muller and W. L. Sjogren

1. Introduction

The *Lunar Orbiter* missions have provided both high-quality photographs of the moon and supplementary scientific information concerning the moon's gravitational field. Previous investigators concluded that the moon is gravitationally rougher than anticipated in the sense that comparatively high degree terms in the spherical harmonic expansion would be required for effective representation of the gravity field (Refs. 1–4). This roughness of the moon has been of interest to the *Apollo* Project because of the resulting perturbations on the *Apollo* orbiting spacecraft. For these reasons, a new analysis has been made using the accurate radio tracking data provided by the NASA Deep Space Network (DSN) operated by the Jet Propulsion Laboratory.

This new processing (Ref. 5) of the *Lunar Orbiter* data has produced unexpected results. A study of local accelerations on the spacecraft resulted in a gravipotential map (Fig. 1) of the lunar nearside that reveals very large mass concentrations (mascons) beneath the center of all five nearside ringed maria (Imbrium, Serenitatis, Crisium, Nectaris and Humorum). In addition, mascons were

---

[1] This subject has also been reported in *Science*, Vol. 161, No. 3842, pp. 681–684, Aug. 16, 1968.

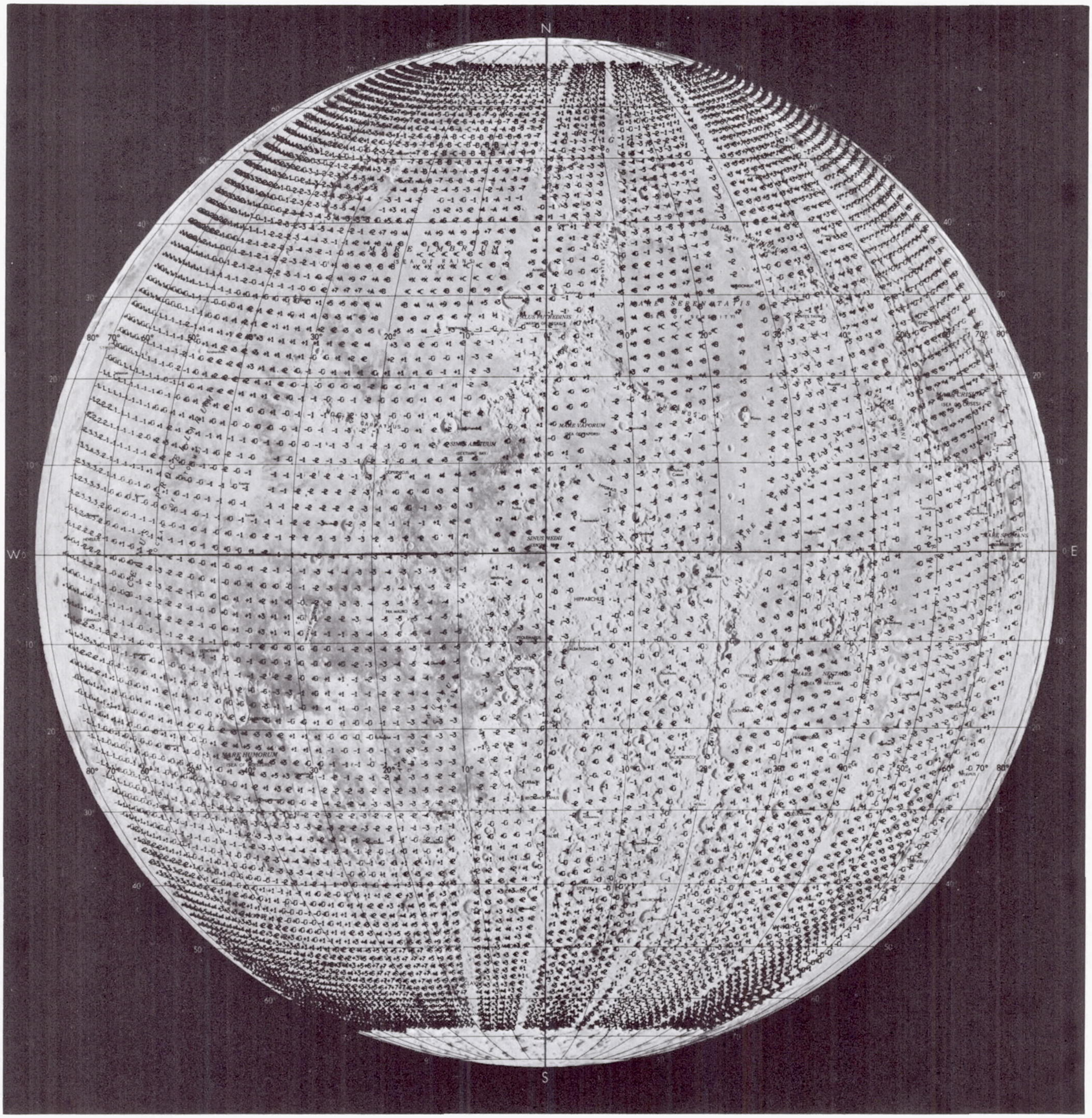

RANGE	SYMBOL	RANGE	SYMBOL	RANGE	SYMBOL
BEYOND ±20	±X	±7.5 to ±8.5	±8	±2.5 to ±3.5	±3
±15 to ±20	±C	±6.5 to ±7.5	±7	±1.5 to ±2.5	±2
±11.5 to ±15	±B	±5.5 to ±6.5	±6	±0.5 to ±1.5	±1
± 9.5 to ±11.5	±A	±4.5 to ±5.5	±5	0.0 to +0.5	+0
± 8.5 to ± 9.5	±9	±3.5 to ±4.5	±4	−0.5 to 0.0	−0

NOTE: RANGE ABOVE × 0.1 = mm/s^2; ABOVE × 10 = mgal. THESE SCALING FACTORS ALSO APPLY TO FIG. 2.

Fig. 1. Gravimetric and acceleration map of the lunar nearside

observed in the area between Sinus Aestuum and Sinus Medii (presumably a newly discovered ancient ringed mare), and in the Mare Orientale. The Urey–Gilbert theory of lunar history (Ref. 6) has predicted such large-scale high-density mascons below these maria.

The DSN tracks unmanned deep-space probes, launched by the United States, using earth-based radio transmissions at 2300 MHz in a coherent loop between the spacecraft and receiver. The doppler cycle count, which is the frequency difference between the transmitted and received signal, is continuously accumulated and sampled at regular 60-, 30-, or 10-s intervals. The high-frequency noise on these data is between 0.1 and 1 mm/s except at times of picture readout where the degradation factor is approximately 3. These data permit examination of the observed systematic effects which are in the neighborhood of 10–150 mm/s (65 mm/s = 1 Hz).

2. Data Processing

The doppler data sample presented in this article spans a 10-day period with 80 consecutive, continuously tracked orbits of the *Lunar Orbiter V* spacecraft. The orbital characteristics of the spacecraft were as follows:

(1) The semimajor axis was 2636 km.

(2) The eccentricity was 0.27.

(3) Inclination to the lunar equator was 85°.

(4) The orbital period was $3^h 11^m$.

The closest approach to the lunar surface was 100 km at 2°N lat.

The central 90-min data span, centered on perilune, was taken from each individual orbit for the data processing. The combined coverage of the 80 orbits, south pole to north pole, east limb to west limb, was adequate to cover the lunar nearside hemisphere between ±70° lat and long.

Whereas the processing of the 9000 individual data points was a substantial undertaking, involving hand working of the punched cards, this was only a small fraction of the data available from five orbiters, in several mission phases, with distinct orbit characteristics.

These data were processed by least-squares fitting in which the theoretical model (Ref. 7) included a triaxial moon and gravitation perturbations due to the earth, sun, Venus, Mars, Jupiter, and Saturn. It was necessary to limit the data arcs to 90 min in order to obtain the consistency required for the analysis. The method used is described in Ref. 5 where the definite correlation between the residuals and variations in the lunar gravitational field is demonstrated.

The residuals from the raw doppler data, obtained after the best selenocentric position and velocity of the spacecraft have been estimated, became the data which were further processed. These data contained the local gravity effects since the other variables (e.g., station motion, the primary selenocentric orbit motion, etc.) had been removed by the least-squares fit.

The next step in the reduction was to extract accelerations from the residuals. As shown in Fig. 2, these were fit with patched cubic polynomials (SPS 37-52, Vol. III, pp. 10–14) to smooth the data and to permit determination of an accurate derivative. Since the spacecraft altitude above the lunar surface was not constant, the raw accelerations represented the gravity effects at the height actually flown. What was really desired was a measure of the relative acceleration changes for a constant spacecraft altitude since such measurements would correlate with gravitational changes at or near the lunar surface. For that reason, the accelerations were normalized so that the plotted values represent the acceleration a spacecraft would have experienced if it had been at an altitude of 100 km, under the assumption that the typical mascons were at a depth of 50 km below the surface. That is

$$A_{norm} = A_{comp} \frac{(H + 50)^2}{150^2}$$

where A_{norm} is the normalized acceleration, A_{comp} is the computed acceleration, and H is the altitude in kilometers.

While this arbitrary choice was necessitated by the desire to make simplifying assumptions, some evidence was available as a basis for judgment. The analysis of distinct spacecraft (with different altitudes) flying over the same features had yielded 25–125 km for the depth of perturbing points below the surface. Therefore, 50 km was chosen as an average depth expectation, and spacecraft accelerations normalized to the perilune distance of 100 km were used. The accelerations were therefore based upon these assumptions.

The accelerations were of necessity measured along the spacecraft–earth direction. Since the method of data processing used is a point-by-point scalar system, the unfortunate fact remained that a single data point could

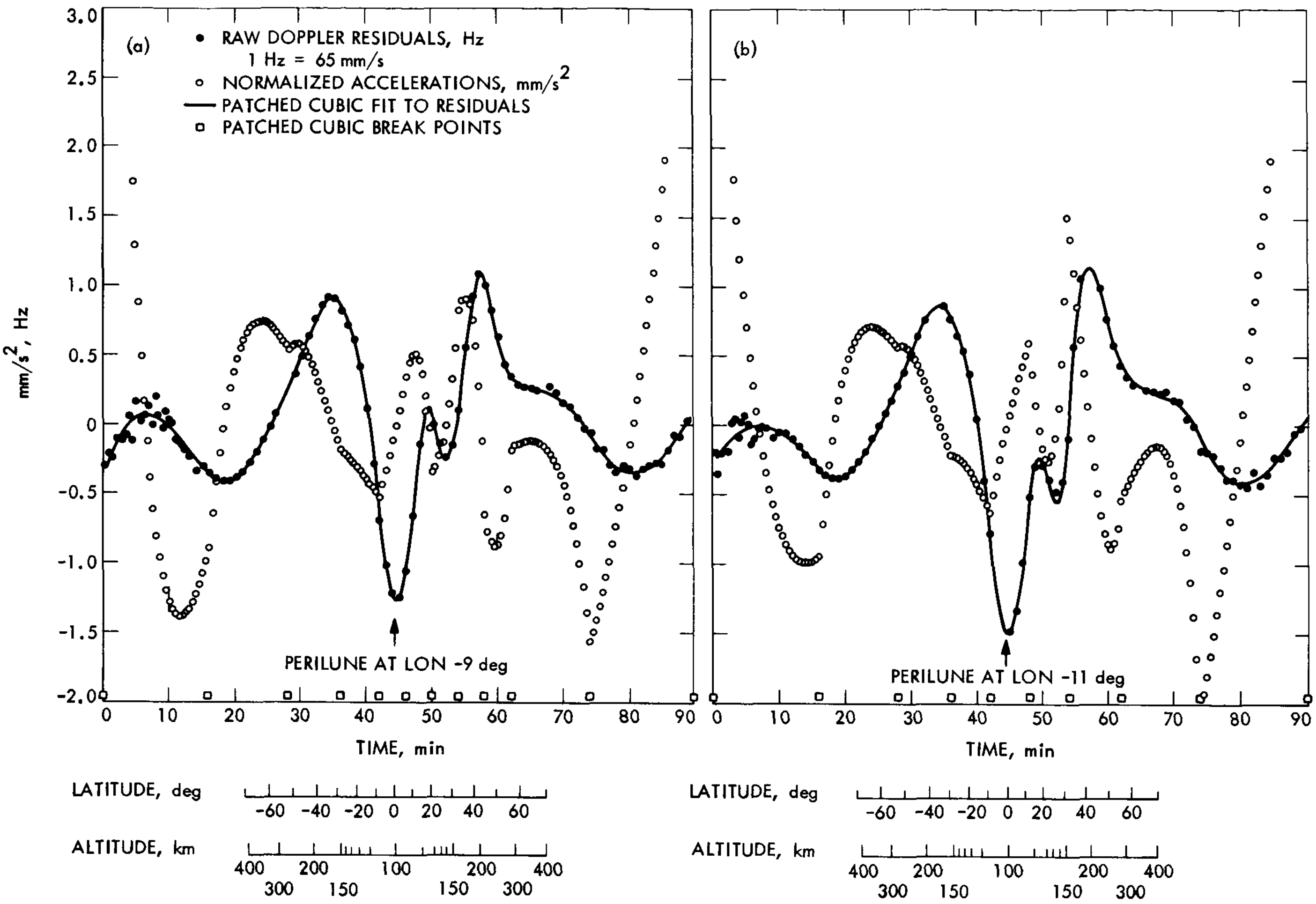

Fig. 2. Data processing results for two consecutive *Lunar Orbiter* V-C orbits: (a) orbit 45, (b) orbit 46

not indicate from what direction the acceleration acted. What was seen was the projection of the true acceleration on the spacecraft–earth vector. Only modeled system-fitting of substantial quantities of continuous data can determine the nature of these geometrical effects.

Since the true direction of the forces was unknown, a simplifying assumption was made in order to tie the observed accelerations to the lunar surface for comparison with a map. Because the acceleration decreased with the distance squared, it was assumed that the force was directly below the trajectory.

The decision to omit a correction for the projection on the spacecraft–earth vector, approximately a cosine function of the angular separation of the spacecraft from the lunar zero latitude and longitude point, resulted in increased uncertainty in the acceleration amplitudes near the limb. Such a correction seemed inadvisable because the true direction was unknown.

These constitute the simplifying assumptions that permitted rapid conversion of the raw residuals into gravimetric data. As already noted, the qualitative aspects of the new observations are rather well preserved at the expense of some of the quantitative information.

From the analysis to date, 74 sets (of the 80 orbits, six had insufficient data) of normalized accelerations (mm/s^2) have been obtained (Fig. 1). While this approach was intended primarily to supply *a priori* information for a more quantitatively precise future analysis, the results proved to be very enlightening and of scientific importance. It should be emphasized that only approximations were made; therefore, those intending to analyze these data should use caution as dictated by the limitations on the method of data reduction.

3. Mascon Location Determination

A contour plot made from the data of Fig. 1 is shown in Fig. 3. The large, distinct positive accelerations, along

Fig. 3. Contour plot of gravimetric and acceleration map

with a smaller number of distinct negative accelerations, are clearly seen. Large positives lie in the centers of all five major ringed maria. The large rate of change in the accelerations over these mascons reveals their relatively small physical extent (50 to 200 km). In fact, analysis of the detailed computer results indicates a non-spherical troughlike mass distribution (approximately 50 by 200 km running generally east–west) in Imbrium and Serenitatis.

The data are consistent, apart from occasional short intervals of poor fit. The individual polar orbits (south–north) are plotted on Fig. 1. The consistency of the results can easily be seen by reading across the map (Fig. 1), i.e., from west to east perpendicular to the individual polar orbits. The variations tend to be smooth and consistent across the adjacent orbit sets. Furthermore, computed comparisons between residual accelerations from an equatorial orbiter (*Lunar Orbiter III*) agree well with the plotted data. These results constitute the data consistency check and the initial estimate of gravity variations sought from the simplified approach.

The more diffuse positive and negative variations shown on the plots near the limbs must be considered doubtful because of the normalizations introduced in the data processing. An orbit determination program, operating under a least-squares fitting, should minimize the sum of residuals squared and tend to compensate for large variations by "splitting the difference." Precisely how this effect appeared on the results is difficult to determine with certainty, but it is suspected that the large accelerations will give rise to diffuse, lower amplitude, opposite and compensating signatures in the processed data.

The contour map shows two nearby mascons of intermediate magnitude between Sinus Aestuum and Sinus Medii. A crucial orbit that might further clarify the situation is missing, and with these data, it is not possible to specify whether these mascons are really distinct. However, this location certainly contains at least one definite mascon. It is consistent to assume that this represents an ancient feature, similar to one of the modest ringed seas, obliterated by the debris from Serenitatis and Imbrium and only now revealed by the new data. There are other lesser mascons which may or may not be significant. There may be correlations with the Russian magnetometer observations from their *Luna* probes if data over the specifically indicated areas is analyzed. Their preliminary statement of results, however, does not indicate any unusual effects.

Table 1. Accelerations in the area of Mare Orientale[a]

Orbit	Accelerations, mm/s^2
88	0.22
89	0.14
90	0.22
91	0.13
92	0.08
93	−0.17[b]
94	−0.17
95	−0.09
96	Occultation

[a] 85–99°W lon at a fixed 22°S lat.

[b] Taking geometry into account, and noting the zero-crossing in the table, permits determination of the Orientale mascon at 95°W lon.

A side investigation of residuals not displayed in Fig. 2 was the examination of data in the area of Mare Orientale (20°S lat, 95°W long), a ringed mare discovered by *Lunar Orbiter* photography. If Mare Orientale has the same characteristics of the other ringed maria, then high accelerations should occur directly above it. Since these largest accelerations would be normal to the probe–earth line at this longitude, one would expect essentially zero effect from the overflight orbit. However, from a family of orbits bracketing this time, one would expect those preceding the overflight to show a modest positive acceleration (at about 22°S lat) and those following to show a negative acceleration. The residuals from these several orbits were plotted and acceleration estimates computed for 22°S lat with eight consecutive orbits (Table 1) resulting in precisely the effect predicted.

Examination of the detailed computer output permitted consistent estimates of the mascon locations. The results of these computations are presented in Table 2 with the estimated probable error.

Table 2. Large positive mascon locations

Ringed maria	Latitude, deg		Longitude, deg	
	Value	PE[a] units	Value	PE[a] units
Imbrium	32 N	1	17 W	1
Serenitatis	25 N	1	19 E	1
Crisium	18 N	1	56 E	2
Nectaris	15 S	1	33 E	1
Humorum	23 S	1	38 W	1
Orientale	20 S	3	95 W	3
Aestuum–Medii	6 N[b]	5	6 W[b]	5

[a] PE = probable error.

[b] Missing data and possible skewed fits make it impossible to resolve whether there are one or two mascons in this location. More sophisticated processing and additional data from other orbiter missions will permit a determination.

4. Conclusion

Even though computations have been made for both masses and depths for the largest mascons, our present quantitative data require further refinements. One may easily compute approximate masses from an assumed depth such as 50 km, e.g., the Mare Imbrium mascon yields numbers on the order of 20×10^{-6} lunar masses. A spherical nickel–iron object about 100 km in diameter would be a rough equivalent. This type of calculation gives a qualitative estimate for the large size of these objects.

The presence of large mascons under every ringed mare, excepting Iridum, and their relative absence elsewhere, suggests a relation between the two phenomena that may be similar to the relation suggested by Urey and Gilbert (Ref. 6). Among the questions that arise are the following:

(1) Does each of these mascons represent an asteroidal-sized body that caused its associated mare by impact?

(2) If the mascons are not simply the original impactors themselves, by what processes were they formed in the lunar interior?

(3) Is the presence of these objects consistent with a molten lunar interior?

Urey (Ref. 8) has proposed that the Mare Imbrium collision object entered at Sinus Iridum as a low elevation impactor while others have held that the two features are independent formations. Sinus Iridum is the smallest ringed mare and, as Urey (Ref. 8) and others (Ref. 9) have pointed out, is a unique feature. It is larger than the other ringed and filled craters, such as Ptolemaeus, and has a similar appearance to the larger ringed maria discussed in this article. If it is a separate impact mare, one would expect its physical properties to resemble the others, and, hence, contain a mascon for the same reasons.

Examination of the data reveals instead a sharply defined, negative acceleration. While this appears to support the Urey hypothesis, it is not necessarily inconsistent with other selenological theories.

References

1. Michael, W. H., Jr., Tolson, R. H., and Gapcynski, J. P., *Science*, Vol. 153, No. 1102, 1966.
2. Lorell, J., in *Measure of the Moon*. Edited by Z. Kopal. Gordon and Breach, Inc., New York, 1967.
3. Tolson, R. H., and Gapcynski, J. P., in *Proceedings of the Eighth International Space Science Symposium: COSPAR Assembly*, held in London, July 1967.
4. Lovell, J., and Sjogren, W. L., *Science*, Vol. 159, No. 625, 1968.
5. Muller, P. M., and Sjogren, W. L., *Consistency of Lunar Orbiter Residuals with Trajectory and Local Gravity Effects*, Technical Report 32-1307. Jet Propulsion Laboratory, Pasadena, Calif., Sept. 1, 1968.
6. Urey, H. C., in *Vistas in Astronomy: Volume II*, p. 1676. Edited by A. Beer. Pergamon Press, London, 1956.
7. Warner, M. R., and Nead, M. W., *SPODP—Single Precision Orbit Determination Program*, Technical Memorandum 33-204. Jet Propulsion Laboratory, Pasadena, Calif., Feb. 15, 1965.
8. Urey, H. C., in *Physics and Astronomy of the Moon*, pp. 484–486. Edited by Z. Kopal. The Academic Press, New York, 1962.
9. Baldwin, R. B., *The Face of the Moon*, p. 200. The University of Chicago Press, Chicago, Ill., 1958.

C. Satellite Determination of the Earth's Gravitational Mass From Doppler and Range Measurements. Part I: Moderate Altitude Orbits, *G. E. Pease*

1. Introduction

The question of the feasibility of determining the earth's gravitational mass from close satellite orbits has been investigated by W. M. Kaula (Ref. 1), R. J. Anderle (Refs. 2 and 3), G. J. Smith (Ref. 2), and others. In general, it has been understood that errors in the assumed value of the earth radius are a limiting factor for close satellites because of the scale relationship of Kepler's third law. Neglecting the effect of oblateness

$$GM = n^2 a^3$$

where

GM = the product of the Newtonian gravitational constant and earth's mass

n = the mean motion

a = the semimajor axis of the satellite orbit or $a = a_e + h$, the radius of the earth plus the satellite altitude

Then

$$\frac{\Delta GM}{GM} = \frac{2\Delta n}{n} + \frac{3(\Delta a_e + \Delta h)}{a}$$

For close orbits, where the mean motion may be accurately measured

$$n \gg \Delta n$$

$$a_e \gg h$$

and

$$\frac{\Delta GM}{GM} \rightarrow \frac{3\Delta a_e}{a_e}$$

whereas, for a distant orbit

$$a_e \ll h$$

and

$$\frac{\Delta GM}{GM} \rightarrow \frac{2\Delta n}{n} + \frac{3\Delta h}{h}$$

Thus, the sensitivity to errors in the earth radius is relatively unimproved by precise range information for close orbits, but becomes a function of this information for distant orbits. In addition, errors in gravitational harmonics are more important in low-altitude orbits. For this reason, most close satellite geodesy work has concentrated on obtaining higher order gravity field harmonics and more or less ignored the possibility of improving the value for *GM* obtained from lunar and planetary spacecraft. With the advent of more powerful boosters and high-orbit synchronous communication satellites, however, the possibility of obtaining a very precise *GM* presents itself.

In this article, some results from simulated doppler and range tracking of a Navy low-inclination doppler only (LIDO)-type satellite orbit are given. This orbit is of interest because, with a semimajor axis of about 9158 km, it is somewhat higher than a typical close-orbit satellite ($a < 8000$ km), yet n may be precisely measured by tracking over more than one pass. Eccentricity and inclination of the model orbit are also high—0.2 and 96 deg, respectively. This high inclination gives the satellite an extensive earth track and, hence, favorable tracking geometry.

2. Tracking Model

For the purpose of this study, simulated 60-s range and range-rate data were analyzed with 1σ weights of $\sigma\rho = 25$ m and $\sigma\dot{\rho} = 5$ mm/s, respectively, assuming 60 s between data samples. These accuracies are more in accord with the JPL S-band and Goddard systems than with the LIDO TRANET system (doppler only) accuracy, but they are felt to be representative of presently attainable technology even though not necessarily applicable to LIDO itself.

Three tracking stations [Pioneer, Johannesburg, and Robledo Deep Space Stations (DSSs)] were simulated. Again, these station locations (which correspond to existing DSSs) are not associated with a specific satellite mission such as LIDO, but were chosen for their favorable relative geometry.

3. Statistical Analysis

The JPL single precision orbit determination program (SPODP; Ref. 4) was used to numerically integrate a trajectory by the Cowell method and to compute partial derivatives of the ρ and $\dot{\rho}$ data types with respect to an initial satellite position, velocity, and *GM*; and to the geocentric radius (r), latitude (ϕ), and longitude (λ) of each of the three tracking stations. These partial derivatives were then multiplied by themselves and the inverse data weights and combined with an *a priori* diagonal covariance matrix ($\tilde{\Gamma}$) to form the covariance matrix of estimated parameters (Γ). If ϕ_i is the vector of partial derivatives and w_i the data weight at the ith observation

$$\Gamma = \left(\sum_{i=1}^{N} \phi_i \, w_i^{-1} \, \phi_i^T + \tilde{\Gamma}^{-1} \right)^{-1}$$

This has been computed at hourly intervals using the JPL double precision matrix manipulation program (DPMMP).[2] The *a priori* standard deviations used were as follows:

(1) 1000 km on position components.

(2) 1 km/s on velocity components.

(3) 10 km^3/s^2 on *GM*.

(4) 50 m for the r, λ, and ϕ of the three tracking stations.

Gravity harmonics were not estimated as these are probably better estimated from low-altitude satellites. Errors in the current values should not be an appreciable error source in determining *GM* from a LIDO-type orbit.

Figure 4 shows the solution for *GM* as a function of tracking data from the Pioneer and Johannesburg DSSs. After 7 h (nearly three orbits), the doppler and ranging solution levels off at a standard deviation of 0.33 which is comparable to that obtainable on a lunar or planetary mission. For example, the 5 days of doppler-only premidcourse maneuver orbit determination for *Mariner V* yield a *GM* value of 398601.49 ±0.39 km^3/s^2. The lunar flights yield similar standard deviations. The doppler-only satellite solution of $\sigma GM = 0.93$ after 7 h is not very impressive.

---

[2] Hilt, D. E., *Double Precision Matrix Manipulation Program*, Apr. 1, 1968 (JPL internal document).

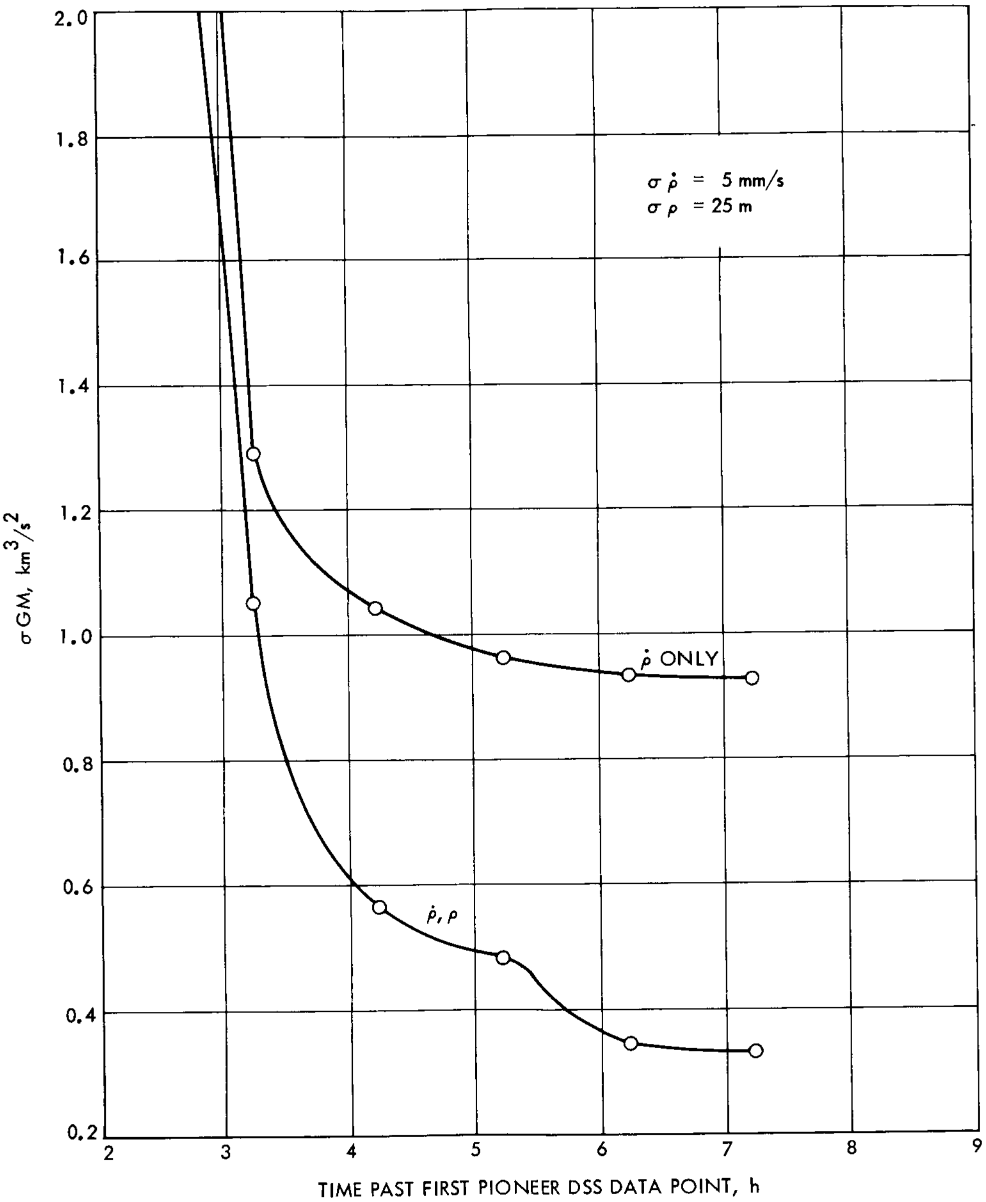

Fig. 4. σGM from Pioneer and Johannesburg DSSs tracking data

Figure 5 shows results for all three tracking stations, with Robledo DSS tracking some 2.5 h before Pioneer DSS. After 9.7 h (4 orbits), the solution for *GM* from doppler and ranging reaches a 1σ value of 0.27. It appears that the addition of the third station also improves the doppler-only solution, which reaches $\sigma GM = 0.65$ at 9.8 h and seems to be still dropping at this point.

The complete parameter solutions at the last data point time of Figs. 4 and 5 are summarized in Table 3. It is seen that while the solution for tracking station longitudes is poor, it is somewhat improved by the addition of the third tracking station. Relative longitudes, however, are comparatively well determined, although this fact is not shown in Table 3 which lists only the absolute standard deviations. The correlations between the various tracking station longitudes range from 0.988 to 0.998 in the four solutions shown in Table 3.

4. Conclusion

It appears that the solution for *GM* from a moderate-altitude earth satellite ($a \approx 9000$ km) of high inclination is comparable in accuracy to that obtained from a lunar

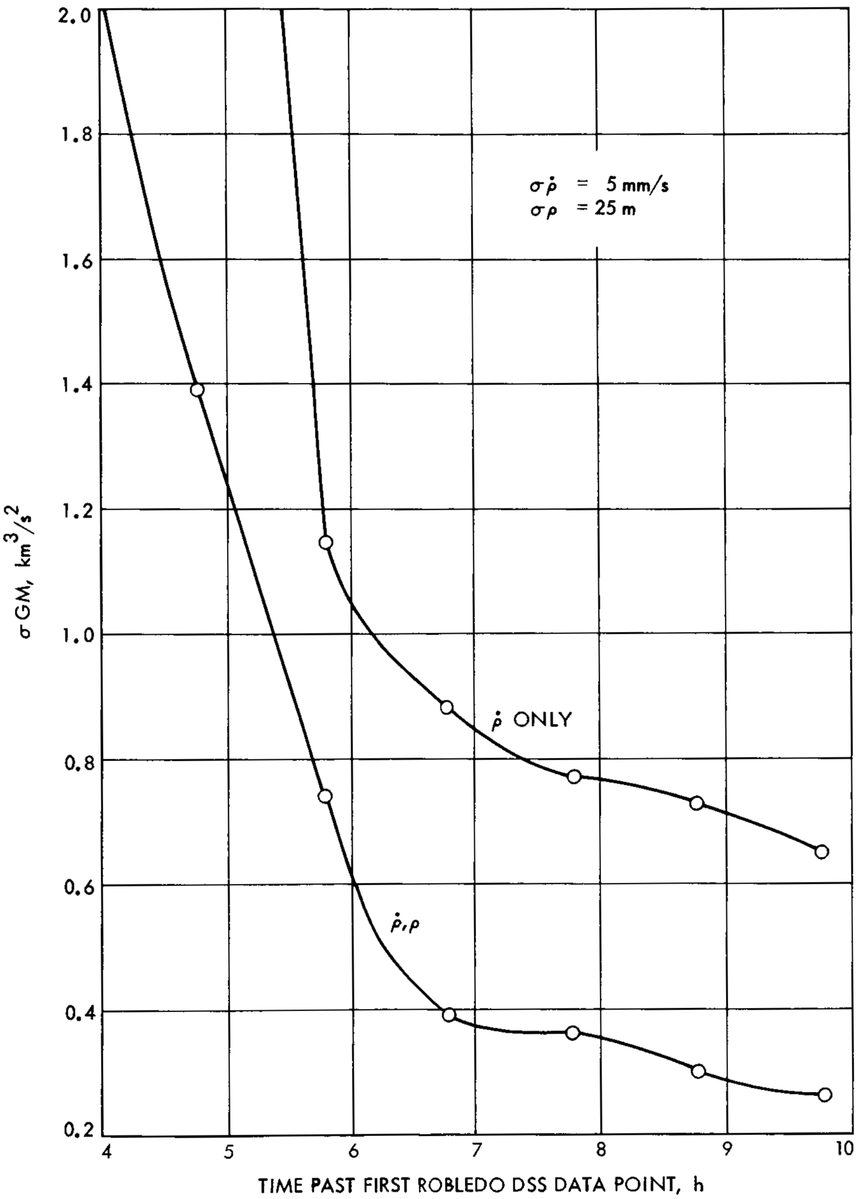

Fig. 5. σGM from Robledo, Pioneer, and Johannesburg DSSs tracking data

Table 3. Satellite orbital parameter solutions at Pioneer DSS rise plus 7^h14^m

Parameter	A priori σ	Standard deviations			
		Pioneer, Johannesburg DSSs		Robledo, Pioneer Johannesburg DSSs	
		$\dot{\rho}, \rho$	$\dot{\rho}$ only	$\dot{\rho}, \rho$	$\dot{\rho}$ only
Geocentric equatorial					
x, m	10^6	14	14	11	12
y, m	10^6	5	7	4	5
z, m	10^6	5	12	4	7
$\dot{x}$, mm/s	10^6	31	31	25	25
$\dot{y}$, mm/s	10^6	23	23	19	19
$\dot{z}$, mm/s	10^6	6	8	5	7
GM, km^3/s^2	10	0.33	0.93	0.26	0.65
Pioneer DSS					
r, m	50	4	7	3	4
ϕ, m	50	7	9	4	4
λ, m	50	35	35	29	29
Johannesburg DSS					
r, m	50	4	5	3	4
ϕ, m	50	6	9	5	7
λ, m	50	35	35	29	29
Robledo DSS					
r, m	50			4	5
ϕ, m	50			4	5
λ, m	50			29	29

or planetary flight if high-precision ranging data is taken. Furthermore, this solution is obtainable after only three or four orbits, thus minimizing the effects of long-term systematic errors such as atmospheric drag, solar-radiation pressure, attitude-control thrust, etc. The situation is not as favorable with doppler data only. The addition of a third tracking station seems to offer the hope of obtaining a more reasonable solution in five or six orbits, although the scale relationship $GM = n^2(a_e + h)^3$ limits this type of solution in which neither a_e nor h are directly determined. A future article will explore the possibility of estimating GM from tracking a high-altitude satellite.

References

1. Kaula, W. M., "Comparison and Combination of Satellite with Other Results for Geodetic Parameters," in *The Use of Artificial Satellites for Geodesy: Vol. 2,* proceedings of the Second International Symposium on the Use of Artificial Satellites for Geodesy, held in Athens, 1965. Edited by G. Veis. North-Holland Publishing Co., Amsterdam, 1965.
2. Anderle, R. J., and Smith, G. J., Technical Report 2106, U. S. Naval Weapons Laboratory, Dahlgren, Va., 1967.
3. Anderle, R. J., "Accuracy of the Determination of Gravity Parameters and Geocentric Station Coordinates on the Basis of Observations of Artificial Satellites," in *The Use of Artificial Satellites for Geodesy: Vol. 1,* proceedings of the First International Symposium on the Use of Artificial Satellites for Geodesy held in Washington, D. C., 1962. Edited by G. Veis. North-Holland Publishing Co., Amsterdam, 1963.
4. Warner, M. R., Nead, M. W., and Hudson, R. H., *The Orbit Determination Program of the Jet Propulsion Laboratory,* Technical Memorandum 33-168. Jet Propulsion Laboratory, Pasadena, Calif., Mar. 18, 1964.

D. Ionospheric Charged Particle Influences on Surveyor Tracking Data, *F. B. Winn*

1. Diurnal Error Sources

The ionospheric charged particle effect on two-way doppler, the *Surveyor* tracking data type, is a function of the time rate of change of the total number of electrons encountered by the radio tracking wave as the signal passes through the ionosphere. The electron density for any ionospheric unit volume along the signal ray path is dependent on the solar activity, the sun–earth–probe angle, the frequency of the radio propagation, and the relative elevation and azimuth between the deep space station (DSS) and the spacecraft. The inter-relation of the geometrical parameters can be more readily seen in Fig. 6.

The "observed minus computed" (O − C) residuals of the *Surveyor* tracking data fits[3] were noted to have a diurnal nature (Fig. 7). In SPS 37-51, Vol. II, pp. 42–50, the author demonstrated that solving for a lunar day mean tropospheric refractivity index for each DSS involved in the *Surveyor* tracking effectively removed the diurnal signature from *Surveyor* residual sets (Fig. 8). Then, as now, it was known that the daily O − C residual excursions were not solely due to tropospheric refraction, but that the error signature was primarily a summation of the ionospheric charged particle influence, topocentric projected lunar ephemeris deficiencies, and atmospheric refraction. Noting the statistically high correlation between these error sources, it became evident that the ionospheric influences on the radio tracking data could not be statistically separated from the other two mentioned error sources and successfully solved for in a recursive least-squares adjustment. Thus, the need to determine and remove the ionospheric charged particle

---

[3] The single precision orbit determination program (SPODP; Ref. 1) was used to process the coherent two-way doppler data from the *Surveyors.*

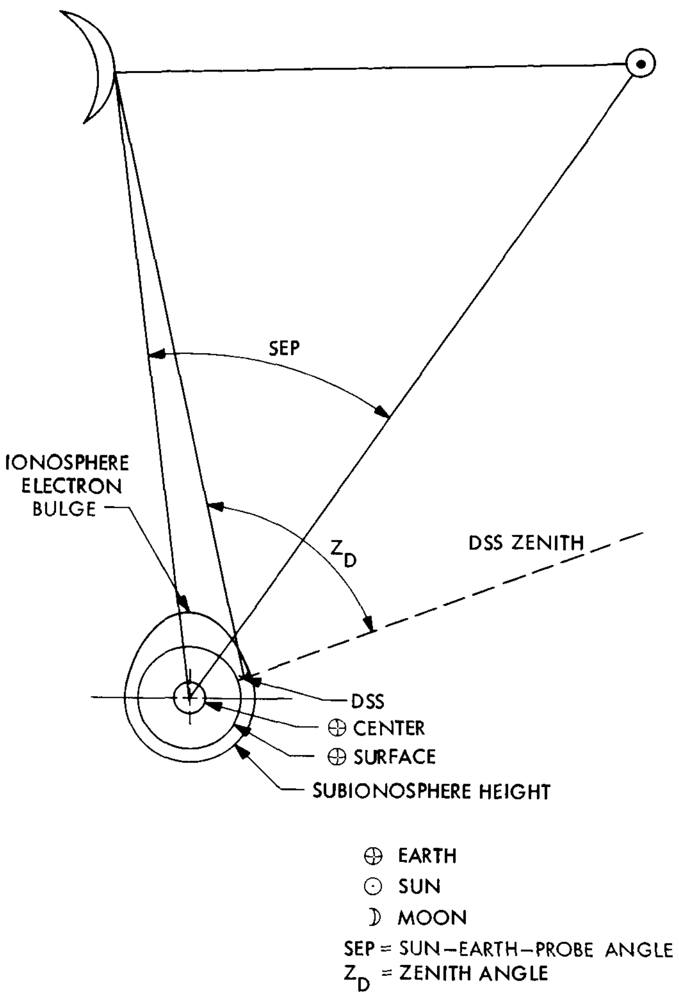

Fig. 6. Spacecraft geometry as observed from the deep space station

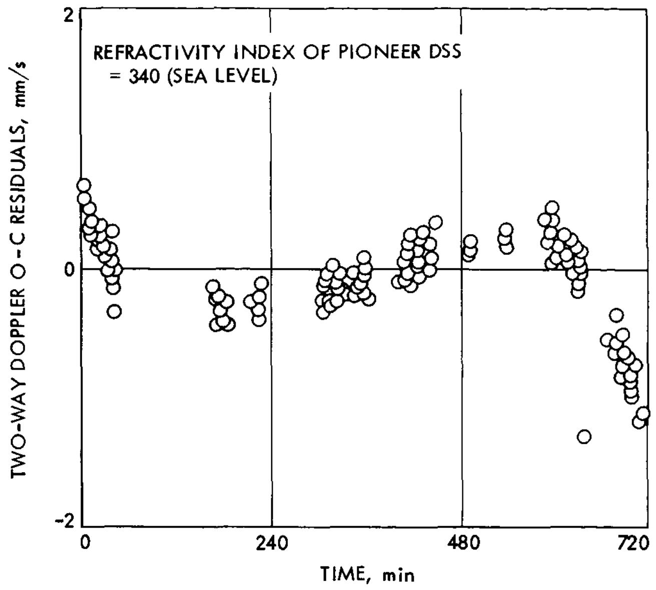

Fig. 7. *Surveyor VII* diurnal signature

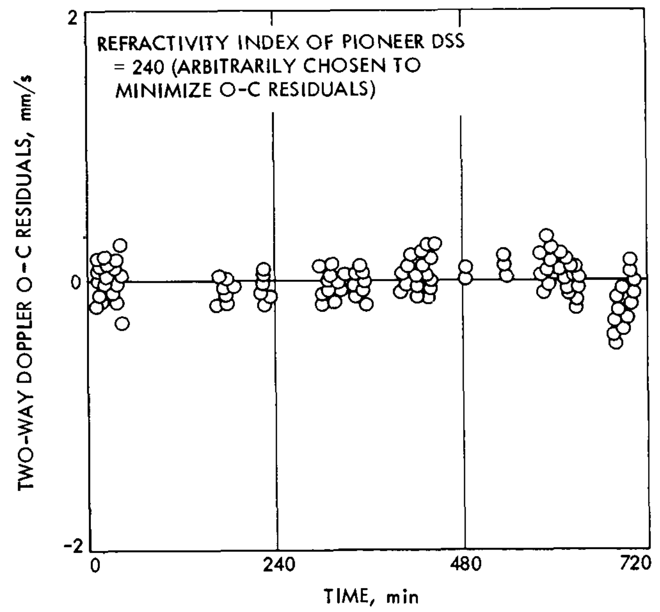

Fig. 8. *Surveyor VII* diurnal signature removed via combinational parameter fit

influence from the tracking data before the data is employed in a differential least-squares adjustment became obvious.

A comparison of DSS and probe-location parameters resulting from *Surveyor* data fits that did and did not employ the lunar day mean tropospheric refractivity parameter demonstrates the corruption of the fit due to the diurnal error sources (Table 4).

2. Elimination of Ionospheric Charged Particle Effects From Tracking Data

The procedure to be outlined is a simple empirical approach that makes use of the Stanford Radio Science Laboratory's Faraday rotation measurements of the polarized transmissions from the Applications Technology Satellite 1 (ATS 1). Stanford continuously monitored ATS 1 and deduced the ionospheric charged particle count history during each of the *Surveyor* first lunar days. Figure 9 shows two 24-h histories of ionospheric electron counts. One depicts the ionospheric electron count history along a Stanford ATS 1 ray path, and the other depicts the electron count history along a Flagstaff ATS 1 ray path. Both profiles have been normalized by Stanford to a zenith observation profile. It is apparent from Fig. 9 that the electron count history as determined for one

Table 4. DSS and *Surveyor VII* coordinates

Conditions	Pioneer DSS		Tidbinbilla DSS		Robledo DSS		*Surveyor VII*	
	λ_s[a]	r_s[b]	λ_s	r_s	λ_s	r_s	λ[c]	ϕ[d]
With diurnal error signature	243°.15112	6372.9973 km	148°.988193	6371.6824 km	355°.75162	6370.0079 km	348°.47319	−40°.8578
Diurnal error signature fitted out (fictitious refractivity parameter)	243°.15108	6372.0034 km	148°.98188	6371.6894 km	355°.75158	6370.0034 km	348°.48208	−40°.8628
Net change in geocentric coordinates of the DSS and the selenocentric coordinates of *Surveyor VII*	4 m	6 m	5 m	7 m	4 m	4 m	266 m	150 m

[a] λ_s = geocentric longitude

[b] r_s = spin-axis distance

[c] λ = selenocentric longitude

[d] ϕ = selenocentric latitude

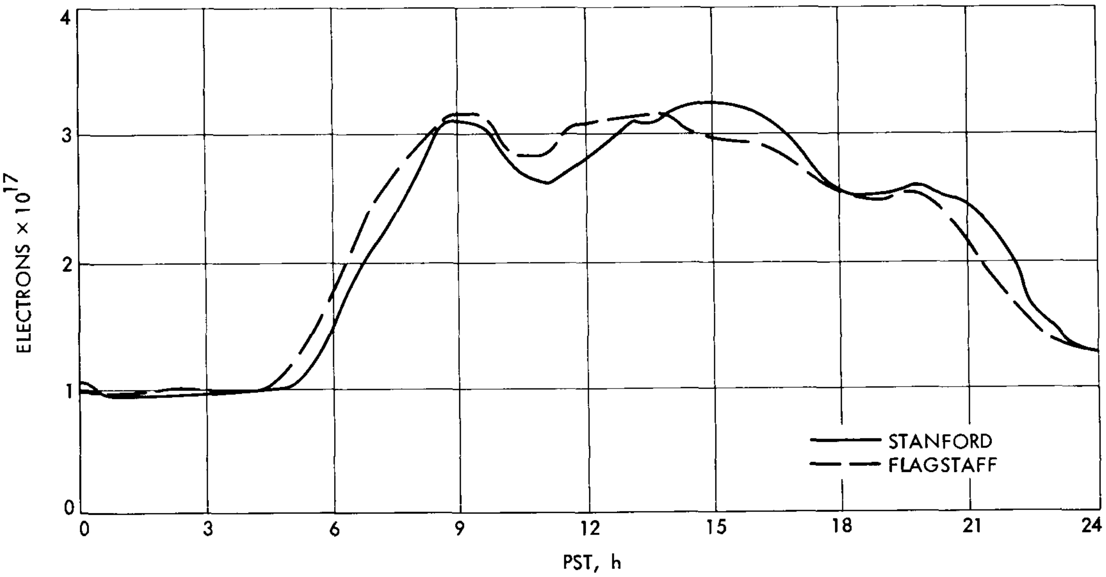

Fig. 9. Stanford and Flagstaff Faraday rotation measurements (July 10, 1967)

longitude can be used to deduce some epoch electron count for a different longitude. All that is required to determine the zenith electron count at the Flagstaff longitude from the Stanford electron count profile is a simple time offset

$$T_{Flagstaff} = T_{Stanford} - \Delta T = T_{Stanford} - (\lambda_{Stanford} - \lambda_{Flagstaff}) \times 15.0$$

where

$T_{Flagstaff}$ = Flagstaff look-up time on Stanford ATS 1 time scale

$T_{Stanford}$ = time of Stanford ATS 1 observation

$\lambda_{Flagstaff}$ = Flagstaff longitude

$\lambda_{Stanford}$ = Stanford longitude

Figure 9 has the Stanford and Flagstaff electron count profiles displaced from each other by ΔT (time scale set apart by the longitude difference of the two stations).

Similarly, to use the Stanford data to determine the electron count at some *Surveyor* subionospheric terrestrial longitude requires a time offset

$$T_{Surveyor} = T_{Stanford} - \Delta T = T_{Stanford} - (\lambda_{Stanford} - \lambda_{Surveyor}) \times 15.0$$

where

$T_{Surveyor}$ = *Surveyor* look-up time on Stanford time scale

$T_{Stanford}$ = time of Stanford observation

$\lambda_{Surveyor}$ = *Surveyor* subionospheric point longitude

$\lambda_{Stanford}$ = Stanford longitude

Once the appropriate time shift has been executed and the zenith electron count determined, it is necessary to scale the electron count number to the correct elevation. The scaling factor is of the following form

$$\frac{\Delta\rho_{Su\ V}(\gamma_{Su\ V})}{\Delta\rho_{ATS\ I}(\gamma_{ATS\ I})} = \text{scaling factor}$$

where

$\Delta\rho$ = range correction

γ = elevation

$\Delta\rho_{Su\ V}(\gamma_{Su\ V}) = \Delta\rho_{Su\ V} = f(\gamma)$

$\Delta\rho_{ATS\ I}(\gamma_{ATS\ I}) = \Delta\rho_{ATS\ I} = f(\gamma)$

The elevation function is derived from the ray-traced solution for a Chapman ionosphere (SPS 37-41, Vol. III, pp. 38–41). Thus, the differences between effective path slant ranges through the ionosphere are taken into consideration.

The range correction ($\Delta\rho$) and the velocity correction ($\Delta\dot{\rho}$) applicable to each *Surveyor* data point can be derived from the above procedure. Figures 10, 11, and 12 represent the $\Delta\rho$ and $\Delta\dot{\rho}$ corrections to the *Surveyor V* tracking data for September 12, 15, and 18, 1967, respectively, as determined from this procedure.

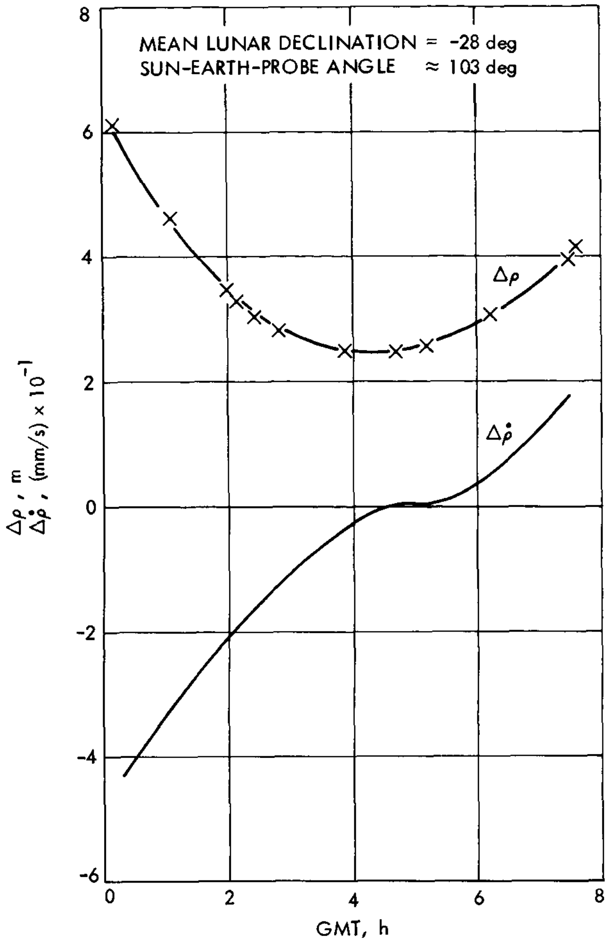

Fig. 10. $\Delta\rho$ and $\Delta\dot{\rho}$ corrections for *Surveyor V* track path referenced from Pioneer DSS for Sept. 12, 1967

The September 12, 1967 $\Delta\dot{\rho}$ corrections exhibited by Fig. 10 represent approximately 25% of the observed *Surveyor V* O − C doppler residuals for that date. The ionospheric charged particle effect is some four times larger than the high-frequency noise characteristic of *Surveyor* data (Figs. 7, 10, 11, and 12). Thus, it is apparent that the SPODP least-squares minimization techniques have corrupted the parameter solutions in the course of minimizing the sum of the squares of the weighted residuals. The extent of this corruption in terms of specific parameters is not known at this time.

Efforts are presently underway to remove the ionospheric charged particle influence from the tracking data samples by the above outlined procedures before the SPODP least-squares fit. Once this has been accomplished, there is still the problem of statistically separating the remaining diurnal error sources plaguing the *Surveyor* tracking data samples. It may prove more convenient to adopt a similar pre-data-correction philosophy for the tropospheric refraction influences on *Surveyor* data utilizing the tropospheric refraction determinations of the Pioneer DSS data fits. If such is the case, the only

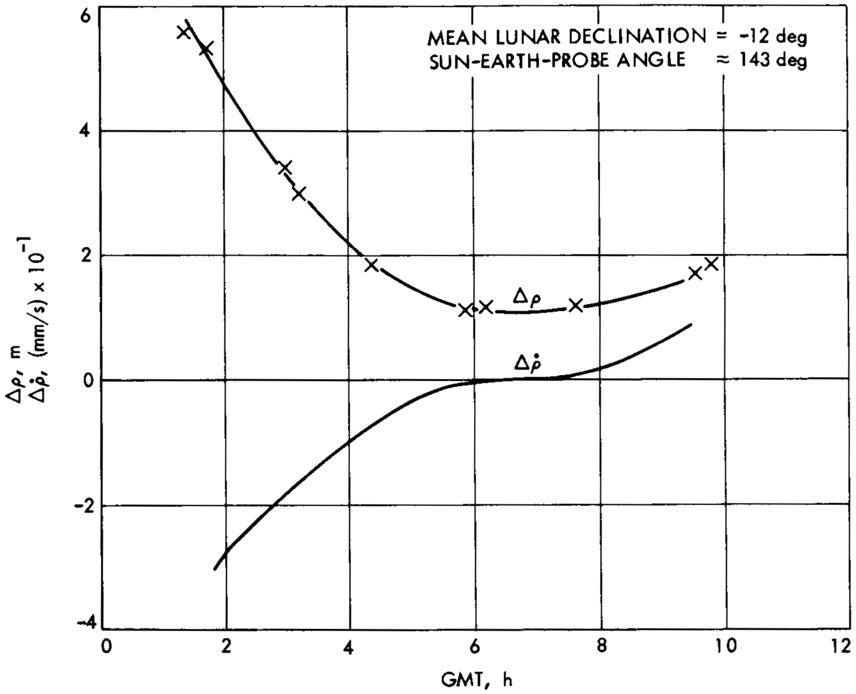

Fig. 11. $\Delta\rho$ and $\Delta\dot{\rho}$ corrections for *Surveyor V* track path referenced from Pioneer DSS for Sept. 15, 1967

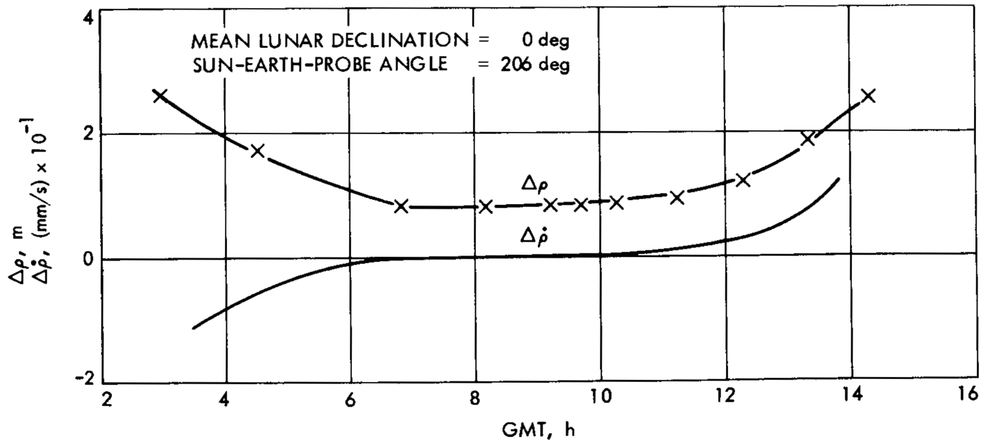

Fig. 12. $\Delta\rho$ and $\Delta\dot{\rho}$ corrections for *Surveyor V* track path referenced from Pioneer DSS for Sept. 18, 1967

known remaining diurnal error source for the least-squares model to evaluate would be the topocentric projection of the lunar ephemeris deficiencies.

Reference

1. Warner, M. R., and Nead, M. W., *SPODP—Single Precision Orbit Determination Program,* Technical Memorandum 33-204. Jet Propulsion Laboratory, Pasadena, Calif., Feb. 15, 1965.

E. Continuous Estimation of the State of a Distant Spacecraft Being Perturbed by Random Accelerations,[4] *J. F. Jordan*

1. Introduction

Utilization of continuous propulsion in unmanned interplanetary flight requires entirely new navigation analysis concepts. The presence of the continuously-operating propulsion device in the spacecraft system gives rise to large random nongravitational forces that influence the trajectory and, hence, the Deep Space Network (DSN) tracking data. These forces result primarily from errors in the thrustor performance, i.e., errors in the magnitude of the thrust and in the thrust direction orientation.

This article is concerned with a comprehensive study of the accuracy of state estimation techniques for powered flight trajectories that utilize tracking data from the NASA/JPL DSN facilities. The purpose of the study is to establish the inherent accuracy of the DSN for such tasks.

The approach used in the study employs the continuous data filtering techniques first developed by R. E. Kalman (Ref. 1). The random forces mentioned above are modeled as noise perturbing the behavior of the differential equations of motion of the space probe. The statistics of the noise are assumed known. Earth-based counted doppler tracking data are assumed to be continuously supplied to the observer from a single DSN facility, and the information content of the data is determined from the integration of a matrix Riccati differential equation for the covariance matrix of the errors in the minimum variance estimates of the state parameters of the probe. Numerical integration of the matrix Riccati equation is performed by the Continuous Estimation program. A description of the program and the application of the continuous data filtering technique to a ballistic trajectory orbit determination problem are given in SPS 37-48, Vol. II, p. 23; SPS 37-49, Vol. II, p. 43; and SPS 37-52, Vol. II, pp. 37–44.

The inherent observing power of a single tracking station is evaluated in terms of the information content of a few successive passes of data. The relative motion of the tracking station and space probe during the pass gives rise to the phenomena known as station–probe velocity parallax and position parallax, which result in the ability of the estimator to determine the following geocentric parameters associated with the space probe (SPS 37-39. Vol. II, p. 18 and SPS 37-47, Vol. II, p. 15):

(1) Geocentric range rate of change.

(2) Right ascension.

(3) Geocentric declination.

(4) Right ascension rate of change.

(5) Declination rate of change.

(6) Range (if the rate of change of declination or right ascension is large).

The accuracies of the above parameters are noted over a few successive passes of data, and their dependency on the statistics of the random forces acting on the spacecraft is demonstrated. The relative influence of other error sources (e.g., station location errors, solar pressure variations, onboard gas jet leakages, etc.) is discussed and their effects on the powered flight inherent accuracies are shown to be small.

The dependency of the accuracy results on the position and velocity of the space probe is shown.

2. Coordinate System and Problem Formulation

Consider a tracking station located on the earth's equator observing a distant space probe. The probe state and station location can be specified in the inertial coordinate system defined and illustrated in SPS 37-52, Vol. II, pp. 37–38.

The equations of motion of the space probe are given by

$$\left.\begin{aligned} \dot{u} &= f_x(x, y, z) + a_x + \eta_x \\ \dot{v} &= f_y(x, y, z) + a_y + \eta_y \\ \dot{w} &= f_z(x, y, z) + a_z + \eta_z \end{aligned}\right\} \qquad (1)$$

---

[4] The technical content of this article is contained in a paper entitled "Orbit Determination for Powered Flight Space Vehicles on Deep Space Missions" presented by the author at the AAS–AIAA Astrodynamics Specialists Conference, Jackson Lake Lodge, Wyo., Sept. 3–5, 1968.

where

$$\bar{f} = \begin{bmatrix} f_x \\ f_y \\ f_z \end{bmatrix}$$ represents the acceleration of the probe due to gravitational sources

$$\bar{a} = \begin{bmatrix} a_x \\ a_y \\ a_z \end{bmatrix}$$ represents the acceleration of the probe due to a continuously thrusting engine

$$\bar{\eta} = \begin{bmatrix} \eta_x \\ \eta_y \\ \eta_z \end{bmatrix}$$ is a spherically distributed vector of random accelerations (process noise)

The components of the noise vector $\bar{\eta}$ are assumed to be independent of one another and exponentially autocorrelated in time; hence, the statistical properties of $\bar{\eta}$ are given by

$$\begin{aligned} E\,[\bar{\eta}] &= 0 \\ E\,[\eta(t_1)\eta(t_2)^T] &= R(t_1, t_2) \\ &= \begin{bmatrix} r(t_1, t_2) & 0 & 0 \\ 0 & r(t_1, t_2) & 0 \\ 0 & 0 & r(t_1, t_2) \end{bmatrix} \end{aligned} \qquad (2)$$

where

$$r(t_1, t_2) = \sigma_\eta^2 \exp\left(-\frac{1}{\tau_\eta}\,|\,t_2 - t_1\,|\right)$$

σ_η is the standard deviation of the process noise, and τ_η is the correlation time.

The station position and velocity during the pass can be expressed in terms of geophysical constants by

$$\left.\begin{aligned} x_s &= r_s \cos\delta_0 \sin\omega t & u_s &= \omega r_s \cos\delta_0 \cos\omega t \\ y_s &= -r_s \cos\omega t & v_s &= \omega r_s \sin\omega t \\ z_s &= -r_s \sin\delta_0 \sin\omega t & w_s &= -\omega r_s \sin\delta_0 \cos\omega t \end{aligned}\right\} \qquad (3)$$

where

t = the time measured from the beginning of pass

ω = angular velocity of earth

δ_0 = *a priori* geocentric declination of probe

r_s = equatorial radius of earth

3. Observable Assumptions

The observational data obtained by the station are counted doppler, or integrated range-rate, contaminated by stationary exponentially correlated noise. Hence, the observable $\phi(t)$ can be expressed as

$$\phi(t) = \int_0^t \dot{\rho}(\tau)d\tau + \epsilon(t) \qquad (4)$$

where the station–probe range is related to the probe state by

$$\rho^2 = (x-x_s)^2 + (y-y_s)^2 + (z-z_s)^2 \qquad (5)$$

The additive noise $\epsilon(t)$ is also assumed to be exponentially correlated in time; hence, $\epsilon(t)$ has the statistical properties

$$\left.\begin{aligned} E\,[\epsilon(t)] &= 0 \\ E\,[\epsilon(t_1)\,\epsilon(t_2)] &= \sigma_\epsilon^2 \exp\left(-\frac{1}{\tau_\epsilon}\,|\,t_2 - t_1\,|\right) \end{aligned}\right\} \qquad (6)$$

where σ_ϵ^2 is the variance of the data noise and τ_ϵ is the correlation time.

It should be noted that $\epsilon(t)$, as well as the component of $\bar{\eta}$, satisfies the Langevin differential equation

$$\dot{\epsilon}(t) = -\frac{1}{\tau_\epsilon}\,\epsilon(t) + \xi(t) \qquad (7)$$

where $\xi(t)$ is gaussian white noise possessing the properties

$$\left.\begin{aligned} E\,[\xi(t)] &= 0 \\ E\,[\xi(t_1)\xi(t_2)] &= \frac{2\sigma_\epsilon^2}{\tau_\epsilon}\,\delta(t_2 - t_1) \end{aligned}\right\} \qquad (8)$$

The information content of the data is unchanged if the derivative of the counted doppler is regarded as the observable. This derivative can be written as

$$\phi(t) = \dot{\rho}(t) - \frac{1}{\tau}\,\epsilon(t) + \xi(t) \qquad (9)$$

Thus, the observable can be thought of as the station–probe range-rate contaminated by exponentially correlated noise, which can be estimated, and white noise.

The analytical expression for the station–probe range can be differentiated to obtain the range rate $\dot{\rho}$, i.e.

$$\dot{\rho} = \frac{x-x_s}{\rho}\frac{d}{dt}(x-x_s) + \frac{y-y_s}{\rho}\frac{d}{dt}(y-y_s) + \frac{z-z_s}{\rho}\frac{d}{dt}(z-z_s) \tag{10}$$

If we let r be the earth–probe distance, and note that ρ is extremely large compared with x, y, z, x_s, y_s and z_s, we can approximate ρ in the denominator of the above expression with r. Thus, Eq. (10) can be written as

$$\dot{\rho} = u-u_s + \frac{y-y_s}{r}(v-v_s) + \frac{z-z_s}{r}(w-w_s) \tag{11}$$

and the elements of the vector of the approximate partials of $\dot{\rho}$ with respect to the estimated parameters, $\partial\bar{\dot{\rho}}/\partial x$, are listed as

$$\left.\begin{array}{ll} \dfrac{\partial\dot{\rho}}{\partial u} = 1 & \dfrac{\partial\dot{\rho}}{\partial x} = -\dfrac{(y-y_s)(v-v_s)}{r^2} - \dfrac{(z-z_s)(w-w_s)}{r^2} \\ \dfrac{\partial\dot{\rho}}{\partial v} = \dfrac{y-y_s}{r} & \dfrac{\partial\dot{\rho}}{\partial y} = \dfrac{v-v_s}{r} \\ \dfrac{\partial\dot{\rho}}{\partial w} = \dfrac{z-z_s}{r} & \dfrac{\partial\dot{\rho}}{\partial z} = \dfrac{w-w_s}{r} \end{array}\right\} \tag{12}$$

It is seen from the partials that the primary parameter that can be estimated is the velocity component along the *a priori* earth–probe line, u. There is also secondary estimation capability for the lateral velocities v and w and the lateral positions y and z. The range x cannot be effectively estimated unless v or w is large. It should be noted that the partials, with respect to the lateral positions y and z, depend upon the lateral velocities of the probe and station. These are the so-called "velocity parallax" terms. The partials, with respect to the lateral velocities v and w, depend on the lateral position components of the probe and station. These are referred to as "position parallax" terms.

4. The Continuous Filter Equations

If the six state components of the probe, the three random acceleration components, and the data noise are formulated as a 10 × 1 vector

$$\bar{x}^T = (u, v, w, x, y, z, \eta_x, \eta_y, \eta_z, \epsilon) \tag{13}$$

the accuracy to which the elements of the vector can be estimated can be expressed in terms of the covariance matrix of the errors in the estimates

$$\Lambda = E\,[\bar{x}-\hat{\bar{x}})(\bar{x}-\hat{\bar{x}})^T] \tag{14}$$

where $\hat{\bar{x}}$ denotes the minimum variance estimate of the vector $\bar{x}$.

The square roots of the first six diagonal terms of the covariance matrix are taken as the rms accuracies of the probe state components. These terms can be stated as

$$\begin{array}{ll} \sigma_u = \left[E\,[u-\hat{u}]^2\right]^{1/2} & \sigma_x = \left[E\,[x-\hat{x}]^2\right]^{1/2} \\ \sigma_v = \left[E\,[v-\hat{v}]^2\right]^{1/2} & \sigma_y = \left[E\,[y-\hat{y}]^2\right]^{1/2} \\ \sigma_w = \left[E\,[w-\hat{w}]^2\right]^{1/2} & \sigma_z = \left[E\,[z-\hat{z}]^2\right]^{1/2} \end{array}$$

The covariance matrix during a pass of data is obtained from the solution of the Riccati differential equation

$$\dot{\Lambda} = F\Lambda + \Lambda F^T - \Lambda G \Lambda + H \tag{16}$$

where, following Ref. 1, the elements of F, G, and H are given by

$$F(10 \times 10) = \begin{array}{cccc|c} 3 & 3 & 3 & 1 & \\ \hline & \left(\frac{\partial \bar{f}}{\partial x}\right) & & & 3 \\ I(3 \times 3) & & & & 3 \\ & & \left(-\frac{1}{\tau_\eta}\right) I(3 \times 3) & & 3 \\ \multicolumn{2}{c}{\left(\frac{\partial \bar{\rho}}{\partial x}\right)^T} & & & 1 \end{array} \tag{17}$$

$$G(10 \times 10) = \frac{\tau_\epsilon}{2\sigma_\epsilon^2} \begin{array}{ccc|c} 6 & 3 & 1 & \\ \hline \left(\frac{\partial \bar{\rho}}{\partial x}\right)\left(\frac{\partial \bar{\rho}}{\partial x}\right)^T & & -\frac{1}{\tau_\epsilon}\left(\frac{\partial \bar{\rho}}{\partial x}\right) & 6 \\ & & & 3 \\ -\frac{1}{\tau_\epsilon}\left(\frac{\partial \bar{\rho}}{\partial x}\right)^T & & \left(\frac{1}{\tau_\epsilon}\right)^2 & 1 \end{array} \tag{18}$$

$$H(10 \times 10) = \begin{array}{ccc|c} 6 & 3 & 1 & \\ \hline & & & 6 \\ & \left(2\,\frac{\sigma_\eta^2}{\tau_\eta}\right) I(3 \times 3) & & 3 \\ & & & 1 \end{array} \tag{19}$$

It should be noted that when data are not being taken, the covariance matrix of the state and process noise, $\Lambda'\,(9 \times 9)$, obeys the linear differential equation.

$$\dot{\Lambda}' = E\Lambda' + \Lambda' E^T + K \tag{20}$$

where

$$E(9 \times 9) = \begin{array}{ccc|c} 3 & 3 & 3 & \\ \hline & \frac{\partial \bar{f}}{\partial x} & & 3 \\ I(3 \times 3) & & & 3 \\ & & -\frac{1}{\tau_\eta} I(3 \times 3) & 3 \end{array} \tag{21}$$

and

$$K(9 \times 9) = \begin{array}{c} \begin{array}{cc} \qquad 6 \qquad & \qquad 3 \qquad \end{array} \\ \left[\begin{array}{c:c} \qquad\qquad & \qquad\qquad \\ \hdashline \qquad\qquad & \left(2\,\frac{\sigma_\eta^2}{\tau_\eta}\right) I(3 \times 3) \end{array}\right] \end{array} \begin{array}{c} 6 \\ 3 \end{array} \qquad (22)$$

5. Results

a. The results from two successive passes of data and the sensitivity to process noise. Consider the tracking station of *Subsection 4* observing a distant space probe, and assume that the station completes two successive 12-h passes of data. The probe is at a distance of 10^8 km from the earth, has a geocentric declination of 20 deg, and is assumed to be travelling directly away from the earth. The *a priori* values of the probe state accuracies are given as

$$\sigma_{u_0} = \sigma_{v_0} = \sigma_{w_0} = 1 \text{ km/s}$$

$$\sigma_{x_0} = \sigma_{y_0} = \sigma_{z_0} = 10^6 \text{ km}$$

which are large enough not to influence the accuracy of estimates from the data after the beginning of the second pass. The standard deviation of the noise in the counted doppler data is taken as 1 m, and the correlation time of the noise is taken as 1000 s, which is of the same order of magnitude as the round-trip light travel time between the earth and the probe. Plots of the time history of the estimation accuracies of the probe state ($\sigma_u, \sigma_v, \sigma_w, \sigma_y, \sigma_z$) are given in Figs. 13–17. The time span in these figures includes the first 12-h pass, the 12-h time span when the station is unable to observe the probe (overnight), and the second 12-h pass. The total time span is thus 36 h. Curves are present for the following values of process noise standard deviation:

$\sigma_\eta = 0$ — the ballistic case, where no random accelerations are assumed to act on the probe.

$\sigma_\eta = 10^{-7}$ cm/s^2
$\sigma_\eta = 10^{-6}$ cm/s^2 — These accelerations are of the order of magnitude of those due to random solar disturbances and leakage in any gas jets on board the spacecraft.

$\sigma_\eta = 10^{-5}$ cm/s^2

$\sigma_\eta = 0.5 \times 10^{-4}$ cm/s^2
$\sigma_\eta = 10^{-4}$ cm/s^2
$\sigma_\eta = 2 \times 10^{-4}$ cm/s^2 — These accelerations are of the order of magnitude of those due to errors in the thrust magnitude and direction program of a solar-electrically thrusted space vehicle.

The correlation time of the process noise is taken as 1000 s, which is representative of short-term fluctuations in the performance of a low-thrust engine or attitude control system. It should be noted that the accuracies in Figs. 13–17 are not particularly sensitive to the correlation time of the process noise, and that the process noise cannot be effectively estimated from the tracking data to any degree better than the *a priori* standard deviation.

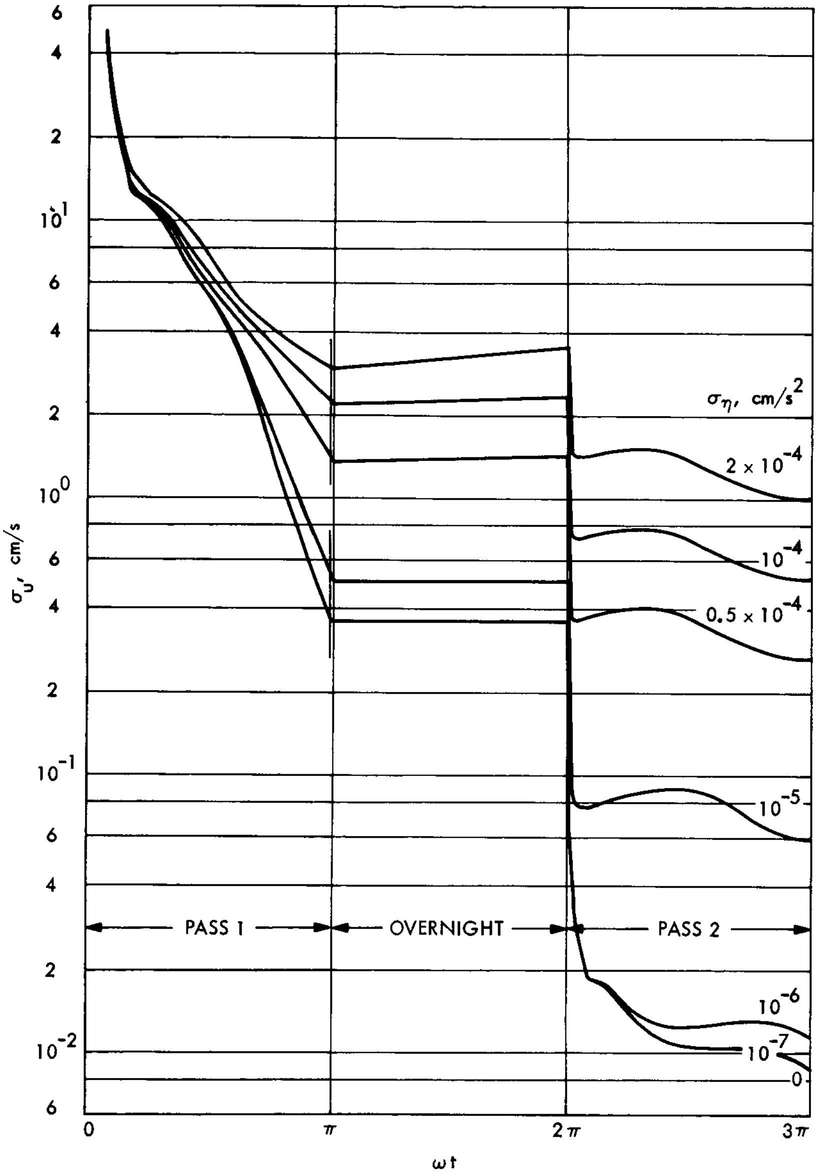

Fig. 13. Range-rate uncertainty time history

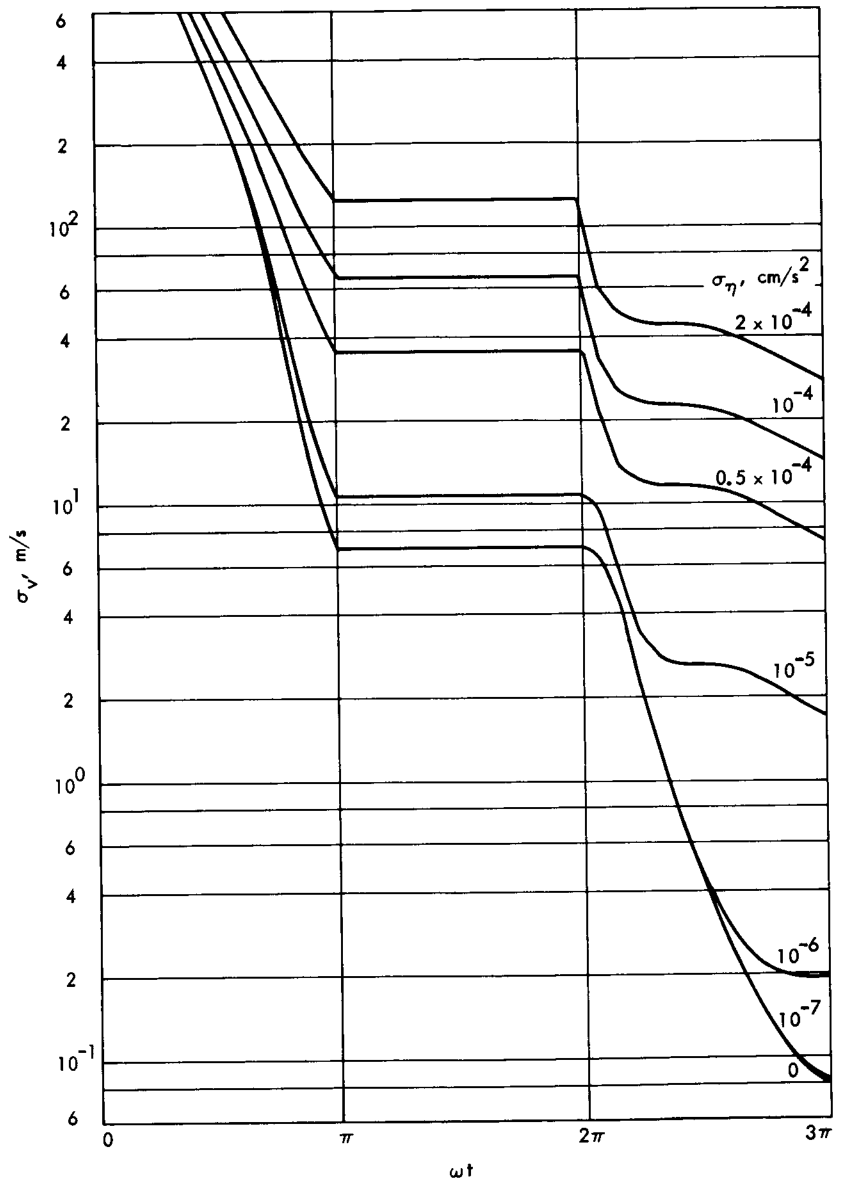

Fig. 14. Lateral velocity uncertainty time history—right ascension direction

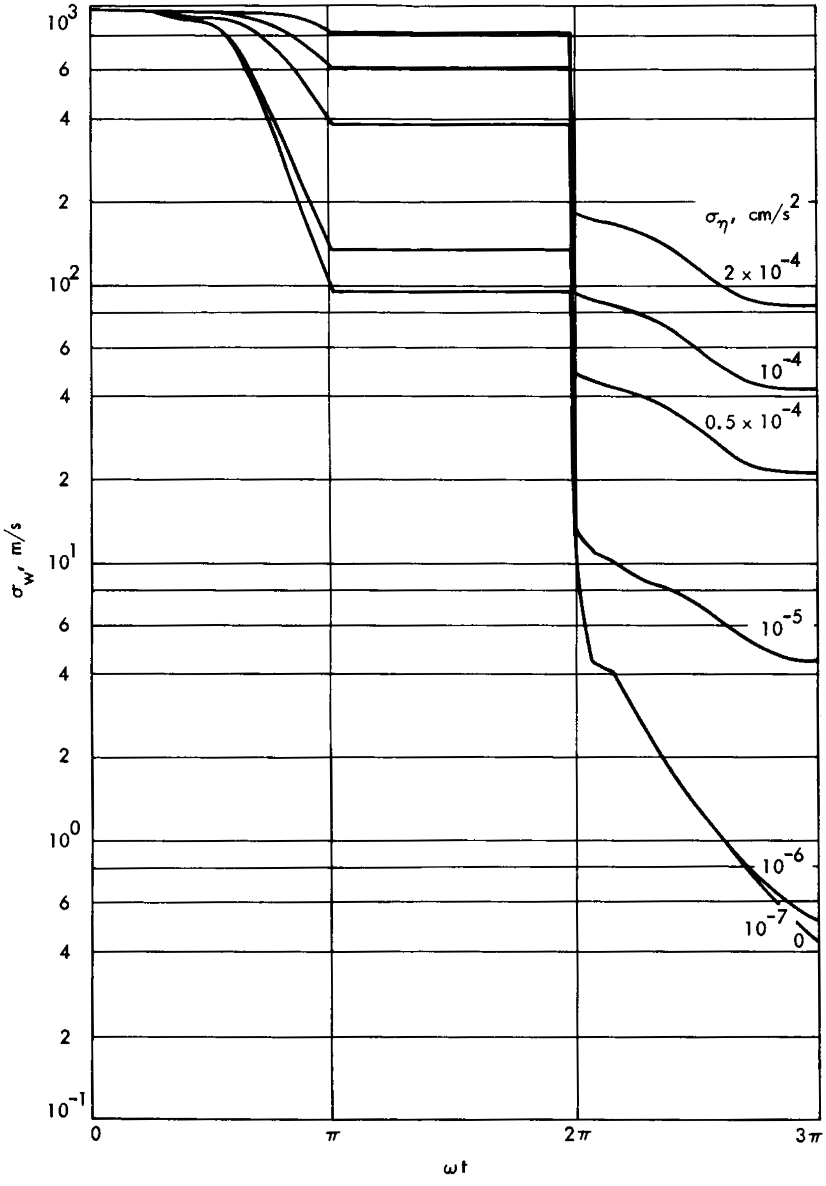

Fig. 15. Lateral velocity uncertainty time history—declination direction

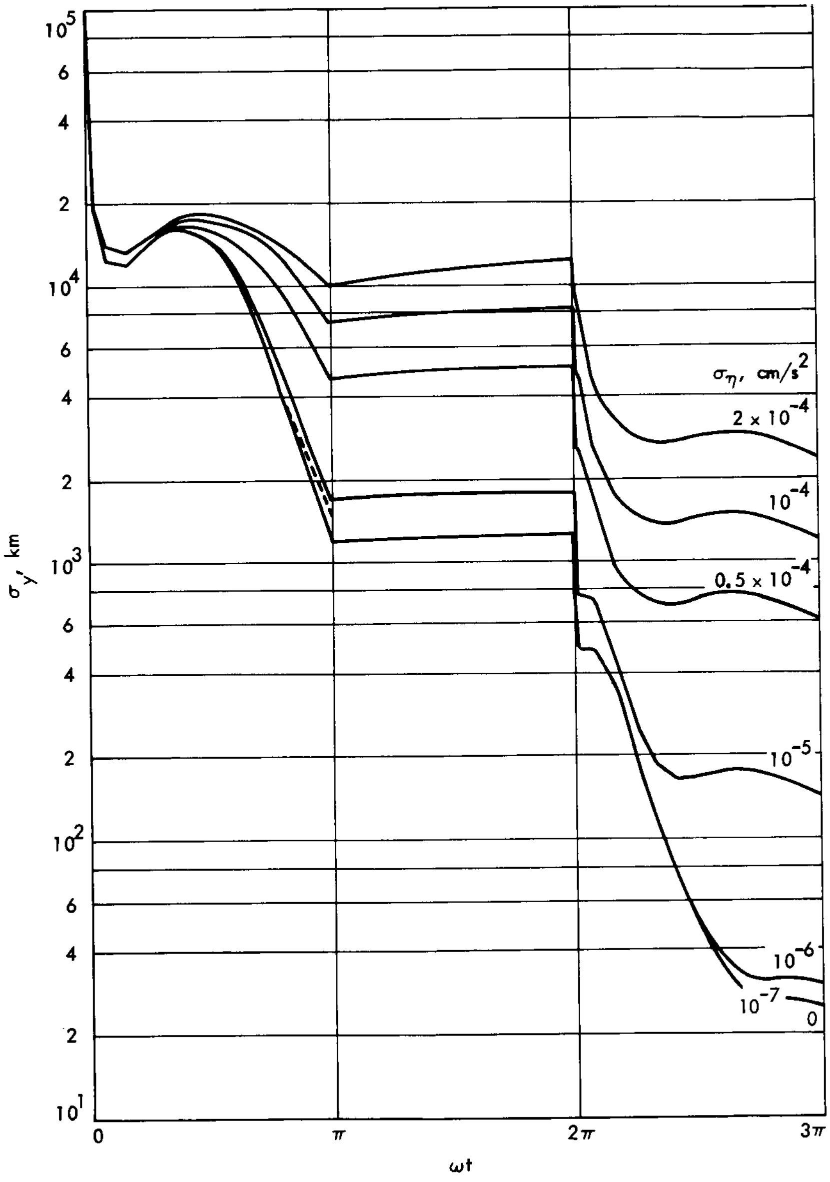

Fig. 16. Lateral position uncertainty time history—right ascension

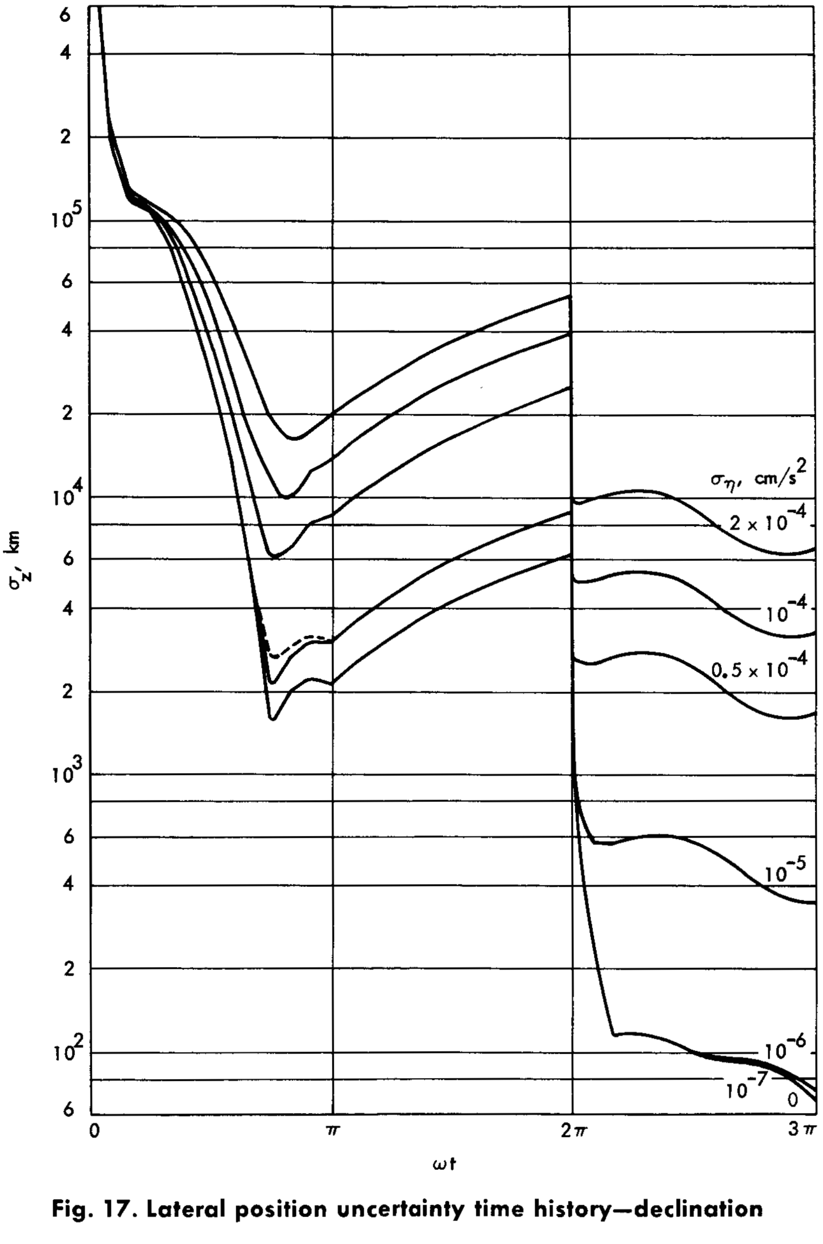

Fig. 17. Lateral position uncertainty time history—declination

It should also be noted that the data noise cannot be effectively estimated better than the *a priori* accuracy.

It is immediately evident from the curves in Figs. 13–17 that high-level process noise ($\sigma_\eta = 0.5, 1, 2 \times 10^{-4}$ cm/s^2) degrades the accuracy of estimates to all 5 parameters during the first pass of data and continues to degrade the accuracy through the second pass to a value about 2 orders of magnitude higher than the ballistic case. Low-level process noise ($\sigma_\eta = 10^{-6}, 10^{-7}$ cm/s^2) has little degrading effect on the accuracy of estimates even through the second pass. It should be noted that a high correlation exists between the errors in the estimates of several of the state parameters at the end of pass 1. Some of these high correlations are due to the similarity in form of the partial derivatives in Expression (12). Others result from the natural correlation between the velocity and displacement along any direction. Pass 2 data aids in separating the parameter estimates such that no correlation greater than 0.85 exists between estimation errors. This separation accounts for the remarkable improvement in the estimation accuracies during pass 2. Note the dashed line in Fig. 16 during pass 1. This represents the degradation in the ballistic case accuracy due to a 50-m uncertainty in the longitude of the station. None of the other parameters is affected. The dashed line during pass 1 in Fig. 17 represents the effect of a 50-m uncertainty in the station's distance from the earth's spin axis. It can be concluded that the effects of large station location uncertainties and low-level process noise (solar disturbances, and onboard gas leakage) are small compared with the effects of large process noise. This does not mean that such uncertainties should be ignored in estimation schemes when large noise is expected to occur, but that their effects have negligible influence on the accuracy of state parameter estimates. It can be seen from the curves that all of the state uncertainties for large process noise appear to vary directly with the standard deviation of the process noise.

b. The results from several successive passes of data. Figure 18 illustrates the accuracy of the range-rate estimates for high-level process noise as a function of the number of successively completed passes, *N*. The results are extended to include 10 passes. It is evident that the large degree of improvement between passes 1 and 2 does not continue as more passes of data are obtained. This same characteristic exists for estimates of the other state variables. After pass 2, σ_u, σ_y, and σ_z decrease by a factor of $(2/N)^{1/2}$, while σ_v and σ_w decrease as $[(2/N)^3]^{1/2}$.

c. Sensitivity of the results to the position of the probe. The results of *Subsection 5b* are given for a probe at a distance of 10^8 km from the earth at a declination of 20 deg. As shown in SPS 37-52, Vol. II, pp. 37–44, the parameters sensitive to the declination are v and z. After the initiation of pass 2, w and z vary with the reciprocal of sin δ_0. The other state variables are not affected by changes in the declination. It should also be noted that the accuracies of lateral state variables v, w, y, and z all vary linearly with the distance of the probe from earth, r.

d. Sensitivity of the results to the velocity of the probe. In the results of *Subsection 5b*, the probe has been assumed to travel directly away from the earth, that is, the *a priori* direction of motion of the probe is along the x axis. If the probe, in fact, travels with an appreciable

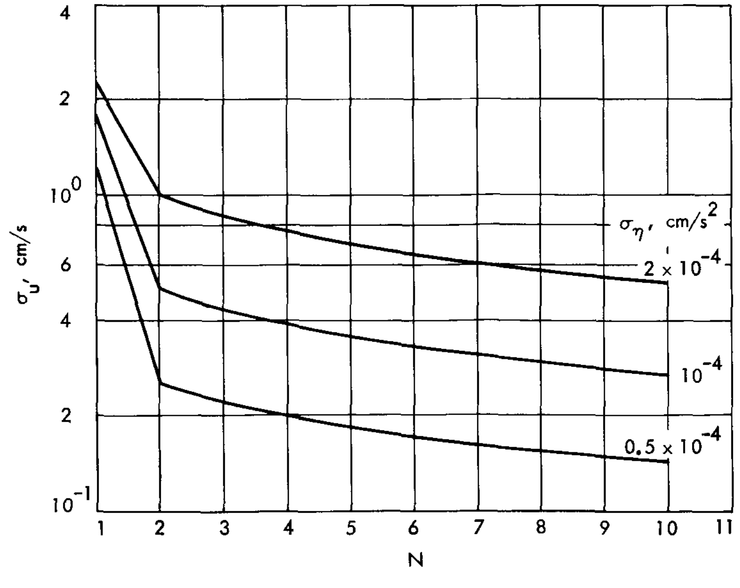

Fig. 18. Range-rate uncertainty time history, 10 passes of data

velocity lateral to the earth–probe direction, then the range-rate uncertainty σ_u is degraded severely.

Figure 19 illustrates the dependency of σ_u on v, the velocity along the right ascension direction. Curves are shown for $v = 0$, 5, and 10 km/s (w is zero for the curves shown). Figure 20 illustrates the sensitivity of the time history of σ_x to v. The presence of nonzero values of v degrades the estimation accuracy of u but makes possible the estimation of the range x. Similar results occur for nonzero values of w. It should be noted that the uncertainties of the rest of the state parameters are not affected by the presence of a lateral velocity.

6. Conclusion

The results of this article are presented in order to illustrate process noise and geometrical influences on the behavior of the accuracies of the state estimates. An examination of the figures shown and others from the continuous estimation program yields the following empirical formulas, which illustrate the state uncertainty behavior after N completed passes of data ($N \geqq 2$)

$$
\begin{aligned}
\sigma_u &= \left[\left(\frac{v}{r}\right)^2 \sigma_y^2 + \left(\frac{w}{r}\right)^2 \sigma_z^2\right]^{1/2} \text{ m/s} \\
\sigma_v &= \sigma_\eta \left[\left(\frac{2}{N}\right)^3\right]^{1/2} (r)\, 1.5 \times 10^{-10} \text{ m/s} \\
\sigma_w &= \sigma_\eta \left[\left(\frac{2}{N}\right)^3\right]^{1/2} (r)\, \frac{1}{\sin \delta_0}\, 1.5 \times 10^{-10} \text{ m/s} \\
\sigma_x &= 2 \left[\left(\frac{r}{v}\right)^2 \sigma_v^2 + \left(\frac{r}{w}\right)^2 \sigma_w^2\right]^{1/2} \text{ m} \\
\sigma_y &= \sigma_\eta \left(\frac{2}{N}\right)^{1/2} (r)\, 10^{-5} \text{ m} \\
\sigma_z &= \sigma_\eta \left(\frac{2}{N}\right)^{1/2} (r)\, \frac{1}{\sin \delta_0}\, 10^{-5} \text{ m}
\end{aligned}
\qquad (23)
$$

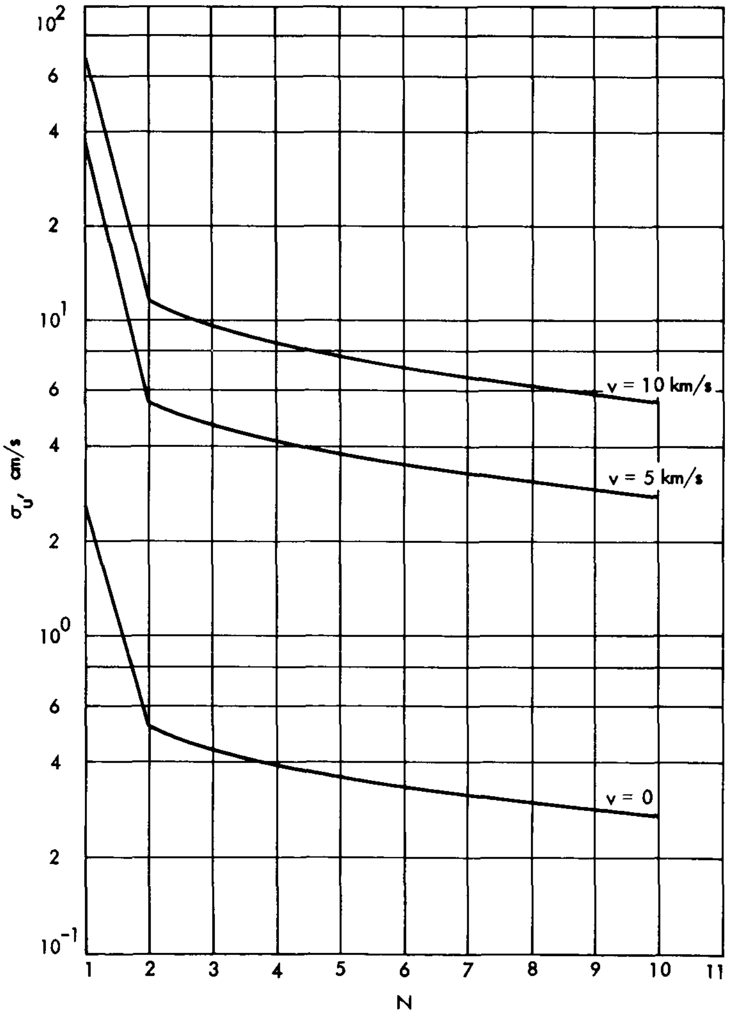

Fig. 19. Sensitivity of range-rate uncertainty to velocity in right ascension direction

Fig. 20. Sensitivity of range uncertainty to velocity in right ascension direction

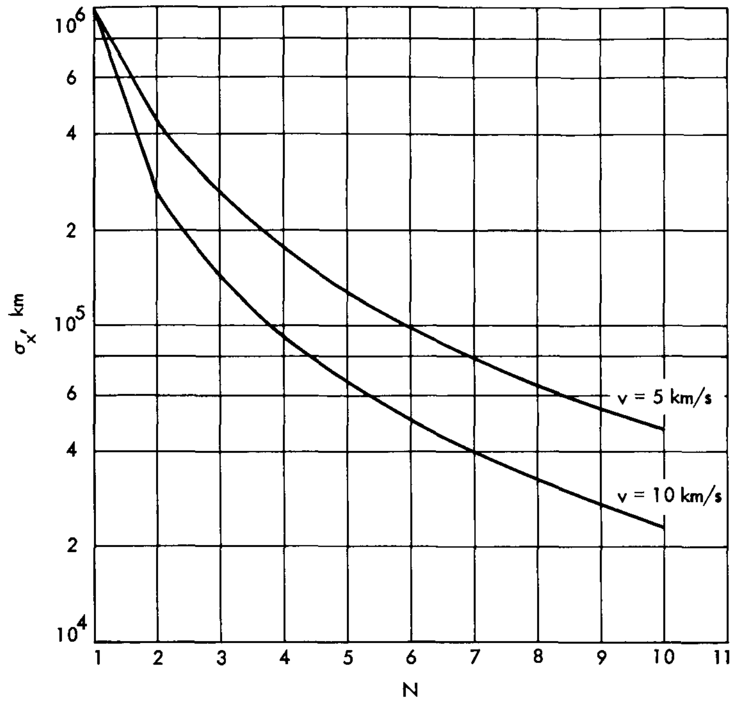

where the earth–probe distance, *r*, is specified in meters, the lateral velocities, *v* and *w*, are specified in meters per second, and the process noise standard deviation, $\sigma\eta$, is specified in cm/s^2 $\times$ 10^{-4}. The formulas are accurate for reasonable lateral velocities (up to 25 km/s at 10^8 km from earth), and are valid up to about 10 successive passes of data. It should be noted that the probe must be relatively free from planetary gravitational forces and be at an appreciable distance from the sun (>1.5 AU). It should also be noted that the entire state information is expressed in terms of covariance matrix of the errors in the state estimates, i.e.

$$\Lambda_N(6 \times 6) = \begin{bmatrix} \sigma_u^2 & \alpha_{uv} & \alpha_{uw} & \alpha_{ux} & \alpha_{uy} & \alpha_{uz} \\ & \sigma_v^2 & \alpha_{vw} & \alpha_{vx} & \alpha_{vy} & \alpha_{vz} \\ & & \sigma_w^2 & \alpha_{wx} & \alpha_{wy} & \alpha_{wz} \\ & & & \sigma_x^2 & \alpha_{xy} & \alpha_{xz} \\ \text{symmetric} & & & & \sigma_y^2 & \alpha_{yz} \\ & & & & & \sigma_z^2 \end{bmatrix}$$

and that the off-diagonal terms of $\Lambda_N(N \geqq 2)$ are such that none of the correlations exceed 0.85.

Reference

1. Kalman, R. E., *New Methods and Results in Linear Prediction and Filtering Theory*, Technical Report 61-1. Martin-Marietta Corp., Research Institute for Advanced Studies, Baltimore, Maryland, 1961.

F. Data Compression and Its Application to Orbit Determination, *P. Dyer and S. R. McReynolds*

1. Introduction

In many applications of estimation theory, especially where nonlinear techniques are employed, a serious problem may be caused by a superabundance of data. Too many data may require an inordinately large amount of computer time for processing and also accentuate numerical inaccuracies. It is, however, clearly undesirable to throw away information to increase numerical accuracy and reduce computer times.

The technique of data compression is designed to handle these difficulties without significantly reducing the information contained in the data. It is based on preprocessing the data to produce new compressed data that retain all the original information. The filter then acts on the compressed data. Naturally the most benefit is obtained when this preprocessing is rapid and cheap and the filter is slow and expensive.

This article discusses some general data compression techniques which are then applied to the processing of doppler data from an earth–Mars space probe.

2. Fundamental Concept

The basic model for the original set of measurements is given by

$$z(t) = h[x(t), t] + v(t) \qquad (1)$$

where

$z(t)$ = scalar measurements at time, t

$v(t)$ = measurement noise at time, t

$x = (x_1, x_2, \cdots, x_n)$ = state of the system

It is assumed that $v(t)$ is white noise, with

$$\left.\begin{aligned} E(v) &= 0 \\ E[v(t)v(\tau)] &= R(t)\,\delta(t-\tau) \end{aligned}\right\} \qquad (2)$$

where $R(t) > 0$.

In applying the data compression technique, it is assumed that a linear finite time expansion for $h[x(t), t]$ exists over the time interval of interest, $(0, T)$. Hence, Eq. (1) can be written

$$z = \sum_{i=1}^{N} \{a_i(x)\, P_i(t)\} + v(t) \qquad 0 \leq t \leq T \qquad (3)$$

where N is a relatively small number and $P_i(t)$ are given functions of time. The coefficients a_i must now be estimated. The least-squares estimate of $a = (a_1, a_2, \cdots, a_N)$ is given by

$$\hat{a} = -J^{-1}d \qquad (4)$$

where J is the $N \times N$ matrix defined by

$$J_{ij} = \int_0^T [R^{-1}(t)\, P_i(t)\, P_j(t)]\, dt \qquad (5)$$

and d is the N vector defined by

$$d_i = \int_0^T [R^{-1}(t)\, P_i(t)\, z(t)]\, dt \qquad (6)$$

The covariance associated with the estimate of the parameters $\hat{a}$ [Eq. (4)], denoted by Λ, is given by

$$\Lambda = J^{-1} \qquad (7)$$

Thus, the original data have been reduced to a collection of N parameters with known statistics. The next step is to obtain estimates of the state of the system, x.

There are two possible alternatives. In the first, the parameters $a = (a_1, \cdots, a_n)$ are regarded as the new data. This approach assumes that the parameters, $\hat{a}$, are known functions of the state and that the partial derivatives $\partial a_i/\partial x_j$ may be easily obtained. The other approach, the one favored here, is to use the expansion Eq. (3) to generate new data $\hat{Z}$ where

$$\hat{Z}(t_j) = \sum_{i=1}^{N} \hat{a}_i(t_j)\, P_i(t_j) \qquad j = (1, 2, \cdots, N) \qquad (8)$$

where the t_i

$$0 \leq t_1 < t_2 < \cdots < t_N \leq T$$

are chosen so that the matrix, A

$$A_{ij} = P_i(t_j) \qquad (9)$$

has full rank. Obviously the compressed data $\hat{Z}(t_j)$, $j = (1, 2, \cdots, N)$, retains all the information in the parameters, a. The advantage of this approach is that the new compressed data are of the same type as the original data.

However, it is apparent that the new compressed data are correlated, i.e., the covariance matrix associated with the new data, Q, where

$$Q = A^T J^{-1} A \tag{10}$$

is *not* a diagonal matrix.

Hence, all of the compressed data points must be processed together which tends to complicate the standard sequential filter.

3. Data Fitting

The unknown parameters in the data expansion model must now be estimated. These parameters will be estimated in either a least-squares or weighted least-squares sense. Unfortunately, there will often be a high correlation between the parameters, which has a detrimental effect on the normal least-squares fitting routines. In the examples given below, the effect is so severe that meaningful solutions cannot be obtained even by using double-precision arithmetic. A much more rewarding approach is founded on the application of Householder (orthogonal) transformations.

Suppose that an n-dimensional vector x is to be found such that

$$J = ||Ax - z||^2 \tag{11}$$

is a minimum. Here, z is an r-dimensional vector (measurements) and A is an $r \times n$ matrix (partials). The Householder algorithm constructs an orthogonal transformation P such that

$$PA = \begin{array}{c} n \\ \left[\begin{array}{c} R \\ \hdashline 0 \end{array}\right] \end{array} \begin{array}{l} \\ n \\ r \end{array} \tag{12}$$

where R is an upper triangular matrix. The transformation is also applied to z to form the n-vector b_1 where

$$PZ = \left[\begin{array}{c} b_1 \\ \hdashline b_2 \end{array}\right] \begin{array}{l} n \\ r - n \end{array} \tag{13}$$

Provided R has full rank, the least-squares estimate of x is given by

$$\bar{x} = R^{-1} b_1 \tag{14}$$

As the matrix R is upper triangular, the inversion required to form $\bar{x}$ is trivial and essentially free from numerical errors. If the vector z represents measurements corrupted with gaussian noise having zero mean and variance σ^2, the covariance Λ associated with the estimate is given by

$$\Lambda = \sigma^2 \left(R^{-1} R^{-1^T}\right) \tag{15}$$

The equivalent solution obtained by the conventional formulation is

$$\bar{x} = (A^T A)^{-1} A^T Z \tag{16}$$

with the covariance given by

$$\Lambda = \sigma^2 (A^T A)^{-1} \tag{17}$$

The difference between the techniques is that the Householder algorithm avoids the formation of the matrix $A^T A$. Clearly, if the matrix A is badly conditioned, the matrix $A^T A$ will be twice as badly conditioned.

The mechanization of the Householder transformation has been adequately described in the literature.[5]

4. Compression of Doppler Data from a Distant Spacecraft

Next, data compression will be applied to doppler data from a distant spacecraft. It will be assumed that the spacecraft is in its heliocentric coast phase. This situation lends itself to a simple expansion as suggested by T. W. Hamilton and W. G. Melbourne (SPS 37-39, Vol. III, pp. 18–23), and D. W. Curkendall and S. R. McReynolds (Ref. 1).

Doppler data, $\dot{\rho}$, from a distant spacecraft can be expressed as

$$\dot{\rho} = \frac{(\mathbf{r}_1 - \mathbf{r}_0) \cdot (\dot{\mathbf{r}}_1 - \dot{\mathbf{r}}_0)}{|\mathbf{r}_1 - \mathbf{r}_0|} \tag{18}$$

---

[5] See also: Hanson, R. J., and Lawson, C. L., *Extensions and Applications of the Householder Algorithm for Solving Linear Least-Squares Problems,* July 12, 1968 (JPL internal document).

where

$\mathbf{r}_1$ = position of the probe in geocentric coordinates

$\mathbf{r}_0$ = position of the observer in geocentric coordinates

Now it is assumed that the parameter $\epsilon = |\mathbf{r}_0|/|\mathbf{r}_1|$ is small. Hence, expanding Eq. (18) in terms of ϵ yields

$$\dot{p} = a_0 + \sum_{i=1}^{\infty} \epsilon^{i-1}\left[a_i \sin(i\,\omega t) + b_i \cos(i\,\omega t)\right] \qquad (19)$$

where the a_i and b_i are functions of the position of the space probe and the parameter ω is the rotational frequency of the earth. Since the parameters a_i and b_j are changing slowly, it is appropriate to expand them in a time series, i.e.

$$a_0 = a_0(t_0) + \dot{a}_0(t_0)(t - t_0) + \frac{1}{2}\ddot{a}(t_0)(t - t_0)^2 \qquad (20)$$

Thus, the final expansion consists of a Fourier series combined with secular terms. The series converges extremely rapidly and the number of terms required decreases as the distance to the space probe increases.

5. Some Results

All the results relate to a *Mariner* Mars 1969-type trajectory with simulated data generated by the single precision orbit determination program (SPODP) and the double precision orbit determination program (DPODP). One pass of data (approximately 11 h of tracking) was processed at a time using the series

$$\dot{p} = a_0 + a_{01}t + a_{02}t^2 + \sum_{i=1}^{3}\{\, a_i \sin(i_\omega t) + b_i \cos(i_\omega t)\,\}$$

$$+\, a_{11}t \sin(\omega t) + b_{11}t\cos(\omega t) \qquad (21)$$

Since it is somewhat impracticable to include all the results here, only a few representative cases will be given.

(1) The first pass corresponded to an earth–probe distance > 1 AU so that the parameter ϵ was extremely small. The relative probe velocity was about 15 km/s, the data were given to 10^{-2} Hz, and there were 600 doppler points at 1 min intervals. The residuals (the difference between the given data and data generated by the expansion) are shown in Fig. 21. The average deviation is 4×10^{-3} Hz.

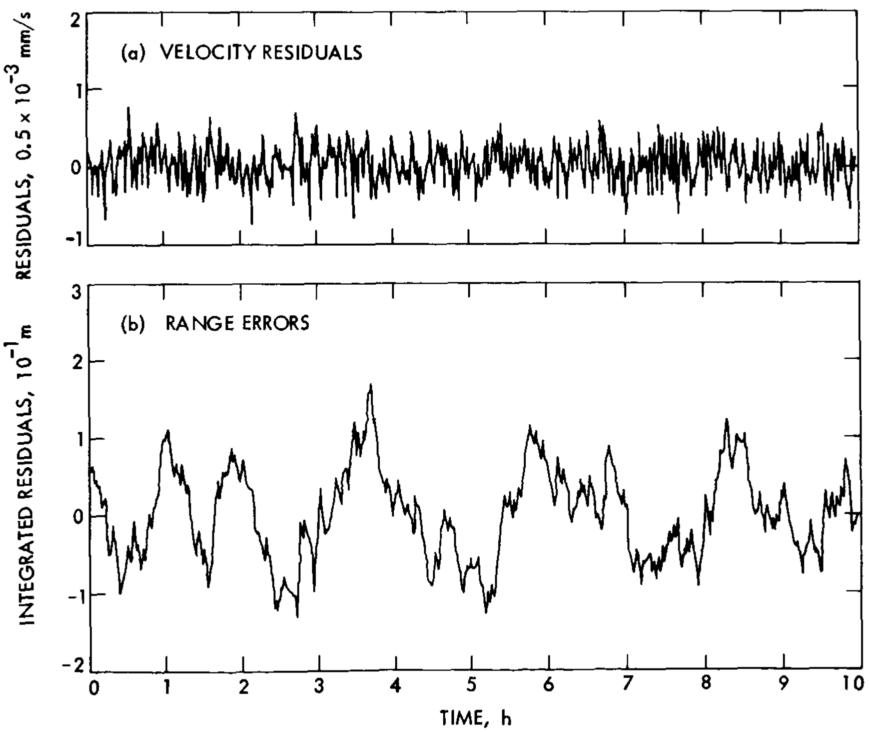

Fig. 21. Far-earth data

(2) The second case corresponded to a near-earth situation (a range of 0.03 AU). The relative probe velocity was approximately 3.5 km/s, the data were given to 10^{-3} Hz, and there were 516 doppler points at 1 min intervals. The data were fitted to 7×10^{-4} Hz (Fig. 22).

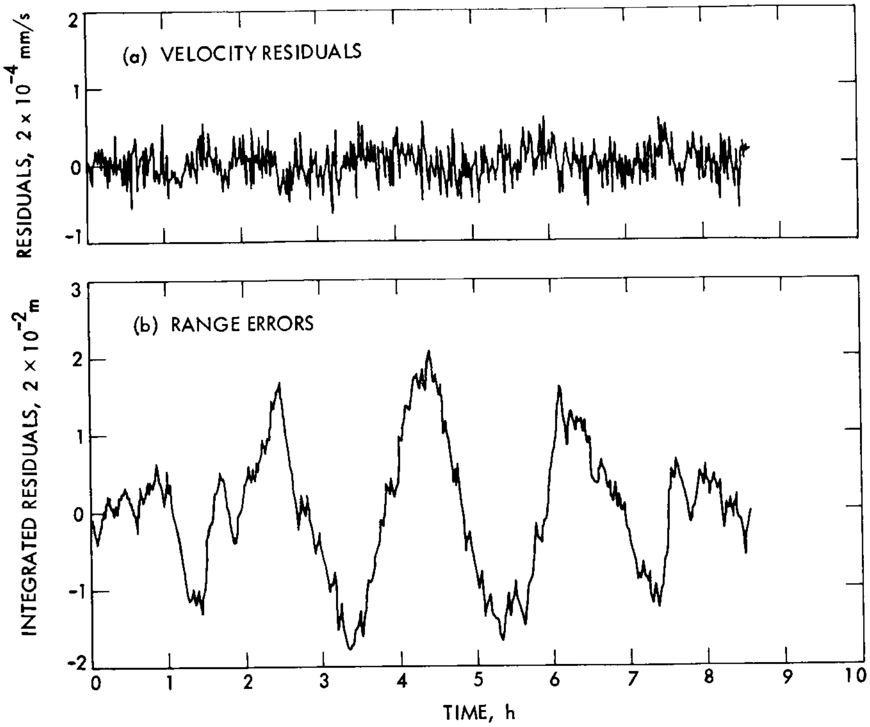

Fig. 22. Near-earth data

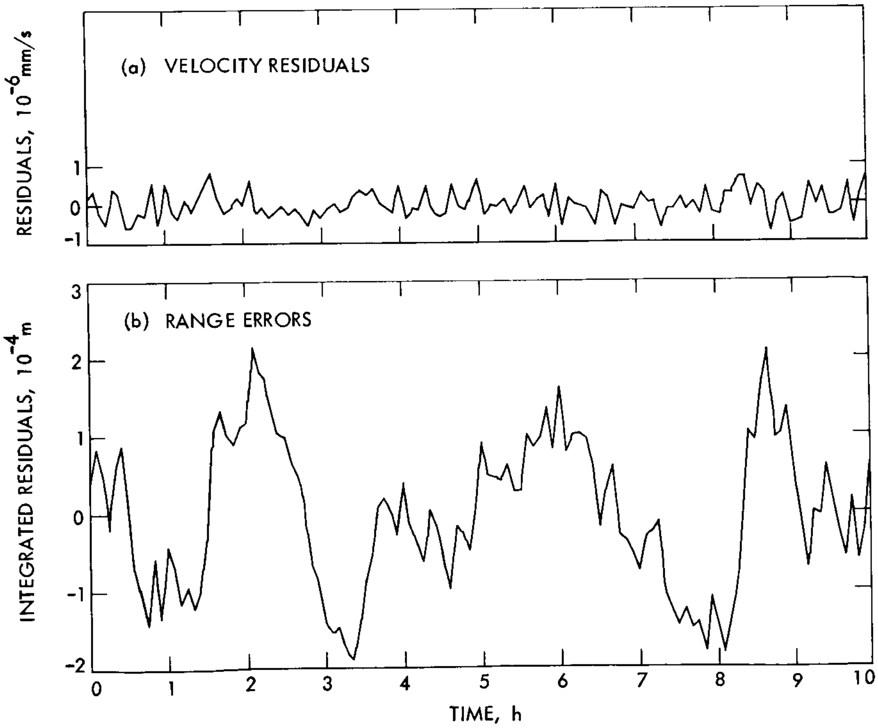

Fig. 23. DPODP data

(3) The above runs were made with data simulated by the SPODP and the accuracy of the fit was limited by the accuracy of the data. Hence, data corresponding to a range of about 0.1 AU were generated by the DPODP. The data were given to 10^{-5} Hz and fitted to 0.36×10^{-5} Hz (Fig. 23).

The error in range (integrated doppler) was also computed for each case and is shown in Figs. 21, 22, and 23 for the respective cases.

The covariance and correlation matrices of the estimated state (X, Y, Z, DX, DY, DZ) generated by the SPODP are shown in Table 5, and used as a reference. First, the covariance Q_0 and the correlation matrices of the estimated state associated with the compressed (correlated) data were computed (Table 6). Comparing Tables 5 and 6, it can be seen that there is essentially two-place agreement, i.e., very little has been lost in the data compression.

However, the existing orbit determination program can only be used with *uncorrelated* data and, as noted above, the compressed data are correlated. Hence, the above computation was repeated assuming that the compressed data were uncorrelated. The resultant covariance, Q_1, and correlation matrices are shown in Table 7. Again, there was good agreement with the SPODP. Finally, the *true*

Table 5. SPODP matrices

Estimated state	*X*	*Y*	*Z*	*DX*	*DY*	*DZ*
			Covariance matrix of estimated parameters			
X	0.27624433 08	0.52235442 08	0.27298892 08	0.34496683 01	−0.22961470 01	−0.25976812 00
Y	0.52235442 08	0.99349065 08	0.51738331 08	0.65333560 01	−0.44855508 01	−0.28575643 00
Z	0.27298892 08	0.51738331 08	0.31470056 08	0.54482548 01	0.79264987 00	−0.83098944 01
DX	0.34496683 01	0.65333560 01	0.54482548 01	0.13765138−05	0.11486907−05	−0.37922410−05
DY	−0.22961470 01	−0.44855508 01	0.79264987 00	0.11486907−05	0.24169919−05	−0.57597110−05
DZ	−0.25976812 00	−0.28575643 00	−0.83098944 01	−0.37922410−05	−0.57597110−05	0.15067777−04
			Correlation matrix of estimated parameters			
X	0.10000000 01	0.99709534 00	0.92586904 00	0.55942305 00	−0.28100587 00	−0.12732526−01
Y	0.99709534 00	0.10000000 01	0.92529831 00	0.55868132 00	−0.28946515 00	−0.73856634−02
Z	0.92586904 00	0.92529831 00	0.10000000 01	0.82778656 00	0.90885589−01	−0.38161211 00
DX	0.55942305 00	0.55868132 00	0.82778656 00	0.99999999 00	0.62976021 00	−0.83268560 00
DY	−0.28100587 00	−0.28946515 00	0.90885589−01	0.62976021 00	0.99999999 00	−0.95441772 00
DZ	−0.12732526−01	−0.73856634−02	−0.38161211 00	−0.83268560 00	−0.95441772 00	0.10000000 01

Table 6. Matrices associated with compressed correlated data

		Q_0 matrix			
0.27055035D 08	0.51160366D 08	0.26694755D 08	0.33595958D 01	−0.22771235D 01	−0.18014859D 00
0.51160366D 08	0.97305227D 08	0.50592826D 08	0.63620601D 01	−0.44476418D 01	−0.13650471D 00
0.26694755D 08	0.50592826D 08	0.30773373D 08	0.53110908D 01	0.75105600D 00	−0.80621996D 01
0.33595958D 01	0.63620601D 01	0.53110908D 01	0.13429518D−05	0.11226450D−05	−0.37032575D−05
−0.22771235D 01	−0.44476417D 01	0.75105602D 00	0.11226450D−05	0.23715205D−05	−0.56456859D−05
−0.18014864D 00	−0.13650480D 00	−0.80621997D 01	−0.37032575D−05	−0.56456859D−05	0.14751730D−04
		Q_0 correlation matrix			
0.10000000D 01	0.99710642D 00	0.92569626D 00	0.55735611D 00	−0.28428183D 00	−0.90174833D−02
0.99710642D 00	0.10000000D 01	0.92509744D 00	0.55654396D 00	−0.29278463D 00	−0.36029485D−02
0.92569626D 00	0.92509744D 00	0.10000000D 01	0.82664709D 00	0.87968159D−01	−0.37861577D 00
0.55735611D 00	0.55654396D 00	0.82664709D 00	0.10000000D 01	0.62906975D 00	−0.83201705D 00
−0.28428182D 00	−0.29278463D 00	0.87968162D−01	0.62906975D 00	0.10000000D 01	−0.95451289D 00
−0.90174858D−02	−0.36029510D−02	−0.37861577D 00	−0.83201705D 00	−0.95451289D 00	0.10000000D 01

covariance Q_2 associated with the latter computation is shown in Table 8 where

$$Q_2 = Q_1 A^T W^{-1} W_2 \; W^{-1} A Q_1 \qquad (22)$$

and

W = diagonal weighting matrix associated with Q_1

W_0 = true weighting matrix

A = matrix of partial derivatives

Scanning the diagonal terms of Table 7 and comparing them with those in Table 5, it can be concluded that the loss of accuracy accrued by making the uncorrelated assumption is, at most, approximately 25%. This is not thought to be a large loss in efficiency, particularly when it is recognized that the original assumption of uncorrelated raw doppler noise is tenuous at best. Indeed, the relatively weak dependence of estimator efficiency upon the correlation model assumed might be considered an encouraging result.

However, the changes required to allow the fitting of data in correlated blocks is not a large task and would make complete the machinery required to process the compressed data and obtain nearly identical results as with the original raw data set.

Reference

1. Curkendall, D. W., and McReynolds, S. R., *A Simplified Approach for Determining the Information Content and Critical Error Sources of Earth-Based Radio Tracking Data,* paper presented at the AAS/AIAA Astrodynamics Specialists Conference, Jackson Lake Lodge, Wyo., Sept. 3–5, 1968.

Table 7. Matrices associated with compressed data assumed to be uncorrelated

<table>
<tr><th colspan="6">Q_1 matrix</th></tr>
<tr><td>0.27817694D 08</td><td>0.52519071D 08</td><td>0.28515386D 08</td><td>0.39783219D 01</td><td>−0.15431637D 01</td><td>−0.22637695D 01</td></tr>
<tr><td>0.52519071D 08</td><td>0.99925854D 08</td><td>0.54020088D 08</td><td>0.75342083D 01</td><td>−0.30922877D 01</td><td>−0.40347433D 01</td></tr>
<tr><td>0.28515386D 08</td><td>0.54020088D 08</td><td>0.34064102D 08</td><td>0.62641611D 01</td><td>0.16810062D 01</td><td>−0.10922235D 02</td></tr>
<tr><td>0.39783219D 01</td><td>0.75342083D 01</td><td>0.62641611D 01</td><td>0.15808552D−05</td><td>0.13107363D−05</td><td>−0.43393416D−05</td></tr>
<tr><td>−0.15431637D 01</td><td>−0.30922877D 01</td><td>0.16810062D 01</td><td>0.13107363D−05</td><td>0.24661157D−05</td><td>−0.60502795D−05</td></tr>
<tr><td>−0.22637694D 01</td><td>−0.40347433D 01</td><td>−0.10922235D 02</td><td>−0.43393416D−05</td><td>−0.60502795D−05</td><td>0.16274768D−04</td></tr>
<tr><th colspan="6">Q_1 correlation matrix</th></tr>
<tr><td>0.10000000D 01</td><td>0.99613347D 00</td><td>0.92633957D 00</td><td>0.59991996D 00</td><td>−0.18631367D 00</td><td>−0.10639329D 00</td></tr>
<tr><td>0.99613347D 00</td><td>0.10000000D 01</td><td>0.92590810D 00</td><td>0.59944956D 00</td><td>−0.19698549D 00</td><td>−0.10005057D 00</td></tr>
<tr><td>0.92633957D 00</td><td>0.92590810D 00</td><td>0.10000000D 01</td><td>0.85362752D 00</td><td>0.18340624D 00</td><td>−0.46388001D 00</td></tr>
<tr><td>0.59991996D 00</td><td>0.59944956D 00</td><td>0.85362752D 00</td><td>0.10000000D 01</td><td>0.66383871D 00</td><td>−0.85550075D 00</td></tr>
<tr><td>−0.18631367D 00</td><td>−0.19698549D 00</td><td>0.18340624D 00</td><td>0.66383871D 00</td><td>0.10000000D 01</td><td>−0.95501746D 00</td></tr>
<tr><td>−0.10639329D 00</td><td>−0.10005057D 00</td><td>−0.46388001D 00</td><td>−0.85550075D 00</td><td>−0.95501746D 00</td><td>0.10000000D 01</td></tr>
</table>

Table 8. True covariance matrices associated with compressed data

<table>
<tr><th colspan="6">Q_2 matrix</th></tr>
<tr><td>0.32324257D 08</td><td>0.61052784D 08</td><td>0.32522296D 08</td><td>0.43274036D 01</td><td>−0.22427413D 01</td><td>−0.14570137D 01</td></tr>
<tr><td>0.61052784D 08</td><td>0.11618031D 09</td><td>0.61626303D 08</td><td>0.81960840D 01</td><td>−0.44420385D 01</td><td>−0.24697827D 01</td></tr>
<tr><td>0.32522296D 08</td><td>0.61626303D 08</td><td>0.38024284D 08</td><td>0.67548272D 01</td><td>0.13288746D 01</td><td>−0.10916255D 02</td></tr>
<tr><td>0.43274036D 01</td><td>0.81960840D 01</td><td>0.67548272D 01</td><td>0.16917538D−05</td><td>0.13843103D−05</td><td>−0.46111679D−05</td></tr>
<tr><td>−0.22427413D 01</td><td>−0.44420385D 01</td><td>0.13288746D 01</td><td>0.13843103D−05</td><td>0.27771064D−05</td><td>−0.66970008D−05</td></tr>
<tr><td>−0.14570137D 01</td><td>−0.24697827D 01</td><td>−0.10916255D 02</td><td>−0.46111679D−05</td><td>−0.66970008D−05</td><td>0.17771103D−04</td></tr>
<tr><th colspan="6">Q_2 correlation matrix</th></tr>
<tr><td>0.10000000D 01</td><td>0.99626514D 00</td><td>0.92765482D 00</td><td>0.58518684D 00</td><td>−0.23671111D 00</td><td>−0.60791403D−01</td></tr>
<tr><td>0.99626514D 00</td><td>0.10000000D 01</td><td>0.92719126D 00</td><td>0.58461716D 00</td><td>−0.24729754D 00</td><td>−0.54354474D−01</td></tr>
<tr><td>0.92765482D 00</td><td>0.92719126D 00</td><td>0.10000000D 01</td><td>0.84219981D 00</td><td>0.12931747D 00</td><td>−0.41993876D 00</td></tr>
<tr><td>0.58518684D 00</td><td>0.58461716D 00</td><td>0.84219981D 00</td><td>0.10000000D 01</td><td>0.63865838D 00</td><td>−0.84097901D 00</td></tr>
<tr><td>−0.23671111D 00</td><td>−0.24729754D 00</td><td>0.12931747D 00</td><td>0.63865838D 00</td><td>0.10000000D 01</td><td>−0.95329409D 00</td></tr>
<tr><td>−0.60791403D−01</td><td>−0.54354474D−01</td><td>−0.41993876D 00</td><td>−0.84097901D 00</td><td>−0.95329409D 00</td><td>0.10000000D 01</td></tr>
</table>

III. Advanced Engineering: Communications System Research

A. Radar Observations of Icarus, *R. M. Goldstein*

1. Introduction

Bistatic radar observations of the asteroid Icarus were made on June 14, 1968, when its orbit came within four million miles of earth. Icarus comes this close to earth only once in 19 years, and this recent approach was the first opportunity for radar study. RF spectral measurements of the echoes provide data dependent on the size, shape, spin, velocity, and radar cross section of the target. It is estimated that the radius is between 0.3 and 0.6 km and the rotation period is between 1.5 and 3.3 h.

Icarus is an extremely difficult radar target. Its radar detectability is only 10^{-3} times that of Mercury (at closest approach) and 10^{-12} that of the moon. Only the most powerful and sensitive radars of modern technology can detect Icarus.

2. Experiment

This experiment demonstrated the capability of the new 450-kW transmitter on the Venus DSS 85-ft antenna, combined with the 210-ft antenna at the Mars DSS as the receiving antenna. The Mars DSS is approximately 14 mi away from the transmitter. Because of this separation, it was possible to transmit and receive simultaneously most of the time. However, when the elevation angle was low, or during the several hours of closest approach when the doppler went through zero, it was necessary to transmit and receive in alternate cycles. Each cycle lasted 43 s, the round-trip time of transmission.

The radar station parameters for this experiment are as follows:

Power	450 kW
Frequency	2388 MHz
Two-way antenna gain	116.0 dB
System temperature	21°K

Pure monochromatic waves were beamed at Icarus. The frequency spectrum of the weak echoes was measured at the receiver, using correlation techniques. Any rotation that Icarus might have would broaden the spectrum of the echo and leave a characteristic pattern.

Three functions of the radar were controlled by ephemerides:[1] pointing of the 85-ft antenna, pointing of

---

[1] Recent accurate ephemerides provided by G. Null and D. Holdridge of JPL and S. Herrick of UCLA; critical optical observation of Icarus supplied by E. Roemer, University of Arizona.

the 210-ft antenna, and tuning of the receiver to account for the relative velocities of Icarus and the tracking station.

Ordinarily, receiver runs of 30 min were made, and the resulting spectrum was displayed. Because of the unusually low power level of the echo, none of these runs produced a clear detection of Icarus. Although there were indications of an echo, they were obscured by the random fluctuations of the spectra.

3. Measurements

When 4 h of data were averaged, however, the result was not only positive detection of Icarus, but also an indication of power, bandwidth, and center frequency. Altogether seven such average spectra were taken. They are reproduced in Fig. 1. Each is the result of 3 to 4 h of averaging.

The radar was calibrated by directing it at the planet Mercury, leaving everything unchanged except for the three ephemerides. Figure 2 is a sample result of averaging 9 min of echoes from Mercury. Note the different scale in frequency.

The total received power is obtained from the area under each spectrum. An average echo power of 0.63×10^{-22} W was obtained from Icarus. When the radar parameters of range, antenna gain, etc., are taken into account, the result is the radar cross section σ. For Icarus,

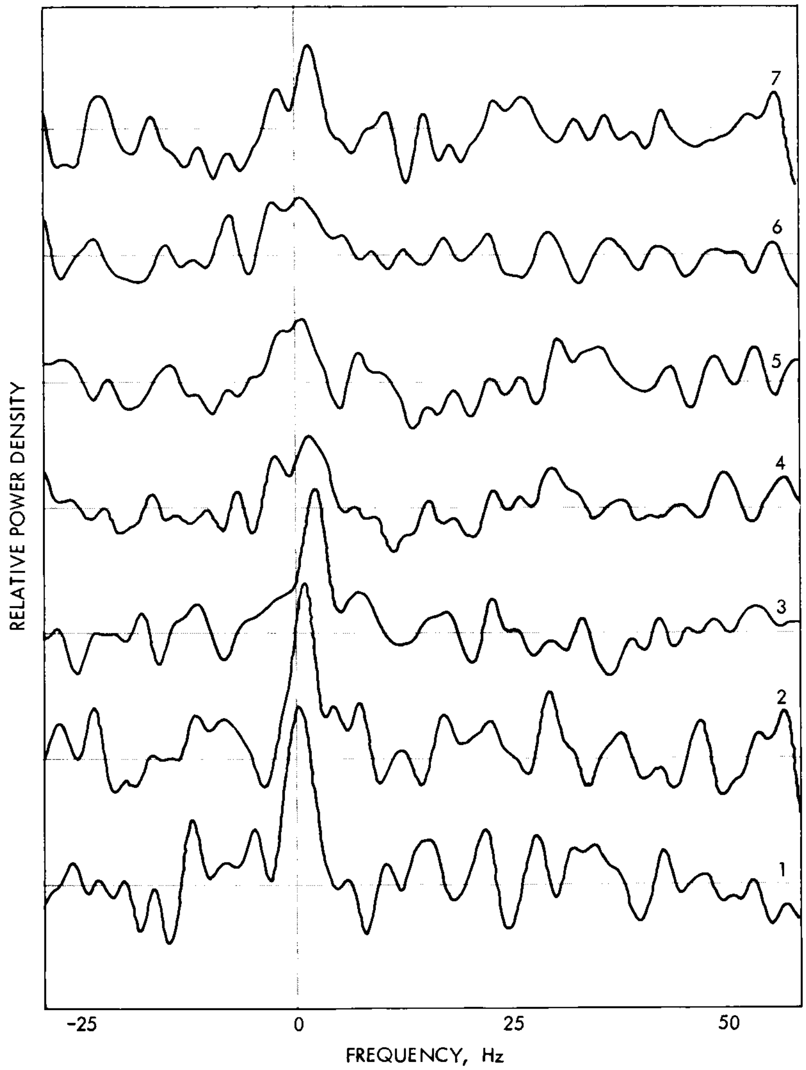

Fig. 1. Individual spectra of Icarus echo

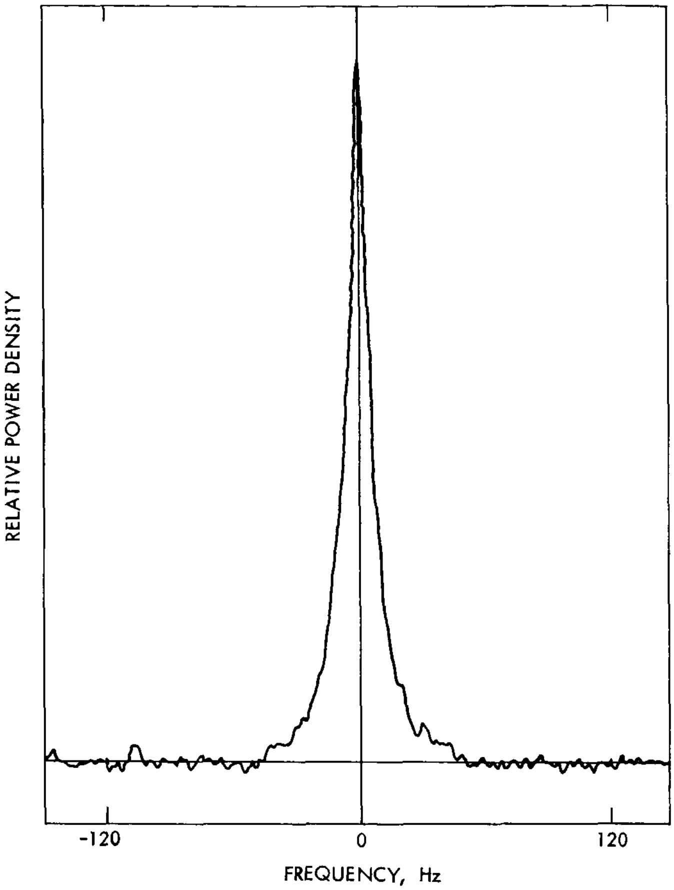

Fig. 2. A sample spectrum of an echo from Mercury, used to calibrate the radar

the result of the experiment is

$$\sigma = 0.1\ \text{km}^2$$

Radar cross section is defined as the effective cross-sectional area of the target. Two factors, reflectivity and directivity, are multiplied onto the actual area. In order to estimate the target radius, it is necessary to assume a reflection model. Radii of Icarus have been computed under the assumption that Icarus reflects in the same way as either Mercury, moon, or Venus. The results are shown in Table 1.

Table 1. Radius and rotation period of Icarus

Reflection model	Radius, km	Rotation period, h
Mercury	0.6	0.7
Venus	0.5	0.5
Moon	0.7	0.9
Rough, metallic	0.3	1.5
Rough, stony	0.6	3.3

The bandwidth B of the spectra at the half power points are related to the spin rate of Icarus by

$$B = \omega r/Q$$

where ω is the effective spin rate, r is the radius, and Q is an unknown shape factor of the spectrum which depends on the roughness of the target. For Mercury, Q equals 7.4.

Once again one has to assume a reflection model in order to compute the spin rate. The rotation period has been estimated for the same models as before, and these results are also listed in Table 1. The effective spin rate is the projection of the actual one, across the line of sight. There is, in addition, a small orbital component of effective spin, but for Icarus this component is negligible.

The 4-h average spectra of Fig. 1 are very noisy and inconclusive. However, a trend does appear in these records. The first two show a single frequency of maximum response, whereas the last four appear bimodal. The third spectrum appears to be transitional. Figure 3 is the result of averaging the last five spectra, so that the bimodal structure shows up clearly. This spectrum has twice the frequency resolution of Fig. 1.

This change cannot be interpreted as the result of Icarus' rotation, since each spectrum is the result of almost 4 h (hence more than one period) of averaging. However, the subradar point on Icarus moved appreciably during the 2½ days of the experiment. Figure 4 shows this motion, with the position at the time of each spectrum marked.

If Icarus is rough, even jagged, and not necessarily round, the spectrum would be expected to change with the motion of the subradar point. In particular, the slow change from unimodal to bimodal can be explained in terms of the motion of the subradar point and the supposed irregular shape of Icarus.

Consequently the radius and spin are computed for two additional models of reflectivity: rough and metallic and rough and stony. The rough assumption leads to a Q factor of $2^{1/2}$. Reasonable reflectivities for metallic and stony surfaces are 0.5 and 0.1, respectively. The corresponding values of the radius and rotation period are listed in Table 1.

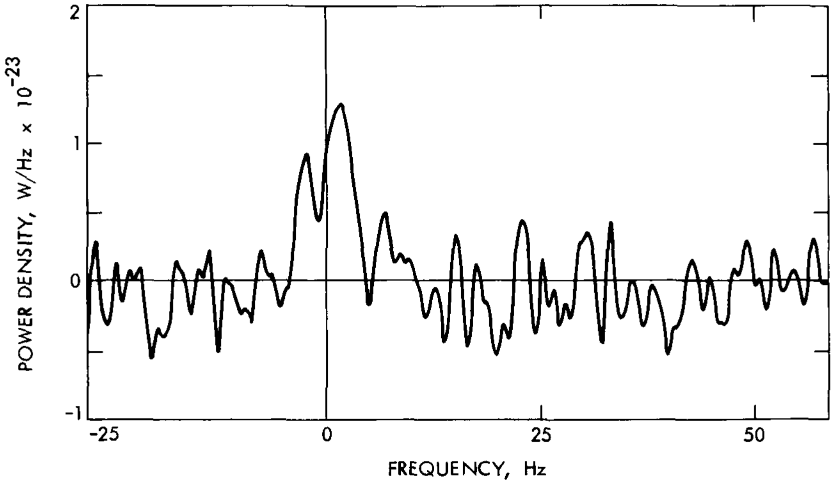

Fig. 3. Icarus 17-h average spectrum

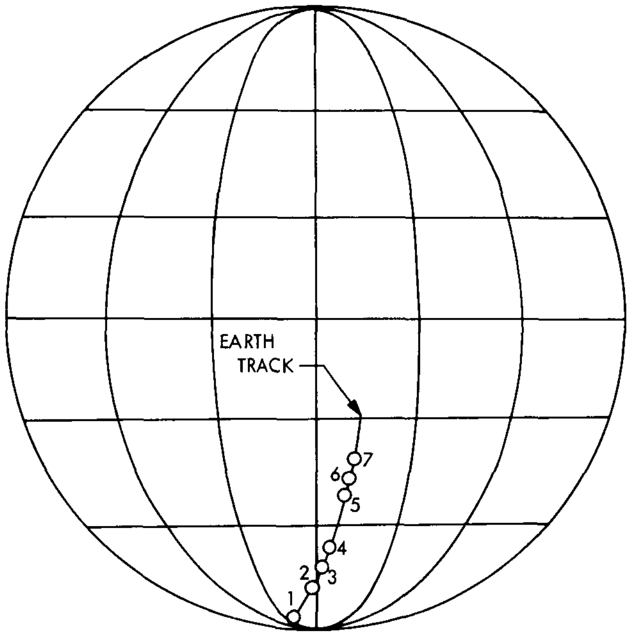

Fig. 4. Position of subradar point on Icarus, assuming no rotation

The center frequency of each spectrum gives the doppler shift and, hence, the line of sight velocity of Icarus. Because of the irregular shape of the spectra, the center frequency is imperfectly determined. We have chosen the "center of gravity" of the spectra as our estimate of the center. The resulting doppler measurements are given in Table 2. This data can be used to improve the ephemeris of Icarus.

Table 2. Doppler measurements of Icarus

Spectrum	Received time		Doppler, Hz
	Day (1968)	h:min	
1	166	05:30	+ 115417.1 ±0.3
2	166	22:20	− 10324.1
3	167	04:30	− 61207.2
4	167	09:40	− 104441.9
5	168	01:40	− 202453.5
6	168	06:30	− 234710.0
7	168	10:00	− 255404.7

B. Simulation of the Programmed Oscillator for Laboratory Testing of Control Programs,

R. F. Emerson

1. Introduction

The Mod V programmed oscillator (PO) is a complex subsystem and its control program is even more complex (SPS 37-39, Vol. III, pp. 71–76). By simulating the programmed oscillator with software, new programs may be tested without tying up an entire tracking station.

2. Method

The simulation program consists of three basic parts: the initialization or setup, the interrupt simulation, and the device simulation routines. The setup routine connects the two programs so that they may operate as one (Fig. 5a). The connection of the two programs is done by replacing the device EOM, EOM-POT, and EOM-PIN

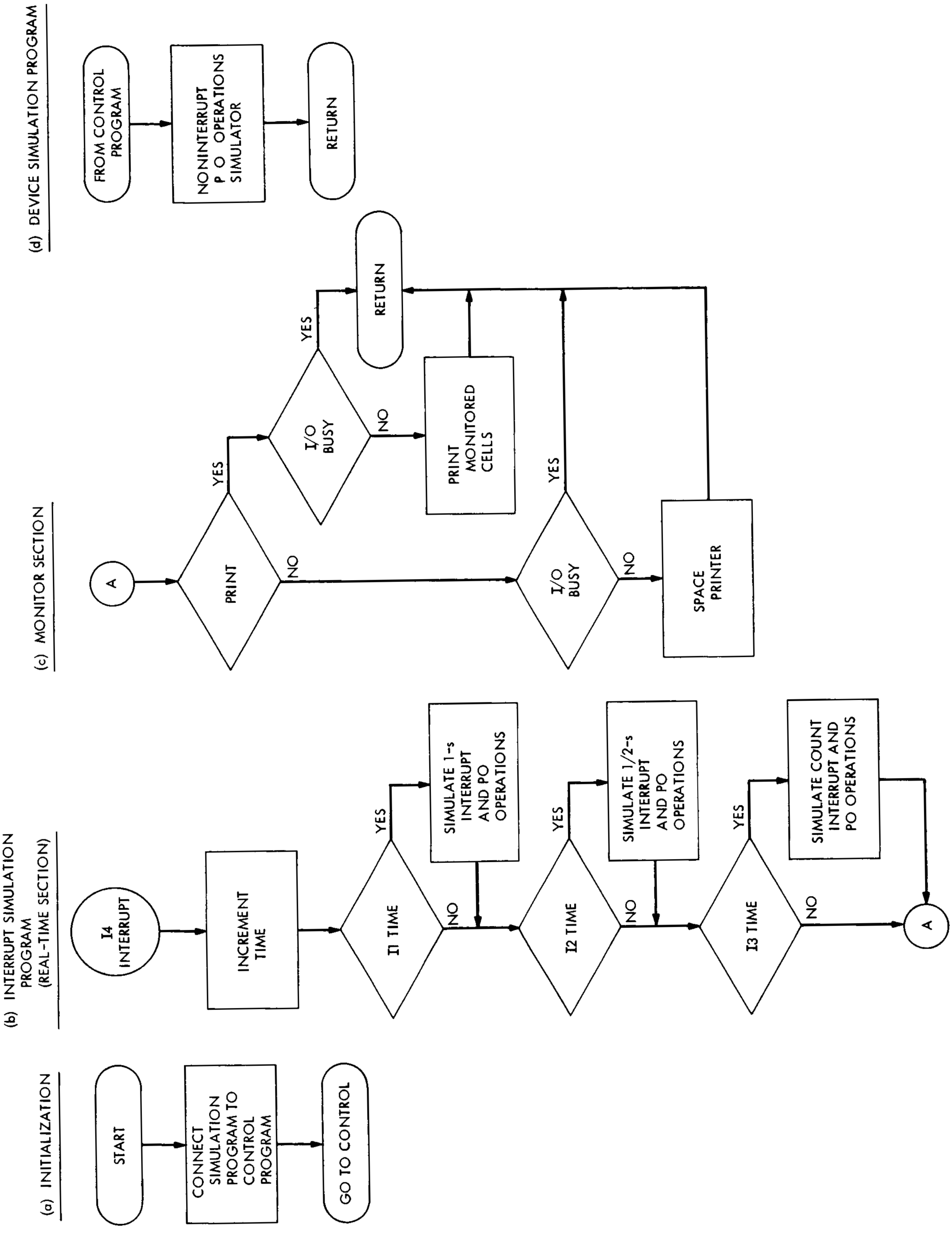

Fig. 5. Flow diagram of simulation program

commands by BRM commands[2] to routines which affect the data transfer between the two programs.

The PO provides three interrupts. The interrupt simulation portion must simulate the action and timing of each of these interrupts. The basic cycle of the PO is a count of ten, that is, the minimum period is one tenth that of the maximum period. All other interrupts can be expressed as integer multiples of the minimum repetition rate.

The primary interrupt routine was thus built around a divide-by-ten program with actions being instituted at appropriate times within the cycle. After performing a simulation of the exterior device, these action routines cause an appropriate interrupt to be generated.

Figure 5b shows the logic of the real-time section of the simulation program. On an I4 interrupt (0204), an external signal used to control the simulation, this routine is entered. The simulator clock is incremented and checked against the time when simulated interrupts are required. When it is time to initiate a simulated real-time interrupt, the appropriate command is sent to the program interrupt card (SPS 37-47, Vol. III, pp. 58–62). Each of the simulated interrupts is of higher priority than the control interrupt and takes over immediately.

An external signal was used to vary the rate of operation. During debugging the rate was set slower than real-time. This allowed the operator to investigate the condition of the composite program completely before going to the next interrupt condition. When it was necessary to verify the operation of the control program the rate was set faster than real-time to reduce the time required to complete a pass or one day of tracking.

The real-time simulation of the device is accomplished by calculating the data that would be provided by the PO. This data is stored in cells accessible by the control program.

The control program responds to the interrupts as it would if the device were actually connected, except when information must be transferred. At these times the control program calls upon the device simulation routines. A typical routine is shown in Fig. 6.

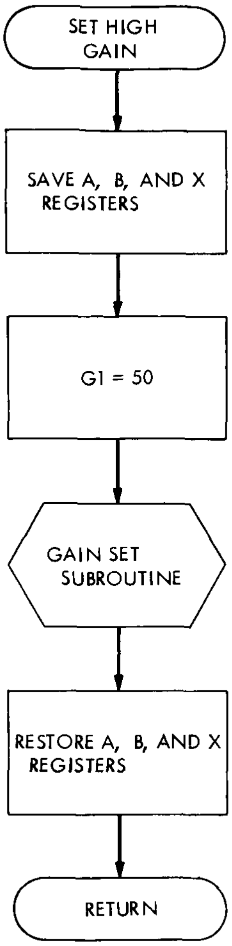

Fig. 6. Flow diagram of a typical device simulation routine

Additional routines are included in the device simulation routine package which are used when requested by the operator through the console control routine. The console control routine is a part of the control program, which enables the operator to control, interrogate, or modify the control program without stopping or delaying its normal operation (SPS 37-39, Vol. III).

The device simulation routines replace the hardware which decodes the commands and presents the requested data to the control program.

It should be noted that the combined control-simulation program spends most of the time in the main loop of the control program. This arrangement allows the composite program to make full use of the console control routine of the control program. The operation of both the control program and the simulation program was monitored by printing on the line printer selected cells of both programs.

---

[2] EOM = end of message; POT = parallel output; PIN = parallel input; BRM = branch and mark place.

The monitor routine was written to print or space the paper every other time it was entered, because this significantly reduced the programming effort and did not reduce the amount of useful data.

3. Operation

When the simulation program is loaded with the control program it is entered first and establishes the necessary communication between the two programs. This requires the replacement of some commands and data words in the control program (Fig. 5a).

The timing control is provided by an external pulse generator. The external signal is used to interrupt the computer into the real-time section of the simulation program (Fig. 5b).

As described above, the real-time section has a clock cell which is used to control the actions of the simulation program. This cell is incremented for each external interrupt signal. At appropriate times in this major cycle, segments of the operation of the PO are simulated, and the results are stored in cells accessible to both the control and simulation programs. A simulated interrupt (or internal interrupt) is produced for that part of the equipment under simulation at the time. Since the device interrupts are of higher priority than the external control interrupt, the operation is transferred to the corresponding active interrupt response routine in the control program. After servicing the interrupt, control is returned to the real-time section where similar decisions are made for each simulated segment of the controlled device.

When all of the above simulations are completed, the monitoring section is entered (Fig. 5c). If the input/output (I/O) channel is not busy, and the printer is ready, a command will be given either to print the monitored cells or to space the printer, and control is returned to the next location to be executed in the main loop.

During the operation of the control program, the control program may change the configuration of the simulated device. These conditions are communicated to simulation program through the routines in the device simulation section (Fig. 5d). Connections to these routines are made during the initialization phase.

4. Application

After the simulation program was debugged, it was applied to an expanded version of the programmed oscillator control program now in use at the Mars DSS. The external control signal was adjusted to provide a simulation time varying from one-tenth to ten times real-time. With this configuration the control program was debugged in less than 5 days. During this debugging several problems were discovered in the control program which may not have occurred in the field for several years. Thus it was possible to locate and correct faults which had an extremely low probability of occurrence.

A word of caution, however, is that this was an ideal simulation. It did not allow for equipment drift nor for component noise. The inclusion of these parameters, while possible, was not justified, because such fluctuations tend to be small compared to the gross operation of the equipment and the time required to program for these contingencies would have been excessive.

5. Conclusion

This simulation permitted the rapid and easy checking of the control program. This PO control program was more completely checked than could have been done with the PO hardware. The simulation concept was proved feasible and shown to be easily modified to test for unusual and unpredicted conditions. This technique is a powerful tool for the testing of computer-controlled systems.

C. Symbol Synchronizer for Low Signal-to-Noise Ratio Coded Systems, *T. O. Anderson and W. J. Hurd*

1. Introduction

This article describes a general-purpose symbol synchronizer and data detector that operates with negligible degradation at the low symbol signal-to-noise ratios (SNRs) which occur in coded systems. The synchronizer will first be used with the sequential decoding machine described by Lushbaugh and Layland (SPS 37-50, Vol. II, pp. 71–78), which will operate over a wide range of information rates at symbol SNRs as low as −4 to −5 dB. The synchronizer will operate at these low SNRs at symbol rates of from 6.25 bits/s to 250 kbits/s.

2. Design and Performance Parameters

For any fixed symbol SNR, the synchronizer will have the same relative parameters at all symbol rates from 6.25 bits/s to 250 kbits/s. Six relative loop bandwidths in two ranges of three each may be selected by a front panel switch. At the design point of $ST_S/N_0 = -3$ dB, where S is the signal power, T_S is the symbol duration, and N_0 is the one-sided noise spectral density, the bandwidths are $w_L\ T_S = 0.0019$, 0.00047, and 0.00012 in the wide range, and 0.0002, 0.00005, and 0.0000125 in the narrow range. The damping ratio $\zeta = 0.790$ in the wide range and 0.707 in the narrow range. At $ST_S/N_0 = -3$ dB, these loop bandwidths yield loop SNRs of from 12.0 to 33.8 dB and rms phase errors of from 0.25 to 0.020 rad.

It is not known exactly how much these phase errors and phase noise bandwidths will degrade the performance of coded systems, because the phase noise is not independent from symbol to symbol. This may be especially true of systems which use several levels of quantization of the detected symbols rather than making hard decisions on each symbol. The sequential decoding machine uses such a quantizing system. However, if an average symbol SNR is used as the criterion, the degradation is less than 0.1 dB at the narrowest loop bandwidth. See, for example, SPS 37-48, Vol. II, pp. 125–128. This degradation would be less at higher SNRs.

3. Design Description

a. Functional design. For the present discussion, reference is made to the functional block diagram of Fig. 7.

The basic concepts used in the design of the synchronizer phase-locked loop are well known. The phase detector consists of several integrators and the logic necessary to obtain phase-error estimates from their quantized outputs. Integration is performed in two channels: (1) between transition points in the data channel, and (2) across transition points in the phase channel. The input to both channels is the received signal, which consists of a constant amplitude bipolar video data stream plus white gaussian noise. In the data channel, the integrations are performed over the assumed data symbol positions, from $(n-1)T_S$ to nT_S, so that the signs of the integrals represent estimates of the binary data symbols. In the phase channel, the integration windows are symmetric about times nT_S. If there is no noise and no timing error, and if a data transition occurs at time nT_S, then the integral across this transition is zero. If there is a timing error between the local clock and the actual data timing, then the integral across the transition is proportional to this timing error. When noise is present, the expected value of the phase channel integral is proportional to the phase error. If no transition occurs, the phase channel integral contains no timing information. For simplicity, only the sign of the phase channel integral is used, so that the phase detector output is $+1$ if the estimate of phase error is positive, -1 if the estimate is negative, and zero if no estimate can be made because no transition is detected. This hard limiting of the phase detector output considerably simplifies implementation of the loop filter while causing a degradation of less than 2 dB in loop SNR.

Integration in both channels is performed using operational amplifier integrate and reset modules. Two modules are used in each channel so that one is being reset while the other is integrating. In the data channel, the output of each integrator is converted to digital form using two separate A/DCs. Demultiplexing is accomplished digitally, eliminating the need for analog switches. The A/DCs are not required for the synchronizer itself, as only the sign of each integral is used, but are included because the sequential decoder system which will use this synchronizer requires 3-bit quantization of the data symbols. In the phase channel, two Schmitt triggers are used instead of A/DCs, since only the signs of the integrals are required, and again the multiplexing is done digitally.

The phase detector output forms the input to the loop filter which is implemented digitally as a perfect integrator. The loop filter transfer function $F(s)$ assumes the form

$$F(s) = \underset{\text{component)}}{K_1 \text{ (first-order}} + \frac{K_2}{sT_S} \underset{\text{component)}}{\text{(second-order}} \tag{1}$$

The two components of the loop filter output are generated separately in the digital domain, and then converted to analog voltages and summed in an operational amplifier. The first-order component of the filter output is generated by setting a register to $+K$, $-K$, or 0, according to whether the phase detector output is $+1$, -1, or 0, and then converting to an analog voltage. The second-order component is the running sum of the phase detector outputs. This summation is accomplished by an up–down counter. The constant T_S arises because inputs to the filter occur every T_S sec, and the gain K_2 is controlled by varying the number of stages in the up–down counter.

The loop bandwidth is controlled by varying the two gains of the digital filter. Initial acquisition of symbol sync may be achieved by increasing the gains K_1 and K_2, thus widening the loop bandwidth, and selecting the voltage-controlled oscillator (VCO) frequency such that the frequency error between the symbol rate and the VCO frequency is less than the loop bandwidth. When symbol lock is achieved, the loop bandwidth is narrowed to give better tracking performance.

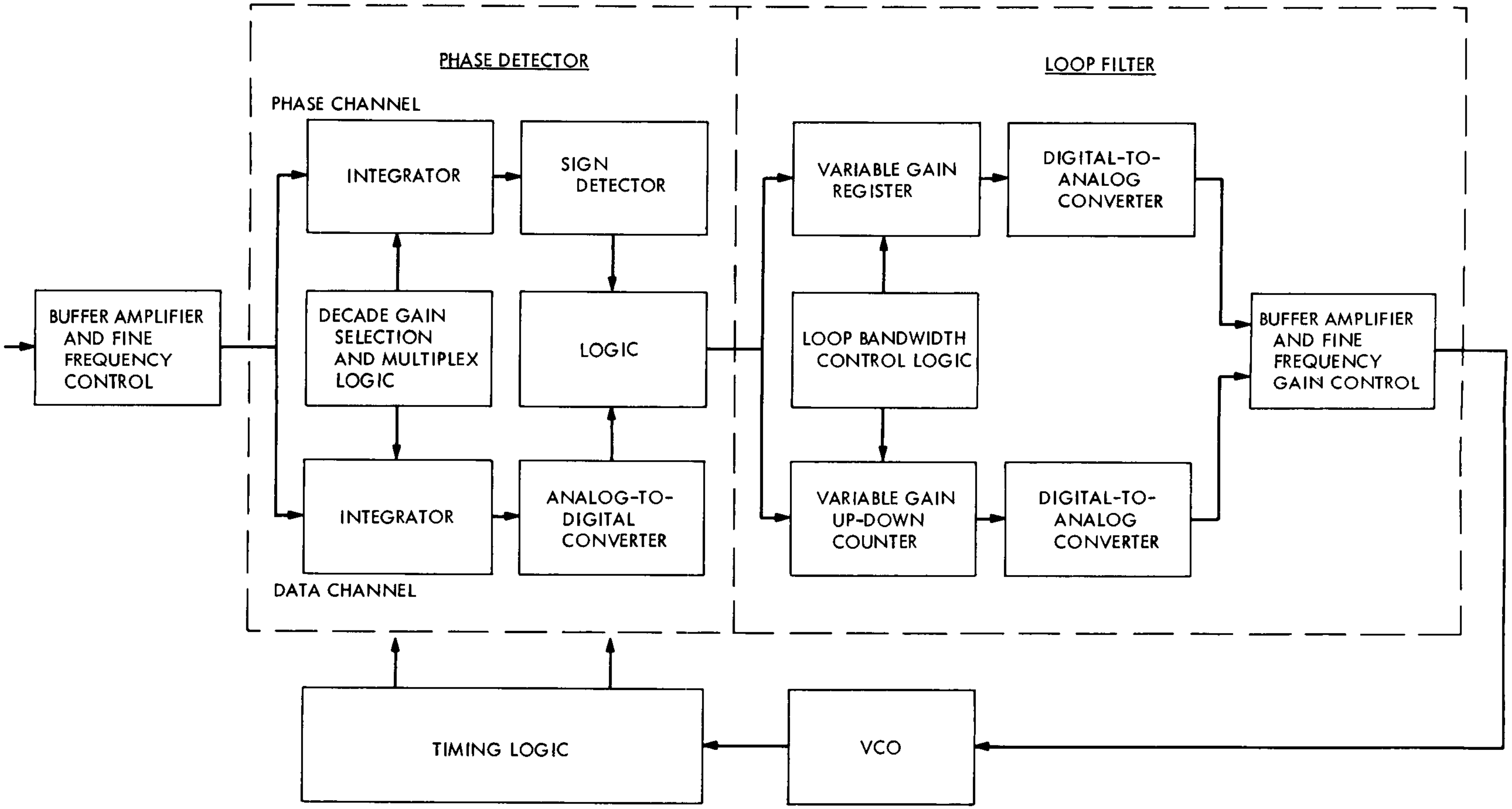

Fig. 7. Symbol synchronizer block diagram

b. Integrators. Even though this symbol synchronizer is designed to work at data rates as high as 250,000 symbols/s, the integrators used are conventional analog integrate and reset circuits. However, even with the fastest available analog integrate and reset circuits, two integrators must be used in each channel so that one integrates while the other is reset. Otherwise the reset time would cause significant loss of data at high data rates. To avoid switching noise in the analog signal, and to allow greater timing flexibility, the demultiplexing is performed not in the analog domain but in the digital domain after conversion. This means that the integrate and reset circuits are continuously connected to the signal and to their individual A/DCs or Schmitt triggers. The integrate and reset modules used in both channels are Burr–Brown model 4013/25, with 0.001-μF feedback capacitors for high data rates and 0.05μF for low data rates. The reset switch is rated at 20 mA, so that the maximum 10-V charge can be dumped from the 0.001-μF capacitor in 0.5 μs. About 3 μs is required, however, before the module stabilizes to within 10 mV of ground. This is sufficient to assure complete resetting even at the maximum data rate, when $T_S = 4.0$ μs.

c. Analog-to-digital converters. To satisfy the speed requirements of the A/DCs, high-speed tracking converters are used instead of the normal A/DC method of sample and hold circuits followed by successive approximation-type converters. In the HSTCs, the signal is continuously tracked and converted to digital form. Then, upon a *stop convert* command, the digital value is frozen. Five-bit converters are used, with an aperture time of 400 ns.

d. System timing. To provide flexibility in detailed timing selection, the basic clock frequency is selected to be 16 times the symbol rate. The basic clock is applied to a four-stage countdown counter and decoder whose various outputs provide the detailed timing for the integrators, A/DCs, copy registers, and the digital loop filter components. The timing chart (Fig. 8) shows the timing for both the data and phase channel integrators. It may be noticed that the outputs of the two data channel integrators are held in the output registers for 2-bit periods. Thus the latest two samples from the data channel are available simultaneously for a full symbol time during which the desired operations may be completed. The two branches of the phase channel operate similarly to the branches of the data channel, except that the integration time is a ½-bit time, and the reset time is 1½ bit times. The output data remains in the output register for 1 bit time. Use of the shortened phase channel integration time results in a 3-dB increase in the loop SNR for any input SNR.

e. Control logic. The control logic for the phase detector contains delay circuits so that two data channel samples and the phase channel sample for the integral between these two data samples are all made available simultaneously. Transitions are detected by an *exclusive or* circuit between the two data channel samples. The sign of the phase channel error signal is multiplied by the sign of one of the data channel samples to account for the direction of the transition by a second *exclusive or* circuit.

4. Phase Detector Analysis and Simulation

The parameters and performance of the phase-locked loop depend on the gain of the phase detector and on the noise spectral density at the phase detector output. Of primary importance is the value of the expression

$$\frac{A^2}{S(0)/T_S} \qquad (2)$$

which, when multiplied by the relative loop bandwidth yields the loop SNR. In this expression, A is the phase detector gain, and $S(0)$ is the noise spectral density at zero frequency when the phase error is zero.

In this section, A and $S(0)$ are determined as functions of symbol SNR for the phase detectors under consideration. They are first calculated using a simplified analysis of the phase detectors, and then the validity of the approximations are confirmed by Monte Carlo simulation. The simulation also yields the S-curves, or phase input versus mean phase output relationships, for the various phase detectors.

a. Simplified analysis. For a linear loop analysis, the phase detector gain A is defined as the slope of the input–output characteristic at zero phase error. If ϕ is the input phase error, and $\hat{\phi}$ is the output phase error estimate, then

$$A = \frac{\partial}{\partial \phi} E\,\{\hat{\phi}(\phi,R)\} \qquad (3)$$

where the expectation is required because $\hat{\phi}$ is a random process, and where the argument R is the symbol SNR $= ST_S/N_0$.

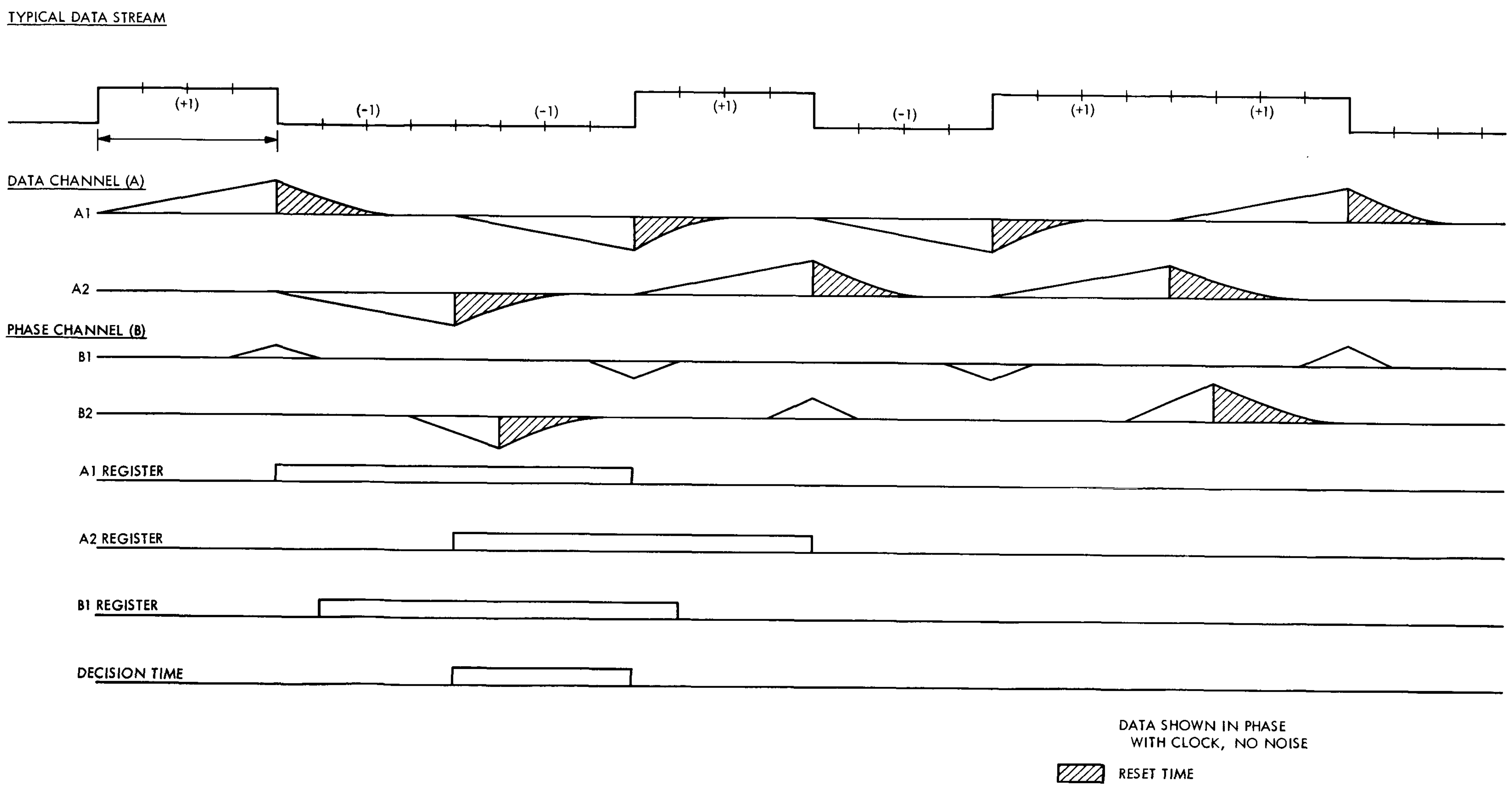

Fig. 8. Timing chart

Page intentionally left blank

Suppose the locally generated clock is such that the data channel integration windows are from times $(n-1)T_S$ to nT_S, and the actual input data symbols are present from $(n-1)T_S + \tau$ to $nT_S + \tau$. The phase error is then $\phi = 2\pi\tau/T_S$. When a symbol transition occurs, the phase channel integrator output is

$$Z_n = \pm 2\tau S^{1/2} + \int_{(n+W/2)T_S}^{(n-W/2)T_S} n(t)\,dt \tag{4}$$

where $n(t)$ is the input noise, assumed to be zero mean, white, and gaussian, and W is the fractional window width. $|\tau|$ is assumed to be less than $W/2$. The sign is positive or negative according to whether the transition is negative or positive, respectively, and Z_n is conditionally gaussian with variance $N_0WT_S/2$ and conditional mean $\pm 2\tau S^{1/2}$. Z_n is not used if no transition is detected. Suppose now that there is no noise, so that all transitions are detected correctly. In the no-quantization case, we form the phase estimate $\hat{\phi}_n$ by multiplying A_n by $\pm 2\pi/(S^{1/2}T_S)$ if a transition occurs, or 0 otherwise. The mean output is

$$\mathrm{E}\{\hat{\phi}_n\} = \frac{1}{2}\,\frac{2\tau S^{1/2}2\pi}{S^{1/2}T_S} = \phi \tag{5}$$

so that $A = 1.0$. In the hard limiter case, we use only the sign of Z_n, so that the average output is 0.5 sgn (ϕ), and A is infinite. This occurs only when there is no noise.

In the noisy case, there is no contribution to the phase estimate if we do not detect a transition, and on the average, there is no contribution if we detect a transition when none has occurred. If a transition occurs and $\phi \approx 0$, we detect its direction correctly with probability $(1 - P_E)^2$ and incorrectly with probability P_E^2, where P_E is the symbol error probability, and

$$P_E(R) = 0.5\,(1 - \mathrm{erf}\,(R^{1/2})) \tag{6}$$

where

$$\mathrm{erf}(x) = 2\pi^{-1/2}\int_0^x e^{-t^2}\,dt \tag{7}$$

is the error function. If we detect the direction of transition incorrectly, we use the negative of the desired estimate of ϕ. Therefore, neglecting the interdependence of the data and phase channel integrals and assuming P_E to be constant with respect to ϕ

$$A \approx [(1-P_E)^2 - P_E^2]\,\frac{\partial E\,\{\hat{\phi}_n\}}{\partial\phi} \tag{8}$$

$$\approx 1 - 2\,P_E(R) = \mathrm{erf}\,(R^{1/2}) \tag{9}$$

since $\mathrm{E}\{\hat{\phi}_n\} = \phi$, independently of R. Thus one effect of noise in the no-quantization case is to lower the phase detector gain.

The noise spectral density at zero frequency for $\phi = 0$ is given by

$$\frac{S(0)}{T_S} = C(0) + 2C(T_S) \tag{10}$$

where $C(\cdot)$ is the noise correlation function, assuming $\phi = 0$. This follows because the phase estimate at time nT_S is uncorrelated with the estimate at time mT_S for $|n\text{-}m| > 1$. We now make the further simplifying assumption that $|C(T_S)| \ll C(0)$, so that

$$\frac{S(0)}{T_S} \approx C(0) \tag{11}$$

This greatly simplifies the analysis, and the simulation results justify this assumption. Then

$$\begin{aligned}\frac{S(0)}{T_S} \approx C(0) &= \frac{(2\pi)^2}{ST_S^2}\,\mathrm{E}\,\{\hat{\phi}_n^2\}\\ &= \frac{1}{2}\,\frac{(2\pi)^2}{ST_S^2}\,\frac{N_0WT_S}{2}\end{aligned} \tag{12}$$

since, for $\phi = 0$, $\hat{\phi}_n$ is zero with probability 0.5 and is gaussian with variance $N_0WT_S/2$ with probability 0.5, Thus, using $R = ST_S/N_0$,

$$\frac{S(0)}{T_S} \approx \pi^2 W/R \tag{13}$$

In the hard-limiter case, when transitions occur and are detected, the phase estimate is

$$\pm\mathrm{sgn}\left[2\tau S^{1/2} + \int_{(n-W/2)T_S}^{(n+W/2)T_S} n(t)\,dt\right] \tag{14}$$

where the sign is positive or negative according to whether or not the transition is detected correctly. Hence

$$\mathrm{E}\{\hat{\phi}_n\} \approx \frac{1}{2}\,(1 - 2P_E)\,\mathrm{E}\,\{\mathrm{sgn}\,(2\tau S^{1/2} + y_n)\} \tag{15}$$

where y_n is a zero mean gaussian random variable with variance $N_0WT_S/2$.

Therefore, letting $p(y_n)$ be the probability density of y_n,

$$E\{\hat{\phi}_n\} \approx \frac{1}{2}(1 - 2P_E)\left[\int_{-2T_S^{1/2}}^{\infty} p(y_n)dy_n - \int_{-\infty}^{-2T_S^{1/2}} p(y_n)dy_n\right]$$

$$\approx \frac{1}{2}\,\mathrm{erf}(R^{1/2})\,\mathrm{erf}\left(\frac{\phi R^{1/2}}{\pi W^{1/2}}\right) \qquad (16)$$

and the phase detector gain is

$$A = \frac{d}{d\phi}\,E\{\hat{\phi}_n\}\Big|_{\phi=0}$$

$$\approx \frac{R^{1/2}}{\pi^{3/2}W^{1/2}}\,\mathrm{erf}\,(R^{1/2}) \qquad (17)$$

The spectral density $S(0)/T_S \approx C(0)$ is approximately 0.5 in the hard-limited case, since the estimate is ±1 half of the time and zero otherwise.

b. Analysis results. Table 3 shows the results of the simplified phase detector analysis for symbol SNRs of $R = -3$, 0, and 10 dB. In all cases, the SNR A^2T_S/N_0 is 3 dB better for the half-width window, $W = 0.5$, than for the full-width window, $W = 1.0$. The degradation when the limiter is used (1-bit quantization) relative to no quantization is $\pi/2$, or 1.96 dB, at all SNRs.

c. Phase detector simulation. Digital Monte Carlo simulation was used to determine the input–output characteristics (S-curves) and the output noise spectral densities S(0) for the various phase detectors. Figure 9 shows the S-curves for the phase detectors with no quantization, and Fig. 10 shows the S-curves with 1-bit quantization. In generating these curves, 50,000 symbols were used for $R = -3$ and 0 dB, and 20,000 symbols for $R = 10$ dB, except that 500,000 and 200,000 symbols were used at $\phi = 0.1\pi$ for $R = -3$ and 0 dB, respectively. The maximum standard deviation of the estimate of any point on the S-curves was thus about 3% of the estimate.

The phase detector gains and output noise spectral densities as determined from the simulation are given in Table 4. The gains were calculated from the points on the S-curves at $\phi = \pi/10$. Thus the gains are generally slightly lower than predicted by the analysis, because of the concave shape of the curves. The remaining discrepancies are attributed to the inaccuracies of the analysis, due to the independence assumptions.

The experimental spectral densities are slightly lower than predicted in the no quantization cases, and slightly higher in the 1-bit quantization cases. One reason the experimental values of S(0) do not agree exactly with the calculated values is that the calculated values use $S(0)/T_S \approx C(0)$ rather than $S(0)/T_S = C(0) + 2C(T_S)$. The last column in Table 4 gives the measured values of $C(0)$, so that one can see the effect of neglecting $C(T_S)$ by comparing $C(0)$ with $S(0)/T_S$. The remaining differences between the measured and calculated values of S(0) are due to the assumption of independence between the data and phase channel integrators.

The S-curves are also used in comparison of the phase detectors. For the no-quantization cases, Fig. 9, the input

Table 3. Comparison of phase detectors according to simplified analysis

R, dB	W	Quantization	A, units/rad	S(0)/T_s, units²	A²T_s/S(0), dB/rad
−3.0	0.5	none	0.682	9.86	−13.26
↓	1.0	none	0.682	19.70	−16.26
	0.5	1 bit	0.1225	0.5	−15.22
	1.0	1 bit	0.0865	0.5	−18.22
0.0	0.5	none	0.843	4.93	− 8.41
↓	1.0	none	0.843	9.86	−11.41
	0.5	1 bit	0.214	0.5	−10.37
	1.0	1 bit	0.151	0.5	−13.37
10.0	0.5	none	1.0	0.493	3.08
↓	1.0	none	1.0	0.986	0.08
	0.05	1 bit	0.802	0.5	1.12
	1.0	1 bit	0.567	0.5	− 1.88

Table 4. Phase detector characteristics according to simulation

R, dB	W	Quantization	A, units/rad	S(0)/T_s, units²	C(0), units²
−3.0	0.5	none	0.585	9.47	9.02
↓	1.0	none	0.535	17.81	16.07
	0.5	1 bit	0.108	0.512	0.501
	1.0	1 bit	0.076	0.531	0.499
0.0	0.5	none	0.745	4.91	4.71
↓	1.0	none	0.684	9.61	8.98
	0.5	1 bit	0.193	0.512	0.501
	1.0	1 bit	0.125	0.521	0.500
10.0	0.5	none	1.01	0.503	0.502
↓	1.0	none	1.02	1.006	1.003
	0.5	1 bit	0.759	0.499	0.500
	1.0	1 bit	0.555	0.499	0.500

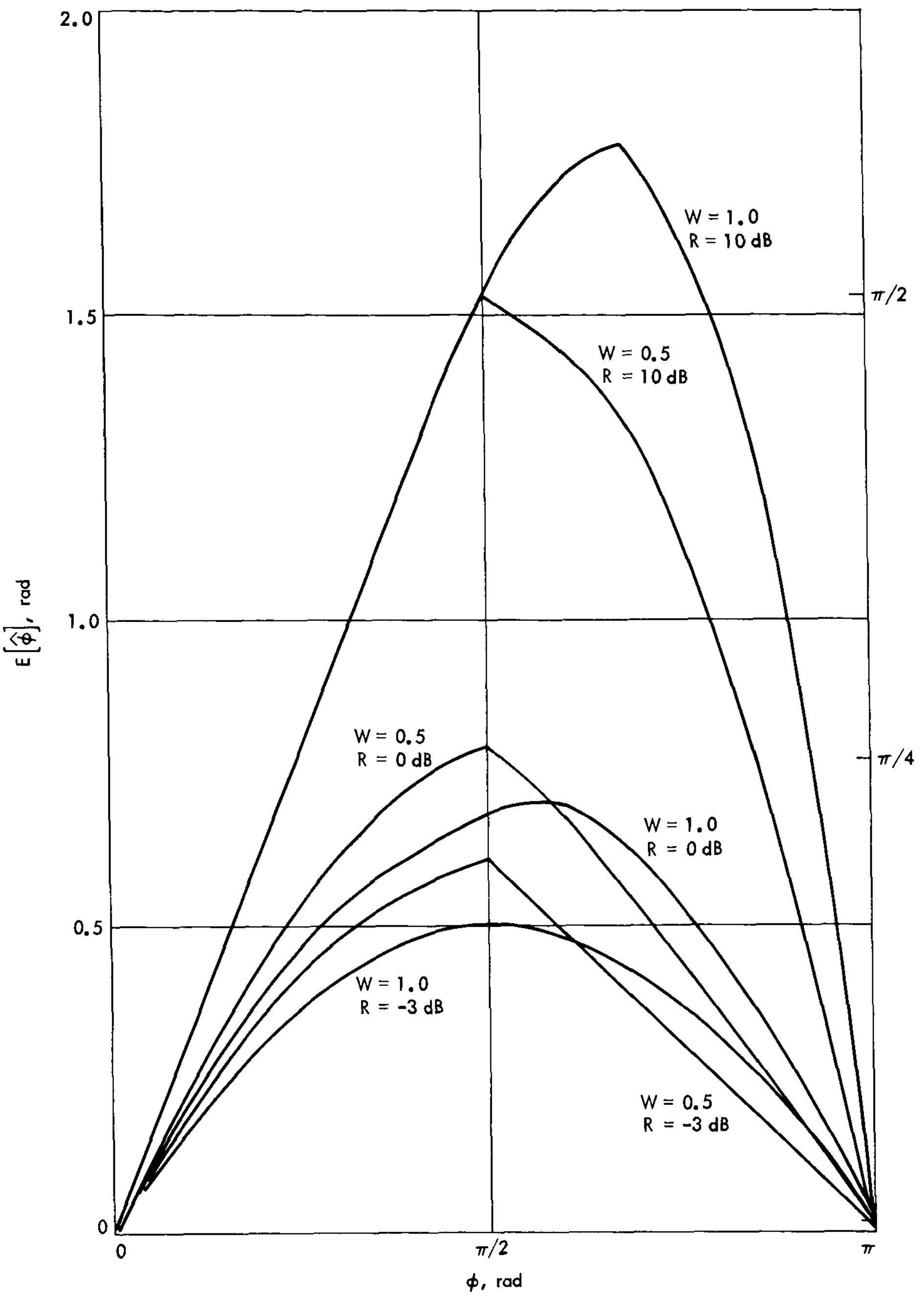

Fig. 9. Phase detector S-curves, no quantization

signal amplitude has been normalized to a constant value, as indicated by Eq. (5). In practice, this is accomplished by using the carrier for the automatic gain control reference. With this normalization, $A \approx \text{erf}(R^{1/2})$. S(0), Eq. (13), decreases with increasing R, and is 3 dB higher for $W = 1.0$ than for $W = 0.5$ for any given R. Since there is little difference between the S-curves for the two different windows, especially at low SNRs, the half-width window is judged to be better on the basis of the lower noise output.

For the 1-bit quantization cases (Fig. 10) performance comparisons can be made directly from the S-curves because the spectral densities S(0) are approximately 0.5 for all cases, regardless of the input signal amplitude. It is now obvious that the half-width window is better

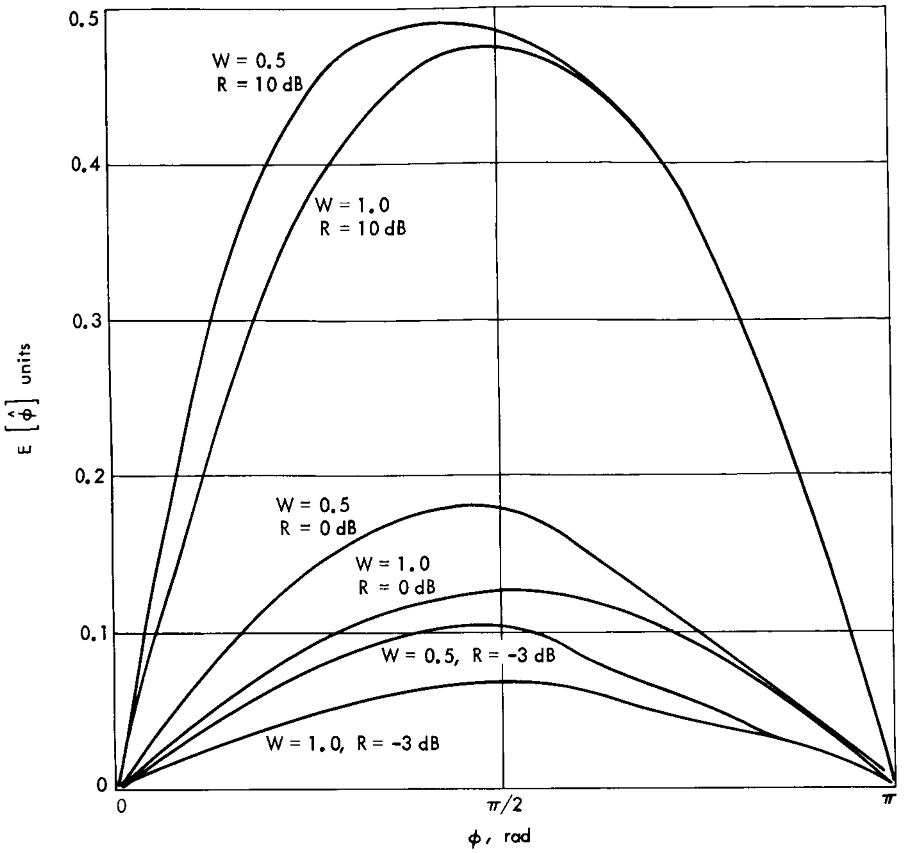

Fig. 10. Phase detector S-curves with 1-bit quantization

for all SNRs, since the half-width window S-curves fall above the full-width window curves at all points.

The S-curves and Eqs. (9) and (17) also indicate the effects of quantization on the variation of phase detector gain with SNR. This is discussed in the following subsection 5.

5. Phase-Locked Loop Analysis

The symbol tracking loop was analyzed using the results and, where possible, the notation of Tausworthe (Ref. 1). The linearized model for the loop is shown in Fig. 11. We define:

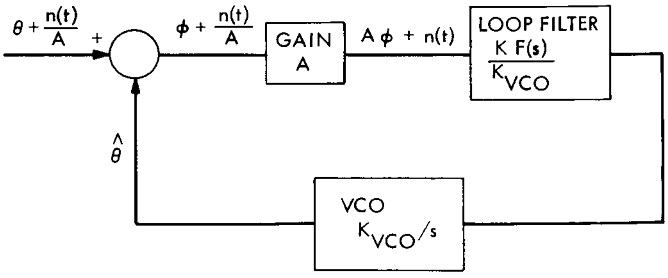

Fig. 11. Linearized model for symbol tracking loop

θ = input signal phase

$\hat{\theta}$ = phase estimate

ϕ = phase error

$n(t)$ = noise at phase detector output

A = phase detector gain

AK = loop gain

K_{VCO} = VCO gain

$KF(s)$ = open loop transfer function

ζ = damping ratio of loop

The loop filter consists of a direct path from the phase detector to the VCO through a digital-to-analog converter (D/AC) and operational amplifiers with a gain of K_1 V/rad, and an integrator path through the up–down counter, a D/AC, and the amplifiers, with a gain of

$K_2/(T_S s)$ V/rad. The gain in the integrator path is proportional to $1/T_S$ because the up–down counter is updated each symbol time.

In Tausworthe's notation, the open-loop transfer function of a perfect second-order loop is

$$KF(s) = \frac{K(1+\tau_2 s)}{\tau_1 s} \tag{18}$$

and our transfer function is

$$\frac{K}{K_{VCO}} F(s) = K_1 + \frac{K_2}{T_S s} \tag{19}$$

Again in Tausworthe's notation

$$\zeta \approx \frac{r^{1/2}}{2} \tag{20}$$

so $\zeta = 0.707$ requires

$$r = \frac{AK\tau_2^2}{\tau_1} = \frac{AK_1^2 T_S K_{VCO}}{K_2} = 2 \tag{21}$$

and the loop bandwidth is

$$w_L = \frac{r+1}{2\tau_2} = \frac{3}{2\tau_2} \tag{22}$$

or

$$w_L T_S = \frac{r+1}{2}\,\frac{K_2}{K_1} \tag{23}$$

Solving these equations for K_1 and K_2, we get

$$K_1 = \frac{4 w_L T_S}{3A\,K_{VCO}\,T_S} \tag{24}$$

and

$$K_2 = \frac{2}{3} K_1 w_L T_S \tag{25}$$

The values of A and w_L to be used in the last two equations are the values at the design point of the system. The values of K_1 and K_2 then, in turn, determine τ_2 by Eq. (22) and determine w_L and ζ as a function of SNR, since A is a function of SNR.

From these equations, it is seen that for a given relative loop bandwidth $w_L T_S$, as selected by the front panel bandwidth switch, both K_1 and K_2 must be varied in inverse proportion to T_S. This is accomplished by the front panel fine-frequency switch, which varies the gain of the summing amplifier between the D/ACs and the VCO input. Coarse adjustment is accomplished by the VCO, whose gain varies in decade steps as the VCO center frequency changes decades.

To control loop bandwidth within each range of loop bandwidths, K_1 is varied in direct proportion to $w_L T_S$ by varying the digital register at the input to the direct channel D/AC, and K_2 is varied proportionally to $(w_L T_S)^2$ by changing the number of stages in the up–down counter. To change from the narrow range of bandwidths to the wide range, the VCO gain is increased by a factor of 10, and the up–down counter gain is increased by 8 by cutting out three stages. This effectively increases K_1 by 10 and K_2 by 80, or slightly less than the 100 desired.

a. Design parameters. The system parameters were selected so that at the design point of $R = -3$ dB, the relative loop bandwidth is approximately as indicated on the front panel, and the damping ratio is about $\zeta = 0.707$. Because of equipment limitations, these values were not attained exactly in the wide-loop bandwidth range. The actual values at $R = -3$ dB are given in Table 5 together with the resulting loop SNRs, rms phase errors, and symbol signal-to-noise degradations.

Table 5. PLL Parameters at design point, $R = -3$ dB

Range	$w_L T_S$ (nominal)	ζ	$w_L T_S$ (actual)	Loop SNR, dB	Rms phase error, rad	Symbol SNR degradation, dB
Wide	0.002 0.0005 0.000125	0.79 0.79 0.79	0.0019 0.00047 0.00012	12.0 18.0 24.0	0.25 0.126 0.063	1.15 0.58 0.29
Narrow	0.0002 0.00005 0.0000125	0.707 0.707 0.707	0.0002 0.00005 0.0000125	21.8 27.8 33.8	0.082 0.041 0.020	0.38 0.19 0.095

b. Variation of parameters with R. Because the phase detector gain varies with symbol SNR, so do the loop bandwidth, the damping ratio, and the doop SNR. Relative to the design point of $R = -3$ dB, ζ varies as the square root of $A(R)$, w_L varies as

$$\frac{w_L(R)}{w_L(R=-3\,\text{db})} = \frac{2\zeta^2(R)+1}{2\zeta^2(R=-3\,\text{dB})+1} \tag{26}$$

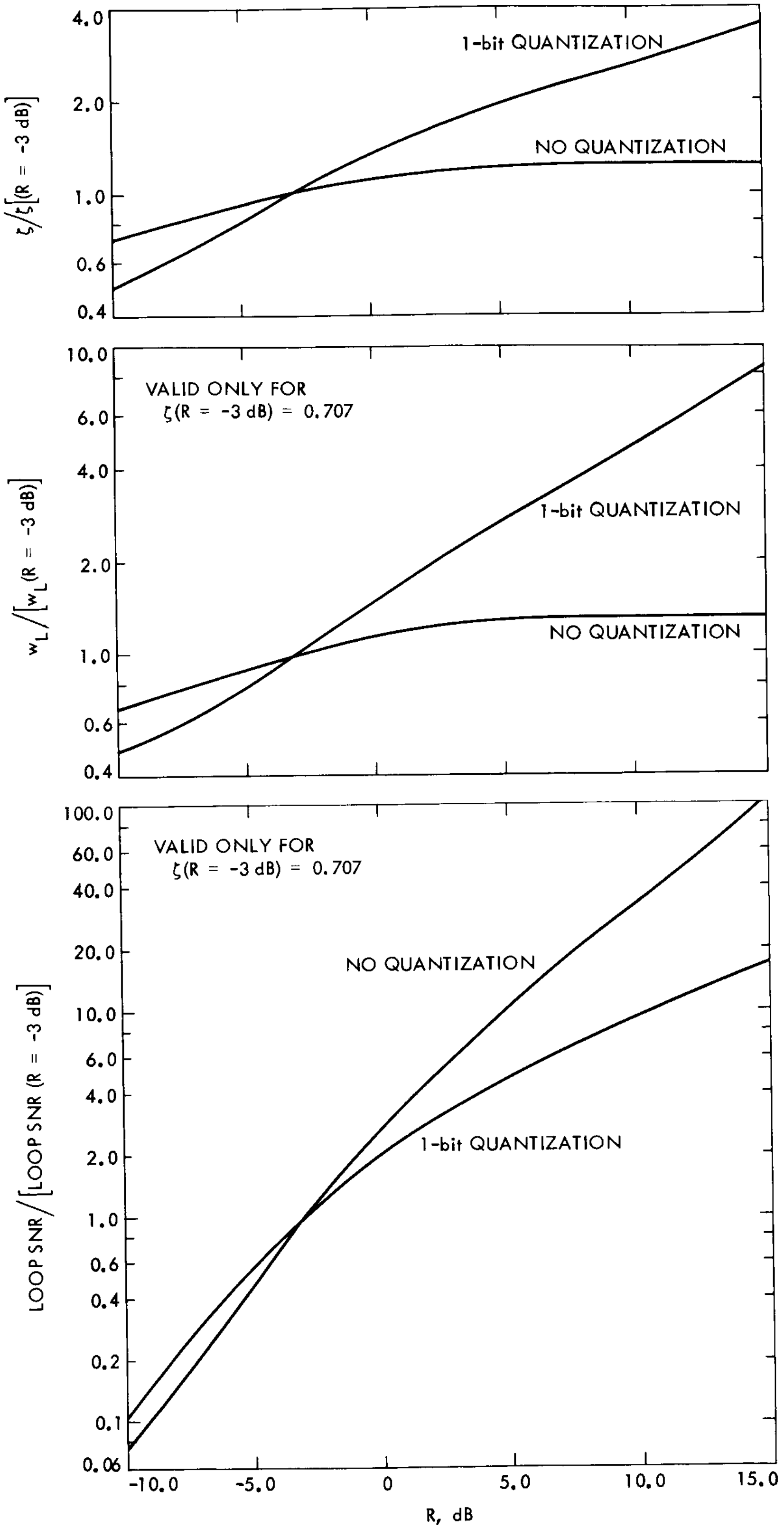

Fig. 12. Variation in PLL parameters

and the loop SNR varies as

$$\frac{\text{loop SNR}(R)}{\text{loop SNR}(R = -3\ \text{dB})} = \frac{A^2(R)}{A^2(R = -3\ \text{dB})} \times \frac{w_L(R = -3\ \text{dB})}{w_L(R)} \frac{S_0(R = -3\ \text{dB})}{S_0(R)} \qquad (27)$$

where $A(R)$, the phase detector gain, is given by Eq. (9) with no quantization or Eq. (17) with quantization, and $S_0(R)$ is the spectral density at zero frequency, which is constant with 1-bit quantization and varies in inverse proportion to R with no quantization.

The variations in ζ, w_L, and loop SNR are shown in Fig. 12 for both phase detectors. Note that the variations in w_L and loop SNR are valid only for the case when $\zeta = 0.707$ at $R = -3$ dB, but the variation would be similar in other cases. These curves show that ζ, w_L, and the loop SNR all increase monotonically both with and without 1-bit quantization, but that ζ and w_L increase faster with 1-bit quantization, and loop SNR increases faster without quantization. This means that at symbol SNRs higher than the design point, the loop bandwidth is wider with the quantization, so that acquisition should be faster. The higher loop SNRs attained without the quantization are not required and occur at the expense of longer acquisition time.

Reference

1. Tausworthe, R. C., *Theory and Practical Design of Phase-Locked Receivers*, Vol. 1, Technical Report No. 32-819, Chap. 5, Jet Propulsion Laboratory, Pasadena, Calif., February 15, 1966.

Page intentionally left blank

IV. Advanced Engineering: Tracking and Data Acquisition Elements Research

A. Spacecraft CW Signal Power Calibration With Microwave Noise Standards, *C. T. Stelzried*

1. Introduction

The continuous wave (CW) power level received from a spacecraft is an important parameter required for the evaluation of a deep space communication system. A precise measurement method which compares CW signal power with microwave noise power was used to calibrate the *Mariner IV* spacecraft received power level at Mars encounter (Refs. 1 and 2). The technique provides a precision calibration of the test transmitter signal level defined directly at the maser waveguide input reference flange without insertion loss measurements. This is achieved by the *Y*-factor technique of power ratio measurements used in noise temperature calibrations. The method compares the test transmitter CW power with the receiving system noise power, which is determined accurately with calibrated microwave thermal terminations.

2. CW Power Calibration Instrumentation Design Parameters

The present CW power calibration instrumentation consists of the standard low-noise receiving system followed by an IF precision attenuator, narrow-band filter, and power meter detector (Fig. 1). The bandwidth selected for the narrow-band filter is the principal factor which determines the CW signal level calibration range. Decreasing the bandwidth increases the signal-to-noise ratio and hence lowers the signal level calibration range. The present operational system has a 50-MHz center frequency filter with a 10-kHz noise bandwidth (SPS 37-52, Vol. II, p. 68). This system is normally used with input (defined at the maser input reference flange) signal levels between -105 and -125 dBmW.

An analysis has been made to determine the operational penalty for using the present system at lower signal levels or designing a system with a narrower bandwidth to operate at lower signal levels.

The CW signal power (at an operating frequency f_s) at the maser input (Fig. 1) is given by

$$P_{si} = \frac{(Y-1)\,k\,T_{op}\,B}{g(f_s)} \tag{1}$$

where

$$\left.\begin{aligned} g(f_s) &= \frac{G(f_s)}{G(f_0)} \\ B &= \frac{1}{G(f_0)}\int_0^\infty G(f)\,df \end{aligned}\right\} \tag{2}$$

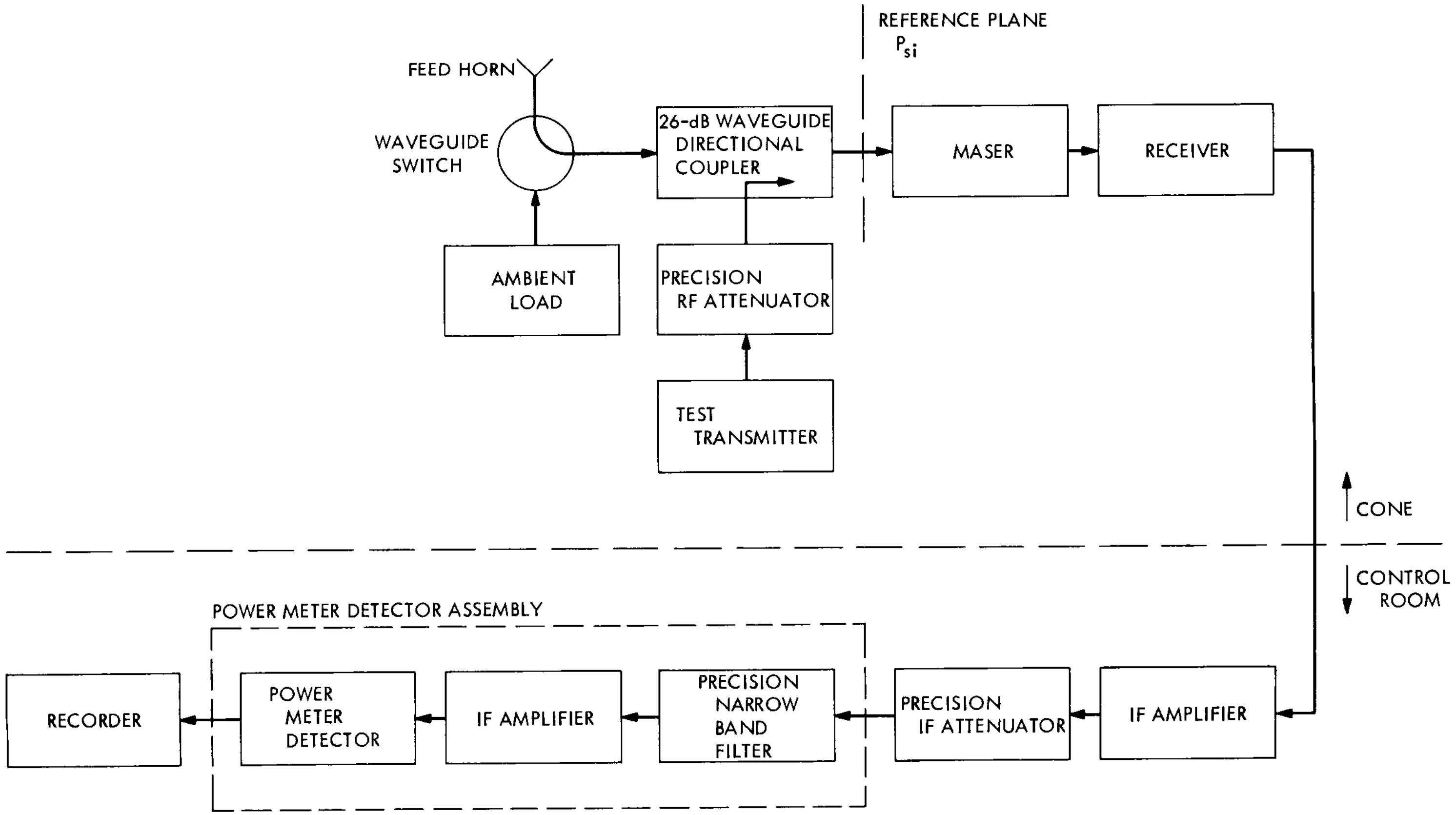

Fig. 1. Simplified block diagram of standard low-noise receiving system with CW power level calibration instrumentation

and

Y = power ratio at the system output between CW signal on and off (measured with the precision IF attenuator), ratio
k = Boltzmann's constant, 1.38054×10^{-23} J/°K
T_{op} = operating noise temperature, °K
$G(f)$ = system power gain at frequency f, ratio
$G(f_s)$ = system power gain at frequency f_s, ratio
$G(f_0)$ = system power gain at frequency f_0, ratio
f_0 = frequency of maximum system gain, Hz

The total probable error of P_{si} (dB) is approximated by

$$PE_{P_{si}}(\text{dB}) \simeq \left[PE^2_{P_{si}/Y}(\text{dB}) + PE^2_{P_{si}/T_{op}}(\text{dB}) + PE^2_{P_{si}/B}(\text{dB}) + PE^2_{P_{si}/g(f_s)}(\text{dB})\right]^{1/2} \tag{3}$$

where

$$PE_{P_{si}/Y}(\text{dB}) = PE_Y(\text{dB}) \frac{Y}{Y-1}$$

equals the probable error of P_{si} contributed by the probable error of Y, dB,

$$PE_{P_{si}/T_{op}}(\text{dB}) = PE_{T_{op}} \left(\frac{10 \log_{10} e}{T_{op}}\right)$$

equals the probable error of P_{si} contributed by the probable error of T_{op}, dB,

$$PE_{P_{si}/B}(\text{dB}) = PE_B \left(\frac{10 \log_{10} e}{B}\right)$$

equals the probable error of P_{si} contributed by the probable error of B, dB, and

$$PE_{P_{si}/g(f_s)}(\text{dB}) = PE_{g(f_s)}(\text{dB})$$

equals the probable error of P_{si} contributed by the probable error of $g(f_s)$, dB.

An estimate of Y is obtained from

$$Y = \frac{P_{si}\, g(f_s)}{k T_{op} B} + 1 \tag{4}$$

using

$$P_{si} = \frac{10^{P_{si}(\text{dBmW})/10}}{1000} \tag{5}$$

with an error of

$$PE_Y(\text{dB}) \simeq \left[PE^2_{Y/A}(\text{dB}) + PE^2_{Y/G}(\text{dB}) + PE^2_{Y/P}(\text{dB}) + PE^2_{Y/J}(\text{dB})\right]^{1/2} \tag{6}$$

where

$$PE_{Y/A}(\text{dB}) = \left\{[A_1(\text{dB})]^2 + [A_2 Y(\text{dB})]^2\right\}^{1/2}$$

equals the probable error of the Y factor measurement due to the resolution A_1(dB) and linearity A_2(dB/dB),

$$PE_{Y/G}(\text{dB}) = \Delta G(\text{dB})$$

equals the probable error of Y contributed by the system gain change G during the Y factor measurement, dB,

$$PE_{Y/P}(\text{dB}) = \Delta P(\text{dB})$$

equals the probable error of Y contributed by the test transmitter level change P during the Y factor measurement, dB, and

$$PE_{Y/J}(\text{dB}) = \frac{0.6745}{\tau B}(10 \log_{10} e)$$

equals the probable error of Y contributed by the noise jitter J, dB, (τ = detector time constants).

These equations have been programmed in Fortran IV and the program designated ID 5877000, CTS35 is available in JPL production with a plot output routine. The symbol designations used in the program are tabulated in Table 1. Figure 2 shows a plot of the probable error

Table 1. Parameter values used for the various test cases shown in Fig. 2

Case identification	B, Hz	PE_B, Hz	τ, s	ΔG, dB
1	10,000	2.0	0.10	0.002
2	10,000	2.0	1.0	0.02
3	100	2.0	0.1	0.002
4	100	0.2	0.1	0.002

$T_{op} = 45$°K, $G(f_s) = 0.0$ dB, $A_1 = 0.002$ dB, $PE_{T_{op}} = 0.3$°K, $PE_{G(f_s)} = 0.002$ dB, $A_2 = 0.004$ dB/dB, $\Delta P = 0.002$ dB.

Table 2. Error analysis of CW power calibration (Case 1)

Errors										
P_{si}, dBmW	P_A, dB	P_J, dB	$P_{\Delta G}$, dB	$P_{\Delta P}$, dB	PE_Y, dB	P_Y, dB	$P_{T_{op}}$, dB	P_B, dB	P_G, dB	PE, dB
−105.0	0.148	0.003	0.002	0.002	0.148	0.148	0.029	0.001	0.002	0.151
−107.0	0.140	0.003	0.002	0.002	0.140	0.140	0.029	0.001	0.002	0.143
−109.0	0.132	0.003	0.002	0.002	0.132	0.132	0.029	0.001	0.002	0.136
−111.0	0.124	0.003	0.002	0.002	0.124	0.124	0.029	0.001	0.002	0.128
−113.0	0.116	0.003	0.002	0.002	0.116	0.117	0.029	0.001	0.002	0.120
−115.0	0.108	0.003	0.002	0.002	0.108	0.109	0.029	0.001	0.002	0.112
−117.0	0.100	0.003	0.002	0.002	0.100	0.101	0.029	0.001	0.002	0.105
−119.0	0.092	0.003	0.002	0.002	0.092	0.093	0.029	0.001	0.002	0.097
−121.0	0.084	0.003	0.002	0.002	0.085	0.085	0.029	0.001	0.002	0.090
−123.0	0.077	0.003	0.002	0.002	0.077	0.078	0.029	0.001	0.002	0.083
−125.0	0.069	0.003	0.002	0.002	0.069	0.070	0.029	0.001	0.002	0.076
−127.0	0.061	0.003	0.002	0.002	0.061	0.063	0.029	0.001	0.002	0.069
−129.0	0.053	0.003	0.002	0.002	0.053	0.056	0.029	0.001	0.002	0.063
−131.0	0.046	0.003	0.002	0.002	0.046	0.049	0.029	0.001	0.002	0.057
−133.0	0.038	0.003	0.002	0.002	0.039	0.043	0.029	0.001	0.002	0.052
−135.0	0.031	0.003	0.002	0.002	0.032	0.038	0.029	0.001	0.002	0.048
−137.0	0.025	0.003	0.002	0.002	0.025	0.033	0.029	0.001	0.002	0.044
−139.0	0.019	0.003	0.002	0.002	0.020	0.030	0.029	0.001	0.002	0.041
−141.0	0.014	0.003	0.002	0.002	0.015	0.027	0.029	0.001	0.002	0.039
−143.0	0.010	0.003	0.002	0.002	0.011	0.025	0.029	0.001	0.002	0.038
−145.0	0.007	0.003	0.002	0.002	0.008	0.025	0.029	0.001	0.002	0.038
−147.0	0.005	0.003	0.002	0.002	0.007	0.027	0.029	0.001	0.002	0.040
−149.0	0.004	0.003	0.002	0.002	0.006	0.033	0.029	0.001	0.002	0.044
−151.0	0.003	0.003	0.002	0.002	0.005	0.044	0.029	0.001	0.002	0.053
−153.0	0.002	0.003	0.002	0.002	0.005	0.063	0.029	0.001	0.002	0.070
−155.0	0.002	0.003	0.002	0.002	0.005	0.095	0.029	0.001	0.002	0.100
−157.0	0.002	0.003	0.002	0.002	0.005	0.147	0.029	0.001	0.002	0.150
−159.0	0.002	0.003	0.002	0.002	0.005	0.229	0.029	0.001	0.002	0.231
−161.0	0.002	0.003	0.002	0.002	0.005	0.360	0.029	0.001	0.002	0.361
−163.0	0.002	0.003	0.002	0.002	0.005	0.567	0.029	0.001	0.002	0.568
−165.0	0.002	0.003	0.002	0.002	0.005	0.896	0.029	0.001	0.002	0.896
−167.0	0.002	0.003	0.002	0.002	0.005	1.417	0.029	0.001	0.002	1.417
−169.0	0.002	0.003	0.002	0.002	0.005	2.243	0.029	0.001	0.002	2.243

Input parameters: $T_{op} = 45°\text{K}$, $B = 1000$ Hz, $\tau = 0.10$ s, $G = -0.00$, $A_1 = 0.002$ dB, $\Delta G = 0.002$ dB, $PE_{T_{op}} = 0.3°\text{K}$, $PE_B = 2.00$ Hz, $PE_G = 0.00$ dB, $A_2 = 0.004$, $\Delta P = 0.002$ dB

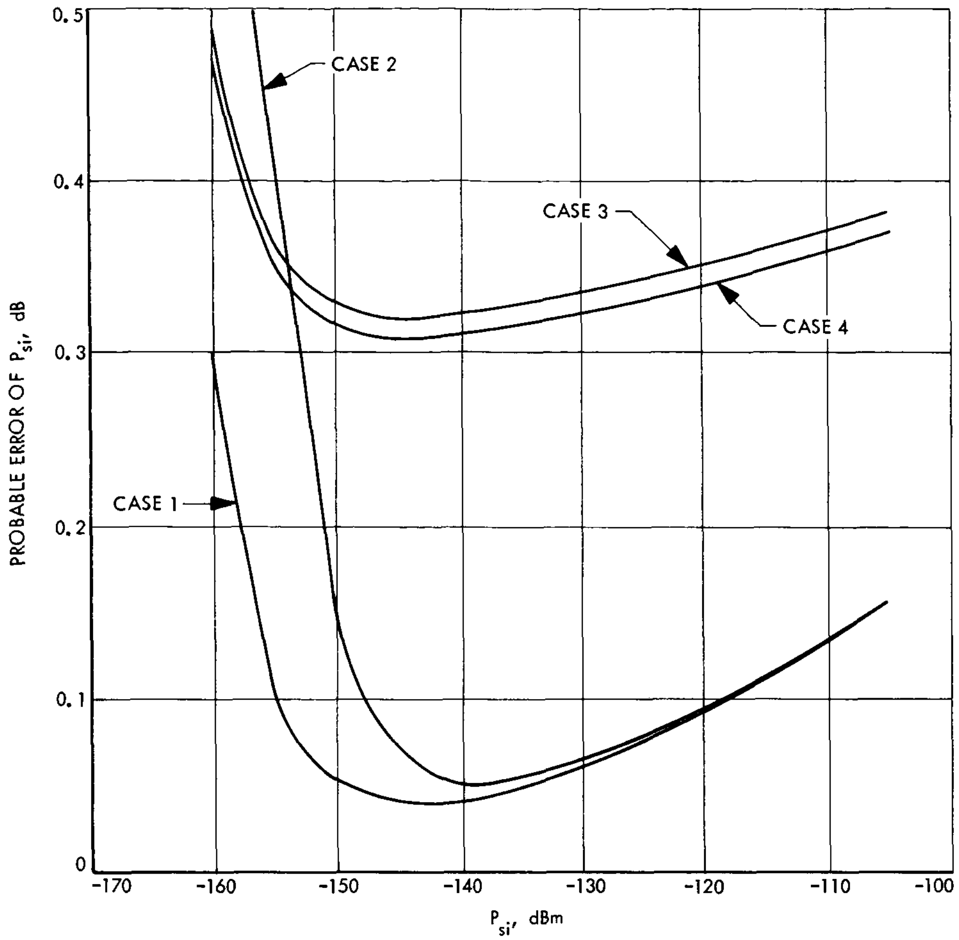

Fig. 2. Probable error of P_{si} vs input signal level for various design parameters

of P_{si} versus input signal level in dBmW for various cases of interest tabulated in Table 1. The computer printout for Case 1 is shown in Table 2. Case 1 most nearly reflects the present operational instrumentation. The greater system gain changes which occur during the Y-factor measurement with longer time constants are reflected in Table 1. Although the minimum measurement error can be reduced at lower signal levels using a narrower bandwidth, the absolute error can actually increase, as with the particular set of parameters considered. The major source of measurement error is due to the Y-factor measurement with the error contributed by the IF attenuator. The analysis also indicates that the calibrations should be made at lower power levels than the present range between −105 and −125 dBmW.

References

1. Stelzried, C. T., and Reid, M. S., "Precision Power Measurements of Spacecraft CW Signal Level with Microwave Noise Standards," *IEEE Trans. Instrumentation and Measurement,* Vol. IM-15, No. 4, p. 318, Dec. 1966.
2. Stelzried, C. T., Reid, M. S., and Nixon, D., *Precision Power Measurements of Spacecraft CW Signal with Microwave Noise Standards,* Technical Report 32-1066. Jet Propulsion Laboratory, Pasadena, Calif., Feb. 15, 1968.

B. *Pioneer VI* Faraday Rotation Solar Occultation Experiment, *G. S. Levy, C. T. Stelzried, and B. Seidel*

1. Introduction

In the second half of November 1968, the *Pioneer VI* probe's orbit will result in a line of sight from the probe to earth that will cause the RF signal to pass through the solar corona and be occulted by the sun. The polarization of the *Pioneer* probe is linear and is spin-stabilized with respect to the plane of the ecliptic. The plane of polarization of the signal received from the *Pioneer VI* spacecraft will be measured. The Faraday rotation produced by the interaction of the RF signal with the solar corona will be inferred from these measurements.

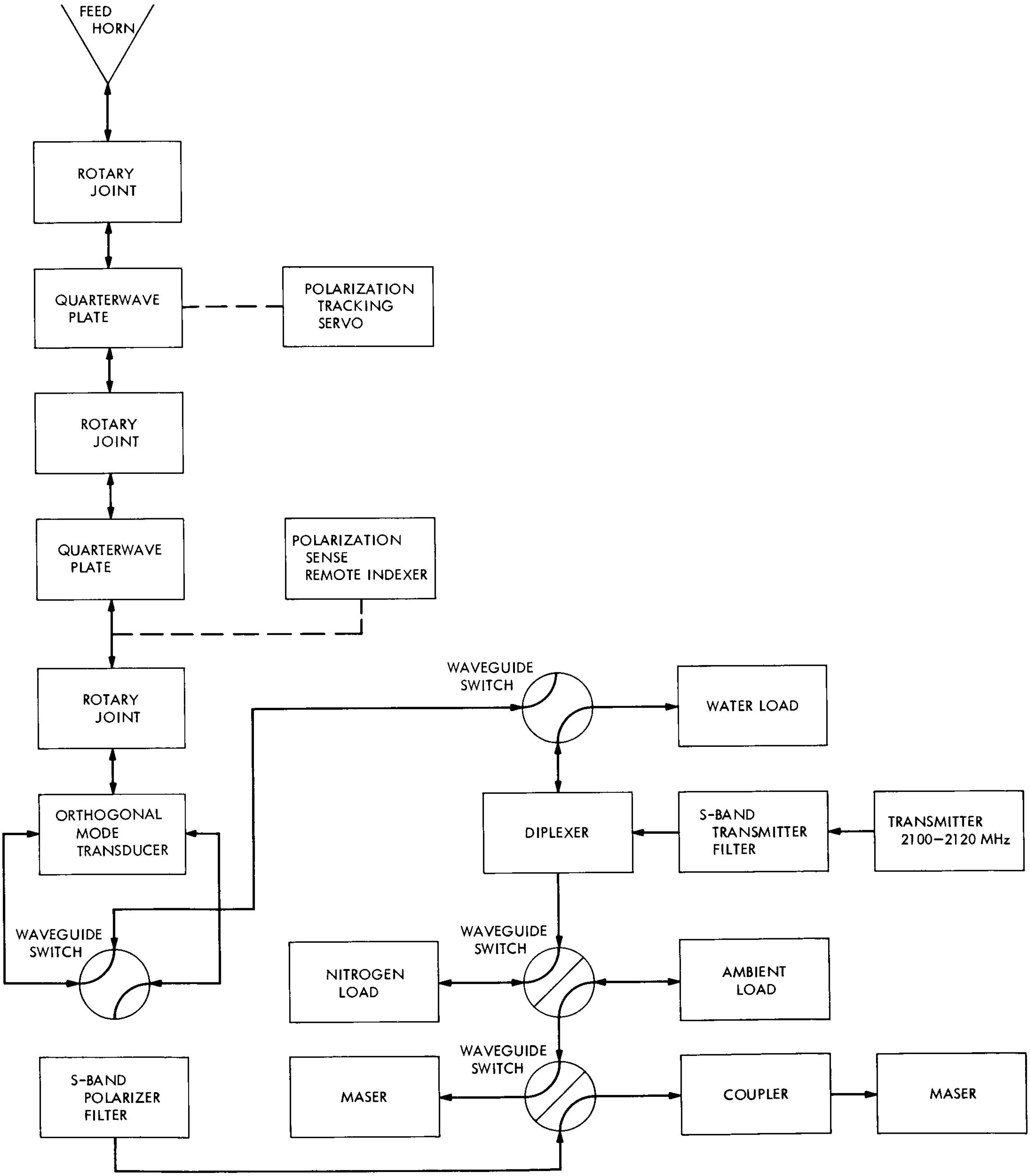

Fig. 3. Simplified block diagram of the S-band multifrequency polarization tracking cone

2. Experiment

The S-band multifrequency cone (SPS 37-35, Vol. IV, pp. 268–270) which was originally on the 210-ft-diam advanced antenna system antenna has been brought back to JPL and modified so that it can use the present monopulse receiver instrumentation to auto-track the plane of polarization. Observations of the apparent plane of polarization of the received S-band signal will be used to deduce some of the electron-density and magnetic-field characteristics of the solar corona.

Figure 3 is a block diagram of the modified multifrequency feed cone. It now has two rotating quarterwave plates placed ahead of the orthomode transducer. These quarterwave plates are rotated between rotary circular waveguide joints. The upper quarterwave plate, when properly oriented with respect to the spacecraft, converts a linear signal into a circularly polarized signal with only one sense of rotation. When improperly oriented with respect to the spacecraft, it also produces some circular polarization with the opposite sense of rotation. The second quarterwave plate converts the two circularly polarized components into two orthogonal linear components which go into two separate ports of the orthomode transducer. One of these ports is treated as the signal port and the second as the error port. The error port provides a signal for servo tracking of the plane of polarization.

The modified cone is scheduled to be returned to the Mars DSS in mid-September. Initially, the plane of polarization of *Pioneer VI* will be tracked using the servo error signal without closing the servo loop. Upon completion of all the servo equipment, full servo control will be used. In addition to the polarization tracking capability of this cone, it can transmit and receive simultaneously either the same or orthogonal polarization on either linear or circular polarization.

Page intentionally left blank

V. Advanced Engineering: Supporting Research

A. 210-ft-Antenna Quadripod Structural Analysis, II, *M. S. Katow*

1. Introduction

In the previous reporting (SPS 37-50, Vol. II, p. 158), two design requirements of the quadripod were discussed. They were:

(1) The STAIR-computed versus field check for the strength to lift the 26-klb feed cone load.

(2) The SAMIS-computed versus field check of the first-mode natural frequency of vibration about the symmetric axis.

This report describes the procedures used to calculate the RF beam boresight errors from computed structural data. These results are compared to those from computations using field-surveyed data. Finally, comparison is made to the operational boresight errors obtained from radio star RF tracking data.

The RF boresight error is calculated from gravity deflection data of (1) the reflector structure, (2) the subreflector quadripod structure, (3) the primary feed cone, and (4) the master equatorial's intermediate reference surface (IRS) mounted on the center hub. Although only the calculations made by JPL are reported here, complete calculations were initially made by the antenna contractor's (Rohr Corp.) engineers to meet the antenna's specifications.

Only the change of RF boresight direction from the zero setting at 45-deg elevation angle to zenith look will be reported here, since comparable results were obtained for the change in elevation angle from 45 deg-to-horizon look, with the exception of wider error tolerances in the limited field checks made below 20 deg elevation angle.

2. Discussion

a. Reflector structure deflection. As noted previously, (SPS 37-40, Vol. IV, p. 181) the output data from the paraboloid best-fitting RMS program provides data for computing the RF boresight direction. As applied to the 210-ft reflector structure, Fig. 1 shows the best-fit paraboloid data for gravity deflection at zenith look, after the setting of the surface panels to a perfect paraboloid at 45 deg elevation. The fit to the STAIR-computed deflections (SPS 37-52, Vol. II, pp. 86–91) is shown at the left side, and the fit to the field measurement is shown on the right side.

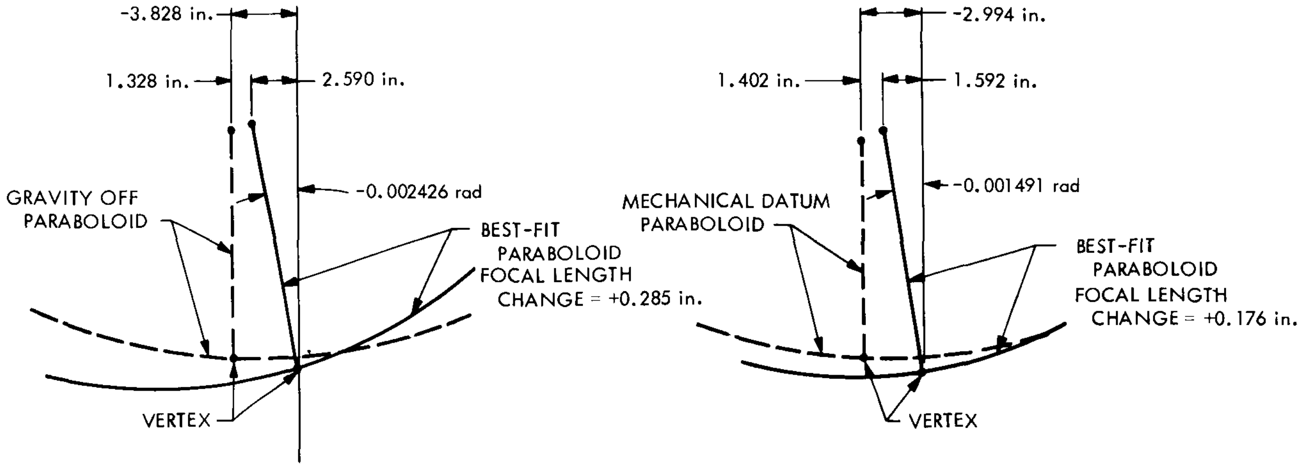

STAIR-COMPUTED

FIELD DATA

Fig. 1. 210-ft reflector structure best-fit paraboloid data—deflections from gravity loading at zenith look, surface panels set to perfect paraboloid at 45-deg elevation angle

The differences in the data comparison are due to the rotated coordinate base used for the field measurements. All field measurements at zenith look are made using datum targets that deflect; this results in a bias difference between the computed and field results. The measured rotation of the datum plane is equal to 0.030 deg as the antenna is rotated from 45-deg elevation angle to zenith look.

b. Subreflector quadripod deflections. Figure 2 illustrates the computed versus field data of the subreflector quadripod deflections that affect the RF boresight direction. For the computed case, the deflections of the quadripod's connections to the reflector structure were STAIR-computed and added to the deflections of the subreflector's secondary focus as computed by the SAMIS program (Refs. 1 and 2). Similarly, the primary feed focus deflections mounted on the cassegrain cone were computed.

Again, there are differences in the deflection data since field measurements are made using the datum targets. The important answers here are the positions of the hyperboloid's secondary foci or the RF phase centers (Fig. 3).

c. RF beam boresight direction. To determine the RF beam boresight direction, a ray from the deflected position of the hyperboloid's secondary focus is reflected from the vertex of the best-fit paraboloid at an angle of reflectance equal to 0.82 times the angle of incidence. This multiplying factor assumes a uniform RF illumination of the paraboloid.

For the computed case, the IRS position was assumed to be fixed to the center hub, and for this case the final RF boresight direction is 0.020 deg down at zenith look measured with respect to the IRS mirror.

The RF boresight direction calculated from field data shows it to be 0.004 deg down at zenith look with respect to the IRS mirror.

d. Operational boresight data. A curve of a radio star RF tracking data[1] is shown in Fig. 4. In this case, the total RF boresight error was read directly from the angle indications of the master equatorial by boresighting the radio star. As shown, the boresight error measured in the declination–hour angle coordinate system of the master equatorial is less than 0.015 deg for the range of local hour angle of plus or minus 45 deg. For lower elevation angles of less than 20 deg, the operational RF boresight data seem at present to indicate larger errors.

The total error in Fig. 4 includes the changes in the IRS mirror position with respect to the RF beam as discussed previously, the master equatorial errors, the error due to the optical tower angular changes, and the ephemeris errors.

---

[1] Data supplied by W. Peterschmidt.

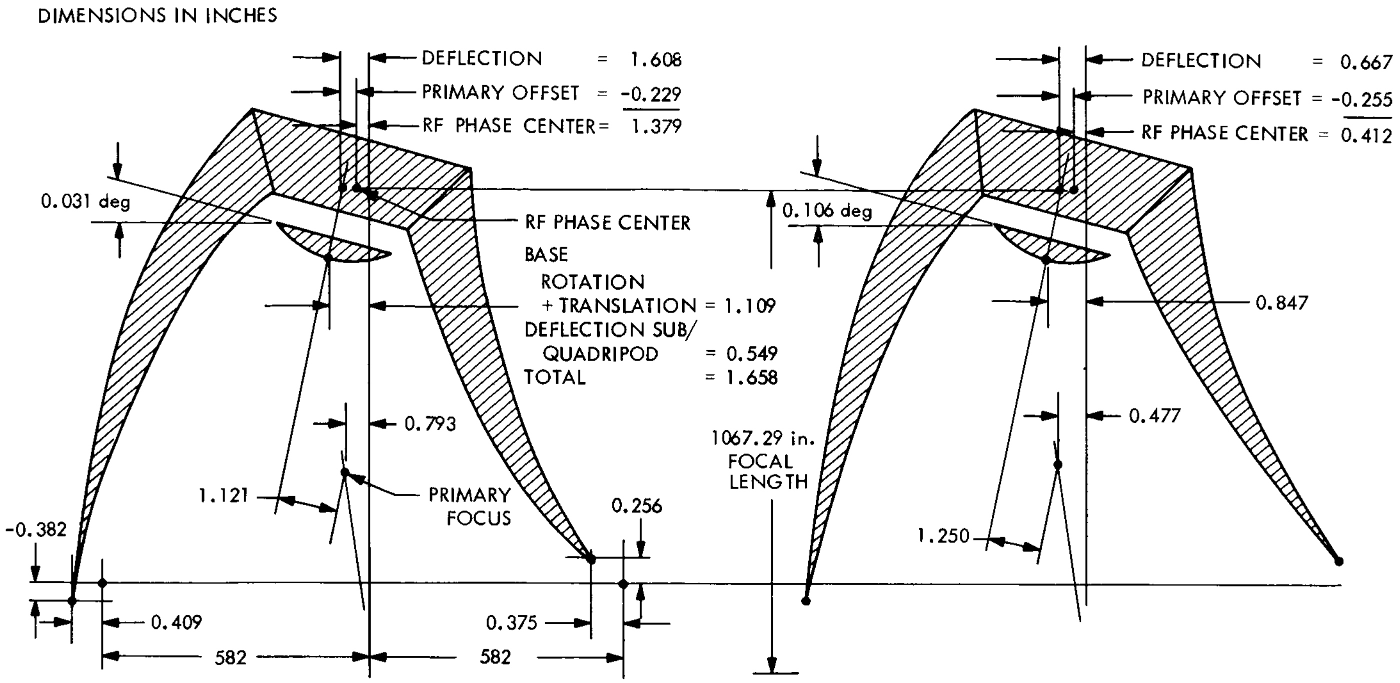

COMPUTED

FIELD DATA

Fig. 2. 210-ft subreflector quadripod gravity deflection data at zenith look, surface panels set to perfect paraboloid at 45-deg elevation angle

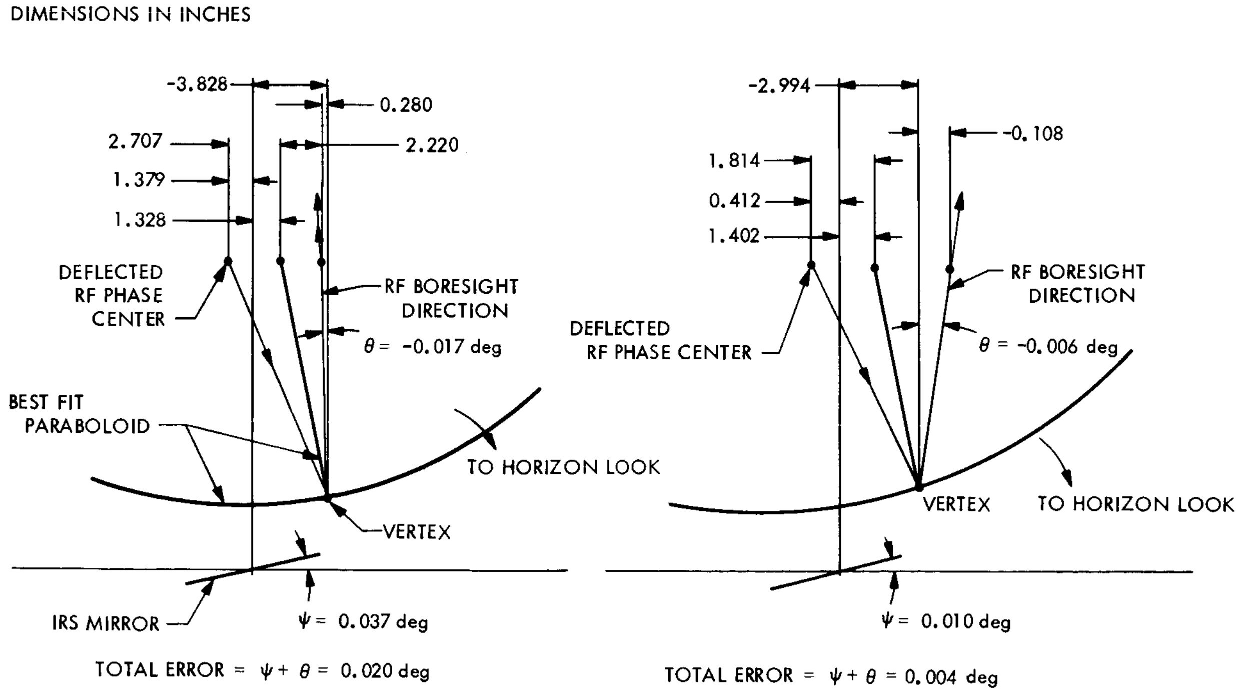

COMPUTED

FIELD DATA

Fig. 3. 210-ft antenna RF beam boresight direction—error at zenith look, zero setting at 45-deg elevation angle

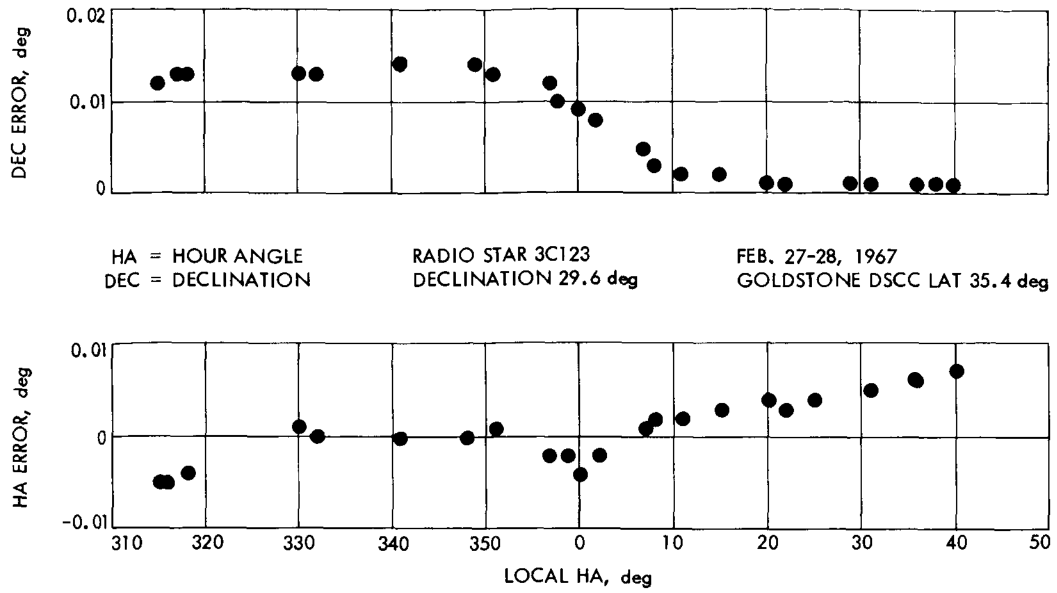

Fig. 4. 210-ft antenna total system RF boresight error—field measurement

3. Conclusions

The RF boresight error with respect to the IRS mirror calculated from the STAIR-computed data and the field measurement data (combined with the best-fit paraboloid data from the RMS program) produced angle errors of 0.020 and 0.004 deg, respectively. Both data assumed perfect alignment at 45-deg elevation angle. The error resulted from the change in direction of the gravity force from 45 deg to zenith look.

The operational data shows more accurate behavior of the pointing system within the measured elevation and hour angles. However, more studies are required, since larger errors are present now at low elevation angles.

References

1. Katow, M. S., Bartos, K. P., and Matsumoto, R., *JPL Modified STAIR System-Operating Procedures,* Technical Memorandum 33-304. Jet Propulsion Laboratory, Pasadena, Calif., June 1, 1968.
2. Lang, T. E., *Summary of the Functions and Capabilities of the Structural Analysis and Matrix Interpretive System Computer Program,* Technical Report 32-1075. Jet Propulsion Laboratory, Pasadena, Calif., April 1, 1967.

B. Joint Integrity Study—Corrosion Effects on Bolted Connections, *V. B. Lobb and F. W. Stoller*

1. Introduction

The DSIF steel antenna structures are exposed to several types of environment in their various locations throughout the world. These antennas, bolted together with high-strength fasteners, are deflection-sensitive structures. Structural weakening, even to the point of excessive deflection or localized yielding, could impair the function of the antenna. Therefore, corrosion control in each antenna is vital.

As a phase of the Joint Integrity program a study was made to evaluate the corrosion protection afforded to structural fasteners and to bolted connections in a highly corrosive salt-spray medium. Protective coatings for both steel and fasteners, such as hot-dipped zinc, electroplated zinc, electroplated cadmium, electroplated tin, mechanically plated zinc, and a zinc silicate paint were evaluated. In addition, a high-strength stainless steel was studied. Concurrently with determining the resistance of these materials to general corrosive attack, bolted connections with fasteners and joint material with different coatings were also exposed to the salt-spray environment to evaluate the galvanic corrosion behavior that might develop from using dissimilar coatings.

Bolted assemblies in which the fasteners and joint material were identically coated were also exposed to the salt-spray test. At the conclusion of the test, these assemblies were sectioned to determine whether, and to what extent, corrosive attack penetrated into the connection.

To determine whether the corrosive attack affected bolt strength, tensile tests were performed on both coated bolts exposed to salt sprays for 1,000 h and unexposed bolts. Since the salt-spray test is only one indicator of corrosion resistance and is not representative of all the environments to which antenna structures may be exposed, a literature search of similar test programs was undertaken.

The results of this investigation and the information gathered from the literature represent a concise state-of-the-art summary concerning the corrosion of exposed steel structures.

2. Test Procedure

Two types of test specimens were employed in the corrosion tests. To determine resistance to corrosion, weight change due to corrosive attack and the effect of corrosive attack on strength properties, ¾-10 × 3 heavy hex structural bolts, conforming to ASTM specification A490 were used. Coating thickness of each specimen was measured with a Permascope. In addition to testing coated bolts, uncoated alloy steel bolts and bolts produced from a new high-strength stainless steel were also exposed to the salt-spray fog.

Six bolts of each type were exposed for a period of 1,000 h. Prior to placing the parts in the salt-spray cabinet, three bolts from each lot were carefully weighed. At approximately 100-h intervals, each of the preweighed bolts was removed from the cabinet, dried, and reweighed.

To determine the corrosion behavior of bolted connections, 3 × 36 × ⅜ in. coupons of ASTM A-36 steel with 13/16-in.-diam holes drilled at their centers were employed. The coupons were bolted together with either ¾-10 × 1¾ A490 heavy hex structural bolts or ¾-10 × 1⅞ A490 high-strength bearing bolts. The test plates were used in the normal black condition and also after being coated with either a zinc silicate paint or hot-dipped zinc.

The bolts were tightened to their proof load, which is the normal clamping load for structural fasteners. The technique used to control bolt preload was measuring bolt length before and after tightening.

The salt spray test essentially consists of exposing the specimens to an environment of humid salt fog created by atomizing a 5% sodium chloride solution. The cabinet is maintained at 95°F, and the concentration of the salt solution, as well as its pH, is closely maintained. Provisions are made to assure a uniformity of the salt fog.

Tensile tests on the ¾ × 3 heavy hex structural bolts were conducted on a 200,000-lb electromechanical universal testing machine. Prior to tensile testing, the corrosion products of the salt-spray test and the remaining coating on the bolts were removed in a solution of inhibited hydrochloric acid which attacks steel at very slow rates. Cleaning of the bolts was accomplished in less than 10 min in all cases, a time short enough to ensure no attack of the steel by the inhibited acid.

3. Results

a. Bolt specimens. All the bolt specimens showed some evidence of corrosive attack in the 1,000-h exposure period. The uncoated bolts and the tin-plated bolts developed red rust within the first 24 h of exposure and exhibited the greatest gains in weight throughout the test. The hot-dipped zinc, electro-deposited zinc, and mechanically plated zinc specimens resisted the formation of red rust for hundreds of hours but developed white corrosion products rather early in the test. The electroplated cadmium coating and the zinc-silicate-painted specimens showed the best visual resistance to red rust formation, being virtually unattacked at the end of the tests. The stainless steel specimens developed a very light rust color early in the test, which did not change substantially throughout the tests.

Figure 5 illustrates the time to red rust formation for each coating. The correlation between the weight change data and the visual observations of corrosion rates was quite good. Only the uncoated and the tin-plated specimens resulted in continuously increasing weight changes throughout the 1,000-h test. The cadmium-coated specimens underwent virtually no change in weight, while the weight changes for all of the zinc coatings, including the zinc silicate paint, showed a tendency for the weight change to stabilize with time. This would not be expected to continue indefinitely, however, since weight change would undoubtedly occur as the formation of red rust developed. The stainless steel specimens, although noticeably discolored throughout most of the test period, underwent very little change in weight, showing a slight decrease in weight early in the test and a very minor weight gain in the second half of the test.

Figure 6 illustrates the net weight change experienced in 1,000 h for each type of bolt specimen tested. A pictorial representation of the appearance of each type of specimen tested is presented in Fig. 7.

Four basically different corrosion behavior patterns were observed in this phase of the test program.

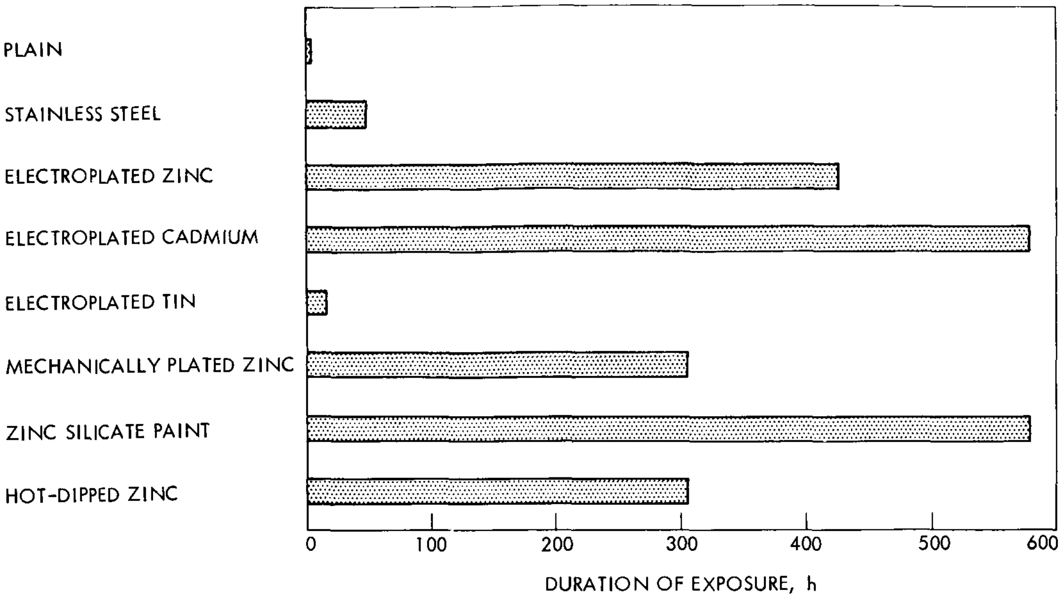

Fig. 5. Exposure time to first indication of red rust

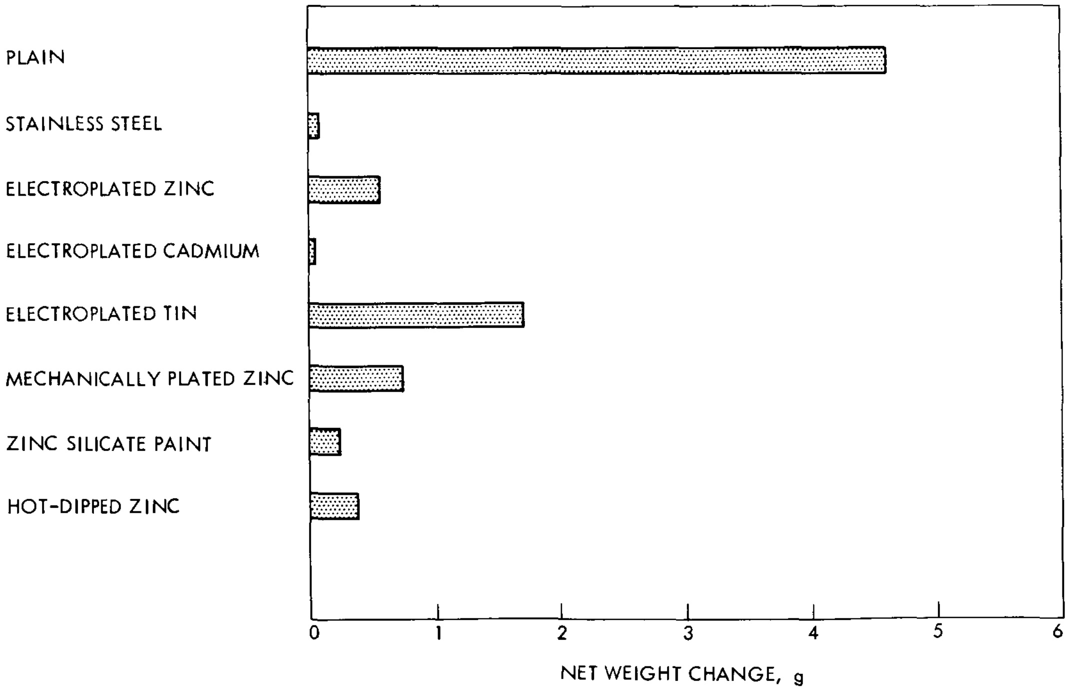

Fig. 6. Net weight change after 1000-h exposure

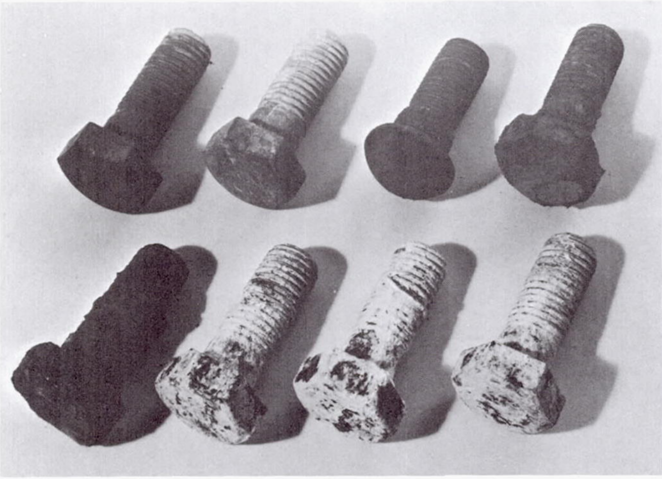

Fig. 7. Typical bolt specimens after 1000-h salt spray exposure

The first was the formation of red rust almost immediately after exposure, and the continual buildup of the corrosion product.

The second was the formation of a white corrosion product which quickly covered the specimen, as was the case for the electroplated zinc, the hot-dipped zinc, and the mechanically deposited zinc coatings. The chromate treatment applied to the electroplated-zinc parts retarded the formation of this corrosion product for some 200 h, as is readily apparent from the weight change data. However, once this white corrosion product was fully developed, little change in specimen weight occurred. Eventually this white corrosion product became dotted with red rust spots, indicating that the sacrificial protection of the zinc was exhausted.

The third was the almost complete lack of any change in appearance throughout the test, which was the case for the electro-deposited cadmium-plated specimens. No change in appearance was noted until 570 h of exposure, when extremely fine red rust spots were noticed. The same was true for the zinc silicate paint, except that a slight darkening of the coating occurred almost immediately after exposure. Here, again, fine rust spots were noticed at 570 h of exposure, and, as in the case of the cadmium, no appreciable increase in the number or size of the rust spots was noted.

The fourth was the formation of a light red oxide product which developed in the first 50 h of exposure on the stainless steel. It had the form of a stain rather than a corrosion product. Although discoloration of the specimens increased slightly throughout the test, no severe deleterious effect on the stainless steel could be expected. This behavior is further confirmed by the weight change data.

After the 1,000-h exposure period, three specimens of each type were cleaned of all corrosion products and any remaining coating and then were tensile-tested. The ultimate strength and total bolt elongation were determined for each specimen and are presented in Table 1.

As a result of the 1,000-h exposure, the plain finish and the tin-plated bolts had noticeably lower tensile

Table 1. Tensile behavior of bolt specimens exposed to 1000-h salt spray

Specimen	Ultimate bolt load, lb	Ultimate strength, psi	Total elongation, in.
Steel control lot	62,500 61,600 61,900	187,300 184,600 185,400	0.225 0.225 0.225
Plain finish	59,200 58,400 58,600	177,200 174,900 175,400	0.235 0.235 0.235
Electroplated zinc	61,500 62,100 62,300	184,100 186,000 186,600	0.225 0.220 0.225
Electroplated cadmium	61,400 61,200 61,600	183,800 183,200 184,400	0.235 0.235 0.220
Electroplated tin	59,600 60,200 61,000	178,400 180,200 182,600	0.235 0.220 0.230
Mechanically plated zinc	61,600 61,600 61,800	184,400 184,400 185,000	0.225 0.235 0.225
Zinc silicate paint	61,200 61,800 61,800	183,200 185,000 185,000	0.230 0.235 0.235
Hot-dip galvanized zinc	61,000 61,600 61,200	182,600 184,400 183,200	0.235 0.230 0.220
Stainless steel control lot	67,000 67,500 66,500	200,600 202,100 199,100	0.275 0.275 0.285
Stainless steel	67,300 67,600 66,900	201,500 202,400 200,300	0.285 0.280 0.275

strength, although their elongation properties were not affected. Both of these specimens were heavily pitted as a result of the salt spray exposure while none of the other specimens were affected. The tensile strength and elongation values of the other bolt specimens compared favorably with the unexposed control lot of bolts. The tensile properties of the stainless steel bolts were compared to the same properties of unexposed bolts, and no difference in properties was detected.

b. Joint specimens. The purpose of evaluating the performance of bolted joints was twofold: (1) to gain a more quantitative evaluation of galvanic effects between dissimilar metals, and (2) to determine whether the corrosion of bolted connections is confined to the surface of the structure, or whether corrosive attack penetrates into the structure along the bolt holes.

Where the joint-coating material and the bolt-coating material were similar, as in the case of hot-dip galvanized plates bolted by any metallic zinc coating, the specimens corroded in identically the same manner as the bolt specimens. Where the bolt coating and the joint coating differed, galvanic action caused the more anodic material to sacrificially corrode to protect the cathodic material.

The galvanic behavior of dissimilar metals in contact with a conducting medium is dramatically illustrated in Fig. 8 where the corrosion of tin-coated bolts in uncoated steel, hot-dip galvanized joints, and zinc-silicate-painted joints is compared with the corrosion of the tin-plated bolts exposed to the 1,000-h salt-spray test without cathodic protection. Since tin is cathodic to both steel and zinc, the tin-coated bolts in the connections were protected. Even in uncoated steel connections, rusting of the tin-plated bolts was not observed until 46 h had elapsed. The degree of corrosion of the tin-plated bolts was such that only 60% of the bolt's surface was rusted after 1,000 h. In the hot-dip galvanized and zinc-silicate-painted joints, less than 20% of the bolt's surface was rust-covered after the test. In the normal galvanic behavior, the joint material or coating should corrode at a more rapid rate under such conditions. While this was observed in the case of the uncoated and the hot-dip galvanized plates, it was not observed in the zinc-silicate-painted connections. The fact that there was no increase in the rate of attack on the zinc-silicate-painted plates demonstrates the excellent corrosion resistance of this coating in a humid salt-spray environment.

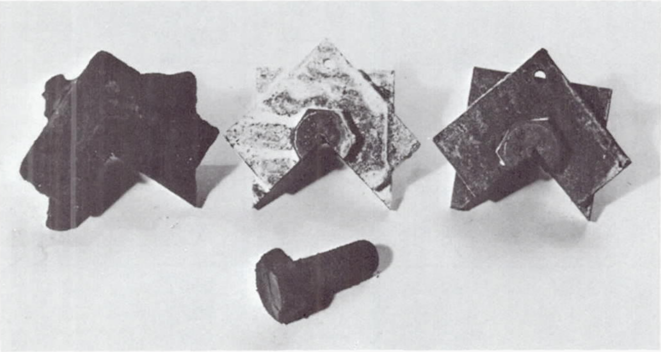

Fig. 8. Relative corrosion tin-plated bolts, and tin-plated bolts in plain steel plates, hot-dip galvanized plates and zinc-silicate-painted plates

Cadmium-plated bolts also underwent galvanic attack when used to join uncoated steel plates. In this case, the cadmium was anodic to the steel and sacrificially corroded. Red rust was noticed after 600 h exposure, and by the end of the test completely covered the bolt's surface. This behavior is decidedly different from that of the cadmium-plated bolt specimens in hot-dip galvanized plates, zinc-silicate-painted plates, or the uncoated bolts after exposure to the salt spray. Such behavior was expected, since zinc and cadmium have similar electrochemical potentials in sea water, an environment similar to a humid salt spray.

Zinc is anodic to steel and is expected to protect uncoated steel by sacrificial corrosion in virtually all environments, including salt spray. This behavior is well-documented in the literature, but this effect is limited to relatively small exposed areas of steel in contact with zinc. In the case of hot-dip galvanized plates or zinc-silicate-painted plates bolted with uncoated steel bolts, the relative area of the bolt heads is too great to gain any reasonable degree of cathodic protection from the zinc-coated plates. The uncoated bolts were corroded to a similar extent whether they were exposed alone or in uncoated, hot-dip galvanized, or zinc-silicate-painted plates.

In the case of electroplated zinc bolts, hot-dip galvanized bolts or mechanically zinc-plated bolts, very little behavior in corrosion rate was observed between the rate of bolt corrosion in either hot-dip galvanized or zinc-silicate-painted plates and the rate observed for the bolt specimens themselves. However, when bolts coated with metallic zinc by any means were used to join unprotected steel plates, corrosion of the zinc-coated bolts was accelerated, and greater amounts of red rust were apparent after the 1,000-h salt spray exposure.

In cases in which stainless steel fasteners were used to bolt the plates together, the visual appearance of the bolts was identical to that of the stainless steel bolt specimens. In joints made of both hot-dip galvanized plates and zinc-silicate-painted plates, it was observed that a preferential attack of the plates took place at the perimeter of the fasteners. This is attributed to the great difference in electrochemical potential between passivated stainless steel and zinc.

At the conclusion of the 1,000-h salt spray exposure test, each joint specimen was sectioned through the bolt line and examined for evidence of penetration of corrosion products into the joint through the bolt hole or along the faying surfaces. No evidence of penetration of the corrosion products into the joints was observed in any type of connection whether a large amount, a mild amount, or virtually no corrosion products were present on the surfaces. This was true in cases where hole-filling high-strength bearing bolts or nonhole-filling structural bolts were used.

4. Summary

The corrosion protection of structural members involves a choice between hot-dip galvanizing and zinc silicate paint, since electroplating is impractical for large sections. In the current literature on this subject, far greater life is claimed for hot-dip galvanized coatings than for zinc silicate paints, but the newness of the zinc-rich paints makes accurate predictions of service life hazardous. The hot-dipped zinc coating has the advantage of good historical data to substantiate its selection over zinc-rich paints. However, the corrosion product of the zinc-rich paint is far less voluminous, and therefore less likely to flake off during service, than the corrosion product of hot-dipped zinc.

This study shows that zinc silicate paint provides corrosion protection equal to that of hot-dip zinc coating. However, it has not yet been critically tested in structures exposed for decades in various atmospheric environments.

When structural members are either hot-dip galvanized or coated with zinc silicate paint, the fastener coating must be electrochemically compatible with zinc and preferably anodic to steel. This immediately excludes tin and stainless steel since both force serious sacrificial corrosion of the structural member's coating. The process of applying zinc silicate paint to structural fasteners is inexact, and control of the thread contour of the fasteners is impossible. This is also true of hot-dip galvanized coatings. In these cases the nuts are tapped oversize by 1/32 in. order to permit the fasteners to be assembled. The hot-dip galvanized coating is also quite brittle and frequently flakes off during shipment and assembly.

Strong evidence is now available that the corrosion protection of metallic zinc depends not upon the method of application but upon the thickness and density of the zinc.

This evidence presents a strong argument for the use of either electroplated or mechanically plated zinc as the protective coating for structural fasteners. In either process the form of the thread elements on the fasteners can be controlled, and the zinc coating is more ductile and adherent to the fasteners than the hot-dip galvanized coating. In recent tests the adhesion of hot-dip galvanized mechanically plated zinc and electroplated zinc coatings of identical thickness was evaluated. The electroplated zinc was rated best, showing the least amount of chipping or flaking under conditions of impact assembly. The mechanically plated zinc coating was rated second, and the hot-dip galvanized coating was rated as the poorest of the three.

Since chromate conversion coatings can be applied easily to electroplated zinc and also to mechanically-plated zinc coatings and are extremely effective in reducing the formation of gross corrosion products of zinc, they are strongly recommended for zinc-plated fasteners.

The use of cadmium-plated steel fasteners is advisable only in marine applications where its corrosion resistance is excellent and it is electrochemically compatible with zinc. Its use should be avoided in industrial environments. Cadmium is not always anodic to steel; in certain environments it can be cathodic and, as such, would accelerate the rate of attack on any exposed steel galvanically connected to the cadmium.

By a process of elimination, then, zinc appears to be the most desirable protective coating for steel structures exposed to atmospheric environments.

For bolted structures, zinc silicate paint is the preferable coating for the structural members and electroplated zinc with a chromate finish for the fasteners.

The penetration of corrosion products into the actual joint, either through the bolt hole or along the faying surfaces, was investigated for different degrees of corrosion. It was found that there was no evidence of penetration of corrosion into the joint, no matter how severely the exterior of the joint was corroded. The joints investigated were all high-strength, high-tension bolted joints with high clamp loads. Both the plain hex bolts and the bearing bolts were used, and both types of bolts prevent corrosion products from penetrating the joint. On larger or multibolt joints, corrosion products may penetrate the joint but will not penetrate the area within a 1-½ bolt diameter of the bolt center.

C. FLIGHT, a Subroutine to Solve the Flight Time Problem, *H. F. Lesh and C. Travis*

1. Introduction

Preliminary trajectory studies for spaceflight mission design often begin with the calculation of conic trajectories which assume that the only gravitational mass is the sun. For these studies, the central computational problem is the calculation of the conic trajectory which starts at the massless point P_1 at time t_1 and arrives at the massless point P_2 at time t_2.

There is an entire family of conic trajectories from a point P_1 to a point P_2, three of which are shown in Fig. 9. The flight times for these trajectories increase, however, as the average distance of the trajectory from the sun increases. Since the flight time must be $t_2 - t_1$, only one member of the family shown in Fig. 9 will do.

Lambert's theorem states that, for a fixed central body, the time to traverse a trajectory depends only upon the length of the semimajor axis a of the trajectory, the sum $r_1 + r_2$ of the distances of the initial and final points of the trajectory from the central body, and the length c of the chord joining these points. Stated functionally, Lambert's theorem states that $t_f = t_f(r_1 + r_2, c, a)$. By fixing the vector positions of the two planets, $r_1 + r_2$ and c are also fixed. With the vector positions of the two planets fixed, the flight time becomes a function of the semimajor axis only.

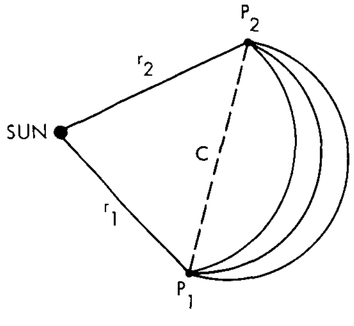

Fig. 9. Members of the family of trajectories from P_1 to P_2

If the functional relationship $t_f(r_1 + r_2, c, a)$ is derived in terms of trigonometric and hyperbolic-functions directly, then the formulas for the elliptic, parabolic, and hyperbolic cases are all different. In fact, the elliptic case alone must be treated with four different formulas, one for each subcase. The subcases depend on the flight time and the angle θ between $\mathbf{r}_1$ and $\mathbf{r}_2$. If the flight time is treated as a function of the semimajor axis a, difficulties arise because of the odd nature of the flight time dependence on a at $a = a_{\min}$, as shown in Fig. 10.

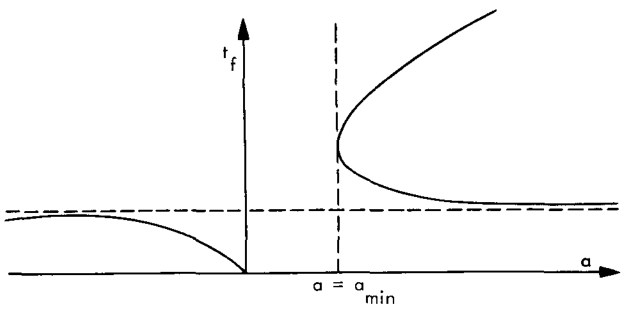

Fig. 10. Flight time versus semimajor axis

By replacing the semimajor axis a with a new independent variable x, and by introducing two new transcendental functions $S(x)$ and $C(x)$, it is possible to combine all the special cases of the flight-time formula into one single formula whose solution in terms of the new independent variable x is much better behaved than the solution of the original equations in terms of a. This article describes a subroutine which implements this method. The accuracy and speed of this method are also discussed.

2. Equational System

The functions $S(x)$ and $C(x)$ are defined as

$$\left.\begin{aligned} S(x) &= \frac{(x)^{1/2} - \sin (x)^{1/2}}{(x^{1/2})^3}, && x > 0 \\ &= \frac{\sinh (x)^{1/2} - (-x)^{1/2}}{(x^{1/2})^3}, && x < 0 \\ &= \frac{1}{6}, && x = 0 \end{aligned}\right\} \quad (1)$$

$$\left.\begin{aligned} C(x) &= \frac{1-\cos(x)^{1/2}}{x}, & x>0 \\ &= \frac{\cosh(-x)^{1/2}-1}{-x}, & x<0 \\ &= \frac{1}{2}, & x=0 \end{aligned}\right\} \quad (2)$$

Graphs of these functions appear in Fig. 11.

These functions may be defined by their Taylor series expansions:

$$\left.\begin{aligned} S(x) &= \frac{1}{3!} - \frac{x}{4!} + \frac{x^2}{5!} \cdots \\ C(x) &= \frac{1}{2!} - \frac{x}{3!} + \frac{x^2}{4!} \cdots \end{aligned}\right\} \quad (3)$$

In order to develop the universal flight-time formulas, introduce the parameter

$$Q = \frac{s-c}{s}$$

where

$$\left.\begin{aligned} c &= (r_1^2 + r_2^2 - 2r_1 r_2 \cos\theta)^{1/2} \\ s &= \frac{(r_1 + r_2 + c)}{2} \end{aligned}\right\} \quad (4)$$

Here c is the length of the chord joining the initial and final points of the trajectory, and s is half the perimeter of the triangle formed by the central body, the launch planet, and the target planet.

The universal flight-time formula is

$$T = \frac{S(x)}{C^{3/2}(x)} \mp Q^{3/2}\frac{S(y)}{C^{3/2}(y)} \quad (5)$$

$$yC(y) = Q\,x\,C(x) \quad (6)$$

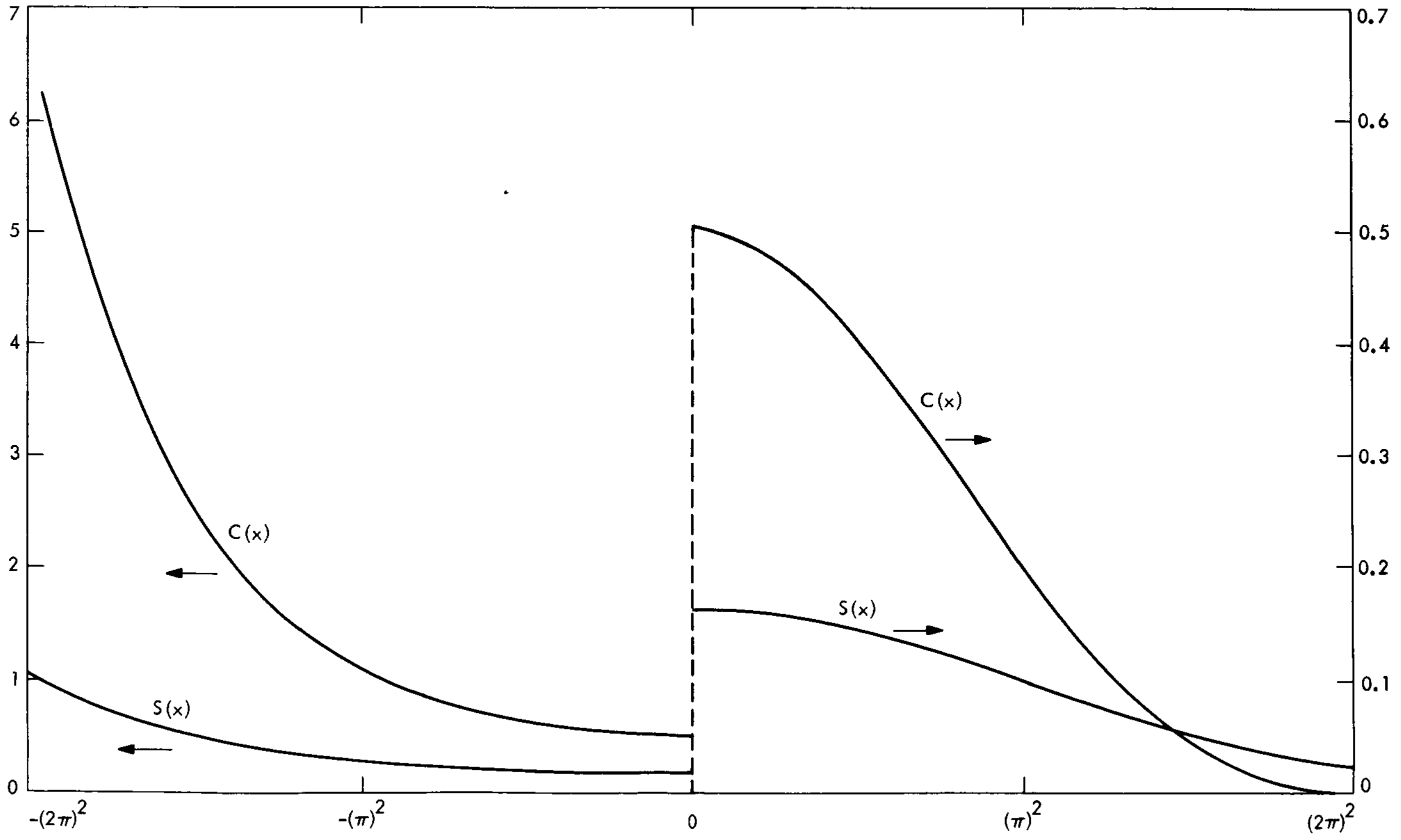

Fig. 11. Special transcendental functions

where

$T = (\mu/s^3)^{1/2} t_f$

t_f = flight time

μ = gravitational parameter of the central body

The choice of the upper or lower sign is made according to whether the angle θ is less or greater than 180 deg, respectively.

Figure 12 shows the family of curves of all possible solutions to these equations as a function of the parameter Q. If $c = s$, then $Q = 0$; this case represents the 180-deg transfers (dark line at middle of curves, Fig. 12). In any other case, $x > c$ and Q is less than 1.0. For each value of Q less than 1.0, there are two cases, one in which the transfer angle is less than 180 deg (curves below 180-deg transfer line), and one in which it is greater than 180 deg (curves above 180-deg transfer line). Values of x less than zero represent hyperbolic transfers. The value $x = 0$ corresponds to the parabolic transfers. Values of $x > 0$ represent elliptic transfers. The value $x = \pi^2$ is associated with trajectories which have minimum energy with respect to the central body.

The development of Eqs. (5) and (6) is too long and complex to reproduce here. It may be obtained from Ref. 1. The derivations are scattered throughout this reference, and the following steps in the derivations may be found in these locations:

(1) The two-body problem (to the point of determining the shape of the orbit) on pp. 15 and 16.

(2) The *vis viva* equation and Kepler's equation on pp. 50 and 51.

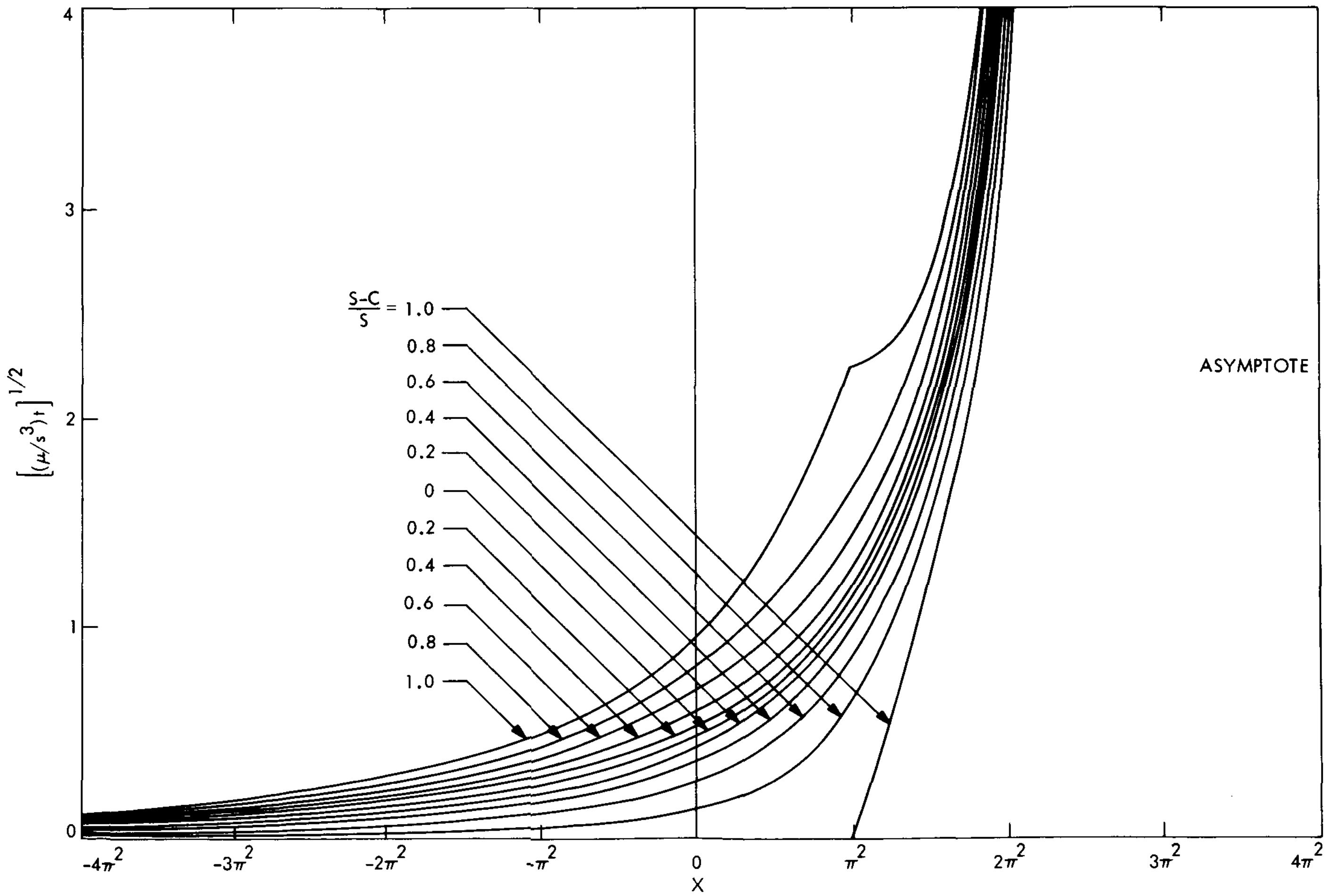

Fig. 12. Family of solutions of Lambert's problem (from Ref. 1)

(3) Lambert's theorem proved from Kepler's equation on p. 71.

(4) The basic flight-time formula and an analysis of the many special cases of this formula, using the *vis viva* equation and Lambert's theorem, on pp. 72–78.

(5) The use of the special functions $C(x)$ and $S(x)$ to amalgamate all the special cases of the flight-time formula into one equation on pp. 80 and 81.

3. Method

a. Elimination of double iteration. Equations (5) and (6) are two transcendental equations in x and y. Rather than solve Eq. (6) by iteration, after having picked a value of x, the following formula was derived which gives y from x without iteration with only two cases.

$$\left.\begin{aligned} y &= 4 \operatorname{arc} \sin^2 \left[\left| \frac{xsC(x)}{2} \right| \right]^{1/2}, \qquad x \geq 0 \\ &= -4 \ln^2 \left\{ \left[\left| \frac{xsC(x)}{2} \right| \right]^{1/2} + \left[\left| \frac{xsC(x)}{2} \right| + 1 \right]^{1/2} \right\}, \\ &\qquad\qquad\qquad\qquad\qquad\qquad x < 0 \end{aligned}\right\} \quad (7)$$

b. Basic iteration. Newton's method is used to solve Eq. (5) given T and Q. The iteration formula is

$$x_{n+1} = x_n - \frac{T(x_n) - T}{T'(x_n)} \quad (8)$$

where

$$T(x) = \frac{S(x)}{C^{3/2}(x)} + Q^{3/2} \frac{S(y)}{C^{3/2}(y)} \quad (9)$$

$$T'(x) = \frac{1 + k \{ \mp Q^{3/2} - 1.5 \, [2 - yC(y)]^{1/2} \, T(x) \}}{2x \, (C(x))^{1/2}} \quad (10)$$

$$\left.\begin{aligned} k &= - \frac{[2 - xC(x)]^{1/2}}{[2 - yC(y)]^{1/2}}, \qquad x > \pi^2 \\ &= + \frac{[2 - xC(x)]^{1/2}}{[2 - yC(y)]^{1/2}}, \qquad x \leq \pi^2 \end{aligned}\right\} \quad (11)$$

At $x = \pi^2$, $2 - xC(x) = 2 - yC(y) = 0$. However,

$$\lim_{x \to \pi^2} \left[\frac{2 - xC(x)}{2 - yC(y)} \right]^{1/2} = 1$$

Therefore if

$$| 2 - yC(y) | < 10^{-4}$$

then k is taken to be 1.0.

At $x = 0$, the formula for $T'(x)$ breaks down because of the x in the denominator. For this reason $T'(x)$ is taken to be

$$\frac{1 \mp Q^{3/2}}{2\pi^2}, \qquad |x| < 10^{-6}$$

Since this value of $T'(x)$ is only a rough approximation to the true derivative at $x = 0$, convergence of Newton's method will be somewhat slower in the very near vicinity of $x = 0$.

Formula (10) for the derivative is not the one that appears in Ref. 1 on p. 82 (which is incorrect). The quantity

$$[2 - xC(x)]^{1/2}$$

should be replaced by

$$[2 - xC(x)]^{1/2}, \qquad x < \pi^2$$

and

$$-\,[2 - xC(x)]^{1/2}, \qquad x \geq \pi^2$$

c. Starting. To determine a good starting value for x, a rough empirical curve fit was made to x as a function of T and Q. First, a hyperbola was fit to the 180-deg transfer line of Fig. 12, giving x as a function of T for $Q = 0$ as

$$\begin{aligned} x_1 &= 82.1678 + 352.8045T \\ &\quad - (123954.8504T^2 + 43904.0083T + 13423.6819)^{1/2} \end{aligned}$$

Next a correction to x for nonzero values of Q was determined. The correction is

$$\Delta x(T,Q) = \mp \left(\frac{2.36}{T^2 + 0.15} + \frac{3.5}{T + 0.1} \right) (0.3Q^2 + 0.7Q)$$

The initial guess is taken to be

$$x = x_1 - \Delta x(T,Q)$$

```
C**** CALLING SEQUENCE *****
C      CALL FLIGHT(R1,R2,THETA,GM,TF,A,N)
C*
C*
C**** INPUT *****
C      THE UNITS OF THE INPUT CAN EITHER BE (AU - DAYS) OR (KM - SEC)
C         R1 = LAUNCH RADIUS (AU OR KM)
C         R2 = TARGET RADIUS (AU OR KM)
C      THETA = CENTRAL ANGLE (RADIANS)
C         TF = TIME OF FLIGHT (DAYS OR SEC.)
C         GM = GRAVITATIONAL PARAMETER OF THE CENTRAL BODY (MU)
C              (AU**3/DAY**2 OR KM**3/SEC**2)
C*
C*
C**** OUTPUT *****
C      A = SEMI-MAJOR AXIS (AU OR KM)
C      N = ERROR RETURN
C        N = 0     NO ERROR
C        N = 1     ERROR IN INPUT.  THERE WAS EITHER AN OVERFLOW OR A
C                  DIVIDE CHECK CAUSED BY EITHER HAVING R1, R2, OR T
C                  TOO LARGE OR BY HAVING R1 = R2 = 0.
C*
C*
C**** RESTRICTIONS *****
C      A)  R1, R2, THETA, TF SHOULD BE POSITIVE
C
C      B)  IF T = SQRT(MU/S**3) * TF  IS LESS THAN .000001, THE SUBROUTINE
C          COMPUTES THE SEMI-MAJOR AXIS FOR T EQUAL TO .000001
C
C      C)  IF T = SQRT(MU/S**3) * TF  IS GREATER THAN 950,000 THE SUBROUTINE
C          COMPUTES THE SEMI-MAJOR AXIS FOR T EQUAL TO 95C,000
C*
C*
      SUBROUTINE FLIGHT(R1, R2, THETA, GM, TF, A, K)
      CALL OVERFL(L)
      CALL DVCHK(M)
      C = SQRT(R1**2 + R2**2 - 2.0*R1*R2*COS(THETA))
      S1 = (R1 + R2 + C)/2.0
      S = 1.0 - C/S1
      T = SQRT(GM/S1**3)*TF
      T = AMIN1(T,950000)
      T = AMAX1(T,.000001)
      V = 1.0
      K = 0
      DATA BIGNO/0377777777777/
      CALL DVCHK(M)
      CALL OVERFL(L)
      IF(M+L-3) 400, 400, 500
  400 N = 1
      RETURN
  500 IF(THETA - 3.1415926) 40, 40, 30
   40 V = -1.0
   30 X1 = 82.1678 + 352.8045*T - SQRT(123954.8504*T*T + 43904.0083*T +
     113423.6819 )
      X = X1 - V*(.3*S*S + .7*S)*(2.36/(T*T + .15) + 3.5/(T+.1))
      X = AMIN1(X, 38.7)
      B1 = SQRT(S)**3
      N = 1
  106 CALL SERIES(X, SX, CX)
      U = 1.0
      ROOT = SQRT(ABS(S*X*CX/2.0))
      IF(X) 107,108,108
  107 E = ROOT + SQRT(ROOT**2 + 1.0)
      Y = -4.0*ALOG(E)**2
      GO TO 109
  108 Y =  4.0*ARSIN(ROOT)**2
  109 CALL SERIES(Y, SY, CY)
      TIME = SX/SQRT(CX)**3 +V*B1*SY/SQRT(CY)**3
      IF(ABS(TIME - T) - T* 1.0E-5) 111, 111, 110
  110 CHECK = ABS(2.0 - Y*CY)
      IF(CHECK - 1.0E-4) 112, 112, 113
  112 AMISS = 1.0
      GO TO 114
  113 AMISS = SQRT((2.0 - X*CX)/(2.0 - Y*CY))
  114 DEM = AMISS*(V*B1 - 1.5*SQRT(CHECK)*TIME)
      IF(X - 9.8696044) 120, 120, 121
  121 U = -1.0
      IF(ABS(X) - .0001) 50, 120, 120
   50 SLOP = (1.0 + V*S)/19.739209
      GO TO 122
  120 SLOP = (1.0 + U*DEM)/(2.0*X*SQRT(CX))
  122 X = X- (TIME - T)/SLOP
      X = AMIN1(X, 39.14553)
      X = AMAX1(X, -823.0473)
      GO TO 106
  111 IF(X) 117, 218, 117
  117 A = S1/(X*CX)
      CALL OVERFL(J)
      IF(J - 1) 219, 218, 219
  218 A = BIGNO
  219 RETURN
      END
$IBFTC SUB2
      SUBROUTINE SERIES(A, SX, CX)
      X = A
      IF(ABS(X) - .01) 50, 50, 60
   50 SX = .16666666 - .00833333*X
      CX = .5 - .04166666*X
      GO TO 40
   60 IF(X) 10, 10, 30
   10 E = SQRT(-X)
      SX = (SINH(E) - E)/E**3
      CX = (COSH(E) - 1.0)/(-X)
      GO TO 40
   30 E = SQRT(X)
      SX = (E - SIN(E))/E**3
      CX = (1.0 - COS(E))/X
   40 RETURN
      END
```

Fig. 13. Fortran IV program for FLIGHT subroutine

For $T > 104$ the initial guess calculated from the above formula is too large so x is taken to be 38.7.

d. Handling of extreme values of T. To ensure that the subroutine will not fail for large or small values of T, certain restrictions on T are built into the subroutine. The subroutine first calculates

$$T = \left(\frac{\mu}{s^3}\right)^{1/2} t_f \qquad (12)$$

and then replaces this value with the smaller of T and 950,000. It then replaces this value with the larger of T and 0.000001. This ensures that $0.000001 \leq T \leq 950{,}000$.

e. Restrictions on x. To ensure that the subroutine will converge with the above restrictions on T, restrictions are placed on the new estimate obtained from Newton's method. The restriction is that the new value of x must be greater than or equal to -823.0473 and less than or equal to 39.14553. These are the values of x that correspond to $T = 0.000001$ and $T = 950{,}000$, respectively.

f. Convergence. Convergence is achieved when the following condition is satisfied

$$|T(x_n) - T| < \frac{T}{100{,}000} \qquad (13)$$

g. Calculation of C(x) and S(x). Calculation of $C(x)$ and $S(x)$ using the Taylor series expansions was tried because of the simplicity of the series. In most cases, however, so many terms are needed from the Taylor series that it is much faster to evaluate $C(x)$ and $S(x)$ from formulas (1) and (2). The only difficulty with the latter approach is that the formulas for $C(x)$ and $S(x)$ both approach zero divided by zero as x approaches zero. To avoid this difficulty, $C(x)$ and $S(x)$ are calculated with the first two terms of their Taylor series for $|x| \leq 10^{-2}$ and from formulas (1) and (2) for $|x| > 10^{-2}$.

4. Performance

a. Accuracy. The subroutine is terminated when the given and computed flight time agree to five significant figures or more. The corresponding accuracy in the semimajor axis a is also five significant figures provided T is less than 950,000 and greater than 0.000001. If T is greater than 950,000, the semimajor axis a computed is the one corresponding to $T = 950{,}000$. If T is less than 0.000001, the semimajor axis computed is the one corresponding to $T = 0.000001$. In these two cases, five significant figures are obviously not obtained; however, these are such extreme cases that it is of little importance.

b. Speed. An average calculation takes 12 ms. This average was computed by doing 4000 cases with T ranging from 0.1 to 40. In this range the average number of iterations is three, including the initial guess. As T becomes smaller the number of iterations necessary for convergence increases to a maximum of 17 at $T = 0.000001$. As T becomes larger, the number of iterations increases to a maximum of 12 at $T = 28.8$, decreases again to four at $T = 7500$, and then increases again to eight at $T = 950{,}000$.

5. Conclusions

A subroutine LAMC was written to solve the flight-time problem. LAMC used the semimajor axis a as the independent variable, and used separate formulas for each of the special cases as discussed above. LAMC does more than solve for a, but if the extra calculations are removed, the length of the program is approximately 838 instructions. FLIGHT is written entirely in Fortran IV, but compiles into a program which is 609 instructions in length, including the calculation of $C(x)$ and $S(x)$.

The 4000 cases mentioned above took 48.4 s for FLIGHT and 64.2 s for LAMC.

Both LAMC and FLIGHT obtain five significant figures in all practical cases, but FLIGHT takes only three fourths as many locations as LAMC and runs in three fourths the time. The Fortran IV program is given in Fig. 13.

Reference

1. Battin, R. H., *Astronomical Guidance*, McGraw-Hill Book Co., Inc., New York, 1964.

D. Venus DSS Activities, *R. M. Gosline, J. D. Campbell, M. A. Gregg, R. B. Kolbly, and A. L. Price*

1. Experimentation

Use of the 30-ft antenna for moon-bounce clock synchronization transmissions at 8.45 GHz and for radiometric observations of the planet Venus at 23-GHz continues. Planetary radar operations were successful, using the new station control and monitor (SCAM) controller and 450-kW transmitter ranging on the planet Venus to within 100 μs.

Pulsar signals were tracked with the 85-ft antenna at 2388 MHz, and signals were processed with the SDS 930 computer.

2. System Performance

a. Receiving systems. All of the R&D receivers were made operational during this period. The Venus DSS Mod IV 2388-MHz receiver was used in both its monostatic and bistatic modes. Bistatic operation was accomplished by feeding the 455-kHz signal from a Mars DSS R&D receiver, via the microwave link, into the 455-kHz portion of the Venus DSS Mod IV receiver. Both of the Mars DSS R&D receivers (2388 and 2295 MHz) were utilized in the bistatic operation of various experiments. In addition, the 2295-MHz receiver was used in support of the Mars DSS operation in tracking the *Pioneer VII* spacecraft. This was necessitated by the modification and overhaul of station receivers. For this operation, the telemetry output of the R&D receiver was connected to the demodulating and recording equipment in the Mars DSS control room.

The Mod IV receiver is also being used in a pulsar experiment being conducted at 2388 MHz. For this use, the 30-MHz signal from the first converter was fed to an external detector and amplifier and then into the digital processing equipment.

b. Transmitting systems. The R&D 450-kW transmitter has operated 468.0 filament hours and 425.3 beam hours for scheduled missions on Venus planetary radar experiments and Mercury–Icarus tracking.

Several modifications have been made as a result of component failures. The mylar on the cone has been reduced from 5 mil to 3 mil thickness, the KN-6 tube has been replaced with a triggered spark gap, and a better silicone lubricant is being used on the high-voltage connectors.

The X-band transmitter has operated for 57 time sync experiments, for a total of 139.4 beam hours for this period.

3. System Improvements

a. Digital systems. An HP 5060A cesium frequency standard and HP 115BR frequency divider and digital clock have been installed to be used in conjunction with the moon-bounce clock-synchronization project. The SCAM controller has been installed and is operational, with the exception of some peripheral equipment and the fast coders.

b. Receiving systems. The Venus DSS *Mariner* receiver (2295 MHz) was removed from the ultra cone at the Mars DSS and reinstalled in the Venus DSS R&D cone. The R&D cone now contains two receivers, one at 2388 MHz and one at 2295 MHz. Except for the shared connection to the maser, each receiver has completely separate cabling.

c. Transmitting systems.

X-band. The power-supply heat-exchanger modification for the X-band transmitter has been completed, and the unit was installed on the motor generator pad. Other power supply work now in progress includes the installation and wiring of the filter choke and capacitor, high-voltage solid-state rectifier, shorting switch, and the series limiter.

500-kW feed cone assembly. An interim feed cone assembly for use with the Venus 85-ft antenna 500-kW transmitter at 2388 MHz was developed by modifying the existing R&D feed assembly. The task of developing the high-power 2388-MHz feed consisted of two major efforts: (1) development of proper cooling of the feed and associated components, and (2) installation of waveguide and switches suitable for high-power operation.

The problem of cooling a waveguide at 500 kW was approached from a theoretical standpoint; at 500 kW, losses in the oxygen-free high conductivity (OFHC) WR-430 waveguide account for approximately 450 W/ft. This power is nearly equally distributed over the surface of the waveguide. Four rectangular ⅝ × 1-in. cooling lines were installed along the guide.

The cooling of the feed assembly was accomplished by soldering 0.5-in. copper tubing to copper sheets and clamping it to the various sections of the feed.

The cooling of the turnstile probe has been reported in SPS 37-50, Vol. II, pp. 163–165. However, to ensure adequate conductance, it was necessary to machine a new probe 0.005 in. oversize and cool it to liquid nitrogen temperature for insertion into the turnstile junction. Special FXR high-powered switches were installed for the polarization and transmit/receive switch. This required modification of the existing mounting structure and installation of coolant lines for the switches.

A waveguide run to the transmitter room was assembled with cooling similar to that previously described. A coolant manifold was installed in the cone for the cooling of switches, feed assembly, and waveguide run. Extensive measurements were run on this feed cone, at both swept and selected spot frequencies. A summary of this data is found in Table 2.

Table 2. VSWR and isolation performance of 500-kW feed cone

Test area	VSWR	
	At 2388 MHz	At 2295 MHz
Transmitter port		
RCP	1.03	—
LCP	1.025	—
Receiver port		
RCP	1.035	1.25
LCP	1.099	—
Test termination		
LN$_2$	1.020	1.28
Ambient	1.020	1.28

1. Isolation between the LCP and the RCP ports was 34.8 dB at 2388 MHz.
2. There was no measurable degradation of the above parameters as a function of temperature from 80 to 140°F.
3. RCP = right-handed circular polarization; LCP = left-handed circular polarization.

Waveguide heat-dissipation tests. Heat dissipation measurements were made on WR-430 OFHC waveguide (with unfinished, white, and flat-black surfaces) operating at a high power level. The waveguide surface area was doubled by the addition of copper-cooling fins. The heat dissipation and improved efficiency were then measured. All tests were conducted with 31 kW of power circulating in the traveling wave resonator (ring) at 2.117 GHz.

A 24-in. section of an OFHC waveguide with JPL flat flanges was selected for testing. This section was placed in the ring, using two 3.5-in. sections as thermal isolators. Temperature instrumentation was provided to monitor E- and H-plane temperatures, as well as the temperatures of a section of the water-cooled ring. The ring was then powered to 31 kW. The temperature stabilized after approximately 40 min to 212°F. This was the reference high from which all improvements could be made.

Next, the section under test was painted white and stabilized after approximately 50 min of operation (at the same test power level of 31 kW) to 189°F. The section was then painted flat black. This provided much more heat dissipation and stabilized at a temperature of 172°F after approximately 25 min.

Straight sections of 0.75-in. U-shaped copper channel stock were then soft-soldered to the test section—four fins on E-plane and two on H-plane (Fig. 14). The test section contained a total area of 304.5 in.^{2}. After modification, the total area was increased to 676.5 in.^{2}. The next heat run provided a stabilized temperature of 180°F for the unpainted surface. Finally, after black MIL-L-71782 Sprayon was applied, an operating temperature of 156°F was achieved—the lowest recorded.

Apparently, the simple addition of flat black finish to an OFHC waveguide will allow it to operate around 40°F cooler if the ambient temperature remains the same. The addition of small cooling fins to the waveguide and flat

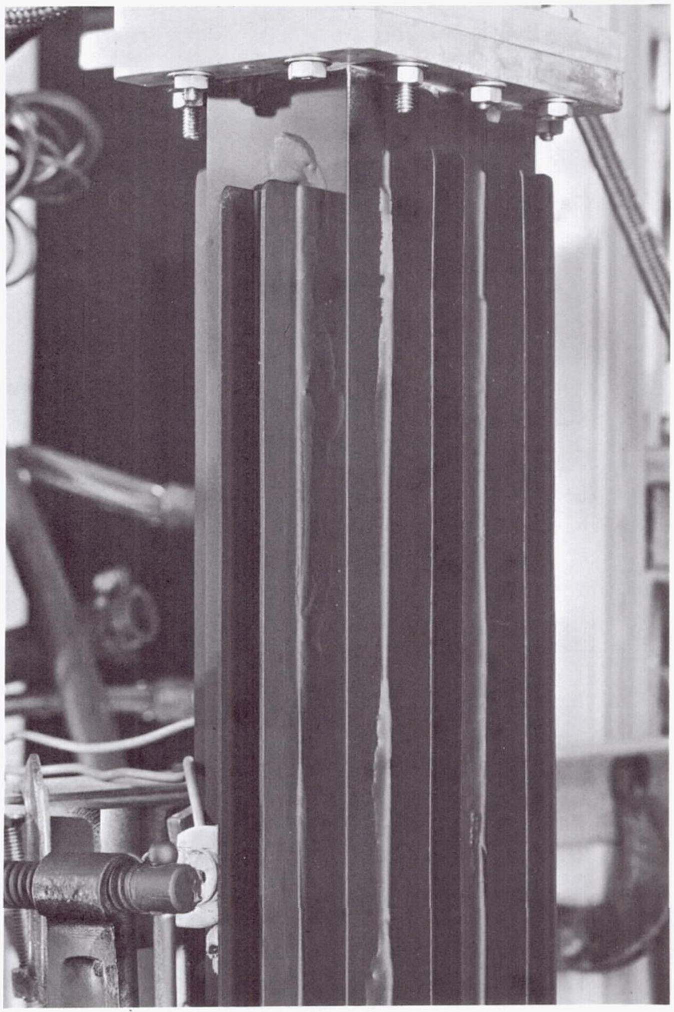

Fig. 14. Fin-cooled waveguide

black paint will lower the operating temperature approximately 56 deg from that of an unpainted waveguide. Long straight sections of transmit guide could be fabricated with cooling fins and painted flat black to eliminate the more costly liquid cooling in some installations.

E. Venus DSS 450-kW Transmitter, *E. J. Finnegan, B. W. Harness, and R. L. Leu*

1. Focus Magnet Power Supply, *E. J. Finnegan*

The 20-kW silicon-controlled rectifier (SCR) power supply described in SPS 37-43, Vol. III, and reported in SPS 37-45, Vol. III, has been uprated to 30 kW and is being used to operate the 450-kW klystron focus magnet. An RF filter was added to the power supply output in order to reduce the commutation transients from the SCRs in the system. A current regulator was added (Fig. 15) in order to maintain a constant current which, in turn, ensures a constant magnetic field on the klystron. The focus magnet is water-cooled and has a long thermal time constant; its resistance is a function of the coolant temperature and operating time. Thus, the focus magnet current varied with the temperature and length of time it was energized.

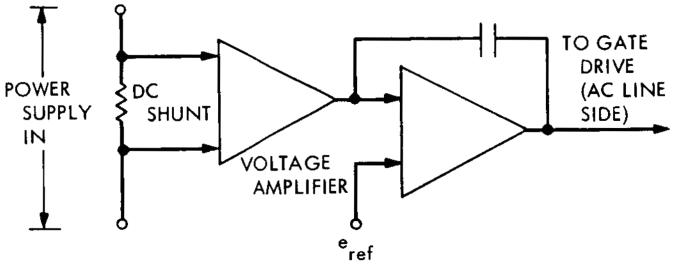

Fig. 15. Feedback amplifier

2. Ignitron Firing Circuits, *E. J. Finnegan*

The ignitron crowbar reported in SPS 37-43, Vol. III, has been installed at the Venus DSS and is working satisfactorily (Fig. 16).

The ignitron protects the klystron cathode and body from being destroyed, should the tube arc internally. This is accomplished in the following manner: If the tube should arc, a dc current sensor detects the high current transient in the line resulting from the arc and generates (in less than 1 μs) a train of pulses which triggers the photon trigger generator. The photon generator then radiates light energy to the high-voltage deck which triggers a light-activated SCR (LASCR). The LASCR generates a pulse to trigger a krytron gas tube which fires the ignition igniter, causing the ignitron to conduct and short-circuit the high-voltage power supply, thus interrupting and diverting the dangerously high current from the klystron. The design goal was to have this sequence of events take place in 10 μs, or less. Recent tests show it takes approximately 4 μs.

Figure 17 shows the igniter pulse circuit. The igniter requirement for fast, reliable firing is on the order of 2000 V (open circuit) and 200 A for 10 μs. A krytron, which is a small gas tube with a keep-alive voltage, was used first because of its compactness and short delay time.

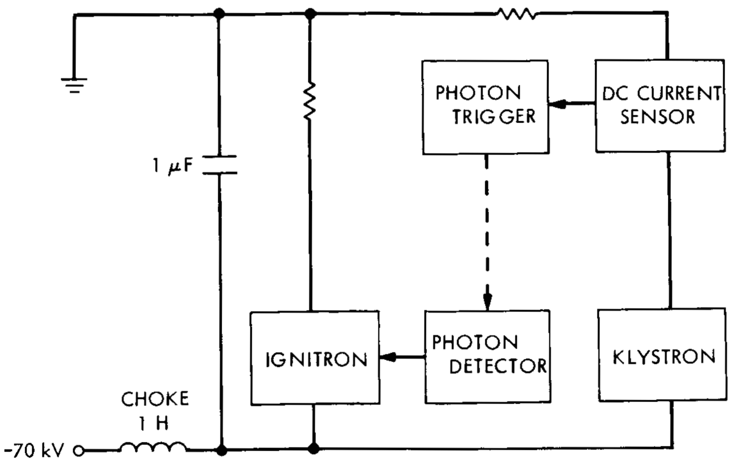

Fig. 16. Ignitron crowbar

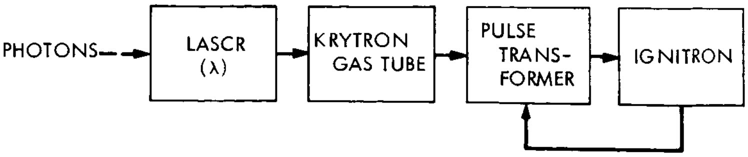

Fig. 17. Igniter pulse circuit

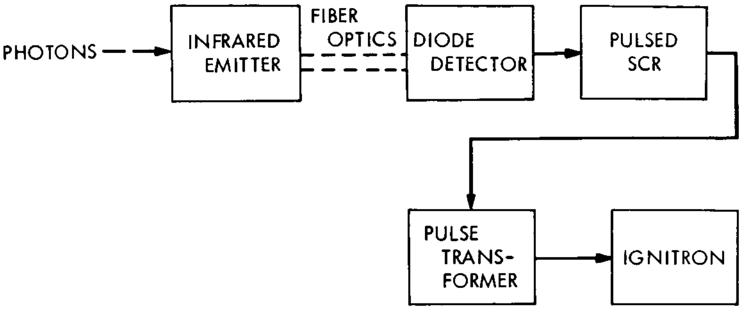

Fig. 18. SCR igniter circuit

However, the reliability proved to be very low, and it was removed from the circuit. The circuit was redesigned, using a triggered spark gap in place of the krytron.

A triggered spark gap is a gas-filled electron tube with a very high impedance when unfired and a near short when fired. A trigger transformer is used to inject a high-voltage pulse which causes the main gap to go into conduction. This supplies the high-energy pulse to the igniter.

Gallium arsenide infrared emitters (Fig. 18), in conjunction with fiber optics, are being investigated for future use. The xenon photon generator now in use has a long ionization time (2 to 3 μs). The gallium arsenide emitter would reduce the delay time to approximately 50 ns.

A circuit using an SCR (Fig. 18) for pulsing the igniter is also in the developmental stage. This requires a high pulse current (500- to 1000-A capacity) device; most of the high-current devices have long turn-on times (on the order of 2 to 7 ns). However, it may prove to have the greatest reliability.

3. RF Power Monitor, *B. W. Harness*

In order to perform an absolute power calibration for the 450-kW transmitter, it is necessary to discontinue tracking, move the antenna to zenith, and proceed to the electronics room where the measurement is made.

A remote water load flow and temperature-sensing system is being developed to accomplish an absolute power calibration at any time that it is possible to switch the transmitter into the water load.

The flow and temperature instrumentation will be accomplished by installing temperature sensors in the coolant inlet and outlet of the water load and by placing a turbine flow meter in the coolant outlet of the water load. A junction box in the antenna electronics room will contain two temperature bridges and an amplifier and will serve as a central cabling point for the sensors. The flow and delta temperature data will be transmitted by cable to the transmitter building where it will be possible to read the flow and temperature differential on digital voltmeters. The water load monitor panel in the transmitter control rack will also contain an analog computer to combine flow and temperature measurements and solve the equation

$$P = K\,(\Delta T)\,F$$

where

K = constant (0.264)

P = power, kW

ΔT = temperature differential, °C

F = flow of coolant, gal/min

The resultant output power will be indicated on a digital voltmeter. A simplified block diagram of the monitor system is shown in Fig. 19.

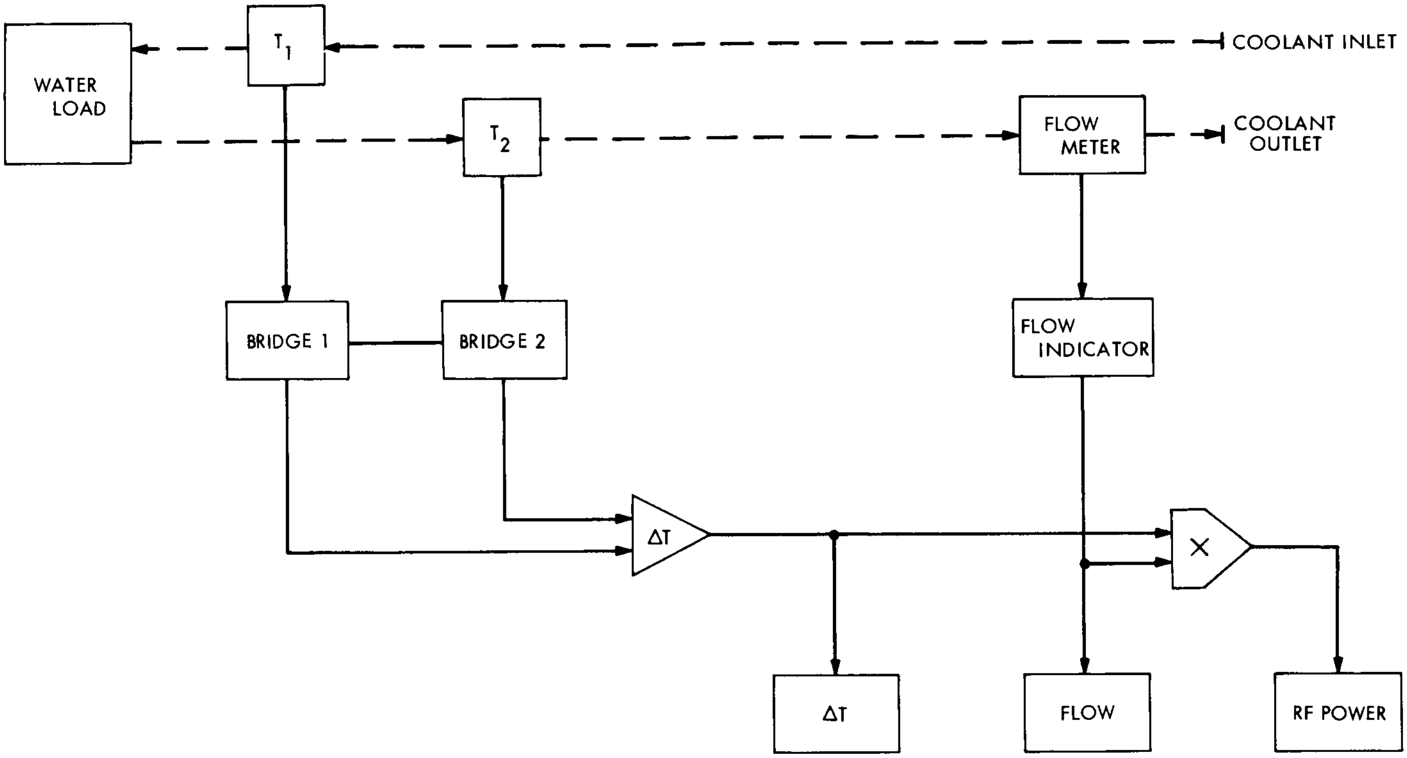

Fig. 19. Block diagram of water load power monitor system

4. Klystron Drive and Monitor Circuits, R. L. Leu

Variations in the RF power output of the 450-kW transmitter have been recorded during operation. Comparison of the RF monitored power with the calorimetric measurements of the waterload has established that the variations are in the RF drive and monitor circuit. Figure 20 is a block diagram of the existing RF drive and monitor circuit. Due to the variations and high insertion loss, a development contract is being negotiated to replace the existing circuits with stripline circuits.

Controlled environmental tests of coaxial components used in the RF drive circuit have shown large variations in insertion loss over a 0 to 60°C range. For testing purposes, only the components in the RF drive circuit were used, since identical components are used in the monitor circuits. Table 3 shows the individual loss variations of the components; however, the total variation of all the components (only one crystal switch) when tested as an assembly was 0.9 dB. Insertion loss variations of an equivalent RF drive circuit (two crystal switches and circulators) exceed 1 dB over the temperature range.

The components for the RF circuits at the present time are discrete units, interconnected by coaxial cables and connectors. As a result, the RF drive circuit has a minimum insertion loss of 6.0 dB and would require drive power across the 20-MHz klystron passband in excess of 40 W.

The new circuit will be comprised of two individual stripline circuits: one for the RF drive control and one for the RF power monitor. The RF drive circuit will include two fast-acting crystal switches (100-ns switching time) for protection of the klystron amplifier and will have a 2.0-dB maximum insertion loss with the variable attenuator at a minimum. Maximum variations of ±0.2 dB from 0 to 60°C and ±0.1 dB from +25 to 35°C are specified on all insertion losses and coupling coefficients in both circuits. The new units will be one fourth the size of the existing unit.

Extensive tests are to be performed on the prototype unit at the contractor's facility, and additional tests will be performed in the laboratory. The units will be installed in the R&D 450-kW transmitter at Venus DSS for final evaluation where they will be continually tested in an operating system.

Table 3. Insertion loss variations of coaxial components from 0 to 60°C

Component	Deviation, dB
Circulator	0.5
Crystal switch (1)	0.4
Variable attenuator	0.15
Coaxial switch	negative
Total	1.05
Circulator (1), crystal switch (1), variable attenuator, coaxial switch (as a unit)	0.9

The present plans are to use the stripline circuits in the Mark III transmitter at Mars DSS and reduce the drive requirements to 20 W across the klystron passband. The new stripline units will be compatible with the existing drive circuits in the DSN 10- and 20-kW transmitters and could be retrofitted into the transmitters.

F. High-Pressure Flow Switch Development,

G. P. Gale

1. Introduction

The azimuth rotation of the 210-ft advanced antenna systems (AAS) antenna is supported on three hydrostatic bearing pads which ride on a circular steel runner. Oil is pumped into cavities in the bottom of the pads and is forced to flow out from under the pads, forming a film of oil between the pads and the runner. The antenna then, in effect, floats or rotates on a thin film of oil. There are

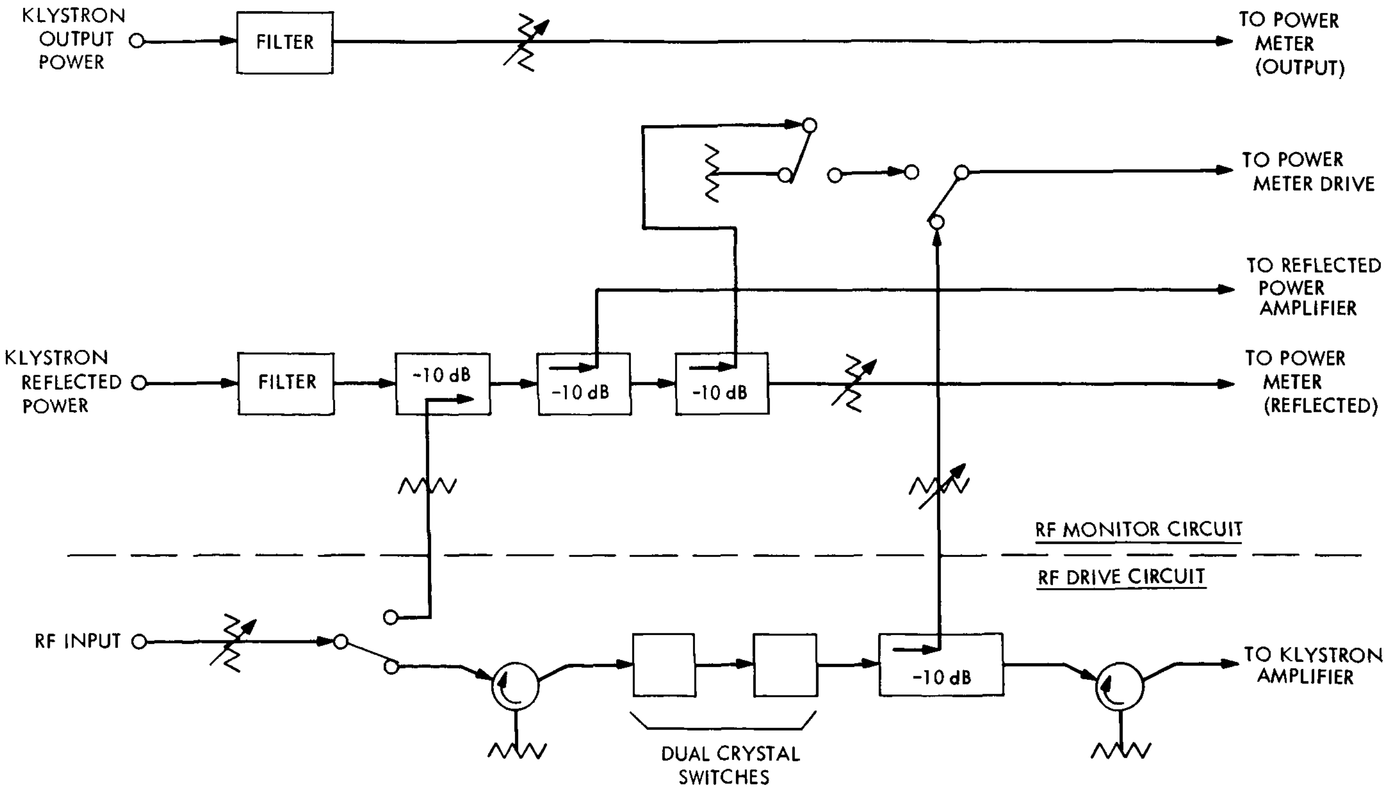

Fig. 20. RF drive and monitor circuit

six chambers in each pad through which the oil is pumped. Should the amount of oil pumped into any one of these chambers drop below a safe rate there may not be a sufficient quantity to maintain the oil film under the pad, and severe damage to either the pad or runner might occur. Therefore, flow-rate switches are used to sense any reduction in hydrostatic bearing oil flow below the minimum rate.

The nearly continuous use of these switches since the antenna was put into service has caused the valve seat portions of the switches to erode, and has reduced the repeatability of the switch-closing flow rate. The switches are constructed with a spring-loaded piston which is forced away from the valve seat when the oil flows. If the seat is damaged, the entire switch assembly must be replaced, because the seat is an integral part of the brass body and not easily repairable.

A market search has been made for a better replacement switch, and out of 64 sources only one switch was found that was in the pressure and flow rate ranges required by this service. This switch was almost identical to the switch currently in use. Consequently, a new switch was designed.

2. New Design

The new design requirements were that the switch: (1) be directly interchangeable with the old switch so that minimum time would be required for the changeover; (2) have replaceable seats and pistons so it could be serviced without total replacement; (3) have at least as good, if not better, performance than the original switch; and (4) have a longer service life expectancy.

A prototype has been built from the proposed design. A detailed description of the new design is found in Fig. 21. As noted in this figure, the switch functions as follows: Oil enters the flow switch housing through port ①. Part of the oil flows through the by-pass port ② and directly to the exit port ③. An adjustable plug ④ is used to limit or control the amount of oil which can escape by this by-pass route and, therefore, becomes a coarse range adjustment. A small part of the oil will flow through the by-pass capillary ⑤ located in the center of the end of the tapered spool ⑥ and then around the stem ⑦ which acts as the guide for the spool and also as a housing for the magnetically sensitive switch ⑧. This small flow of oil is provided to lubricate the guide for the spool, reducing the friction which could limit the repeatability of the switch action. A second function of the by-pass capillary is to create a restricted passage to damp out surges in oil flow rate which could cause erratic switching actions.

The rest of the oil has to flow through the annular space ⑨ between the tapered spool and the orifice. As the rate of flow is increased, the spool is forced out of the orifice. The distance the spool moves is proportional to the rate of flow. A spring ⑩ is used to resist the motion of the spool and to return it into position as the flow rate decreases. A ring magnet ⑪ pressed onto the spool is used to actuate the magnetically sensitive switch ⑧ when the spool is forced out of the orifice. Provision has been made in the housing ⑦ to locate several magnetic switches should multipoint flow-rate switching be required. A threaded adjustment ⑫ and lock nut ⑬ have been included on the housing to allow for positioning the magnetic switch closer to, or farther away from, the magnet on the spool, thereby providing an adjustment for the flow rate which will actuate the switch. The spool is tapered to increase the distance it will travel with respect to the rate of flow, thereby improving ability to precisely set the rate of flow at which the switching action will take place.

The orifice part ⑭ has been made separate from the main housing ⑮ to provide for easy replacement should the seat wear during use and to provide for the use of more wear-resistant materials for those parts which get abuse during operation. O-ring seals ⑯, ⑰, ⑱, and ⑲ have been used around the removable parts at all points where leaks might occur. The bypass ports ② in orifice part ⑭ are located symmetrically about the spool, and the oil flow around the spool is annular through space ⑨ and is symmetrical through the capillary passage ⑤ so that side forces which might cause the spool to bind or prevent it from moving freely are eliminated by this design.

3. Tests

The prototype switch was built using a brass housing, 416 stainless steel for the orifice, and 304 stainless steel for the spool. Preliminary tests were made on this switch using 5606 hydraulic fluid at approximately 80°F. The repeatability of the switch-closing flow rate for 10 trials was within 6.44 to 6.46 gal/min, and for 10 trials the switch opened within 2.05 to 2.10 gal/min. Even though the repeatability of the switching action was good, the wide spread between switch *open* to switch *closed* of 4.36 gal/min switching differential was not acceptable. Another problem was that in order for the switch to function, the bypass passage had to be almost completely closed.

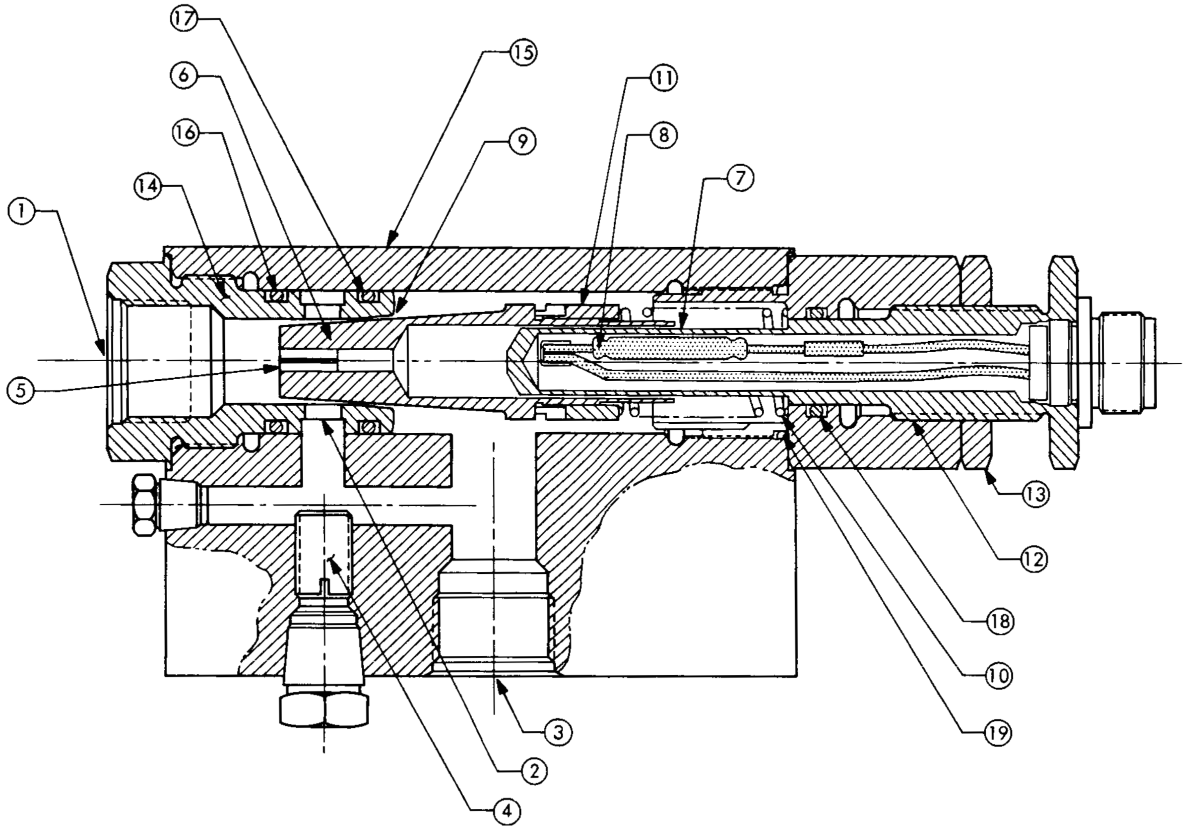

① INLET PORT
② BYPASS PORT
③ EXIT PORT
④ PLUG
⑤ BYPASS CAPILLARY
⑥ SPOOL
⑦ STEM
⑧ SWITCH
⑨ ANNULAR SPACE
⑩ SPRING
⑪ RING MAGNET
⑫ THREADED ADJUSTMENT
⑬ LOCK NUT
⑭ ORIFICE
⑮ MAIN HOUSING
⑯ ⑰ ⑱ ⑲ O-RING SEALS

Fig. 21. High-pressure flow switch

Because the switch was intended for use with an oil more viscous than the one used for the above test, subsequent tests were made on a system using R & O Eagle 20 oil. However, the flow-rate indicator was not precise, being an electronic indicator reading in percent of total flow and calibrated at two points of flow—50 and 100%. The precision of measurement was good to 0.25% only. With this oil, the bypass adjustment fell safely within its midrange and functioned as intended. However, the switching differential problem still existed. The switch closed at 48%, or 7 gpm, and opened at 31%, or 4.5 gpm; for a deadband of 2.5 gpm.

A plot of the spool position at time of switching action versus flow rate (Fig. 22) was made for several adjustments of the switch and indicates a surprising linearity. From these results it was decided to do two things: (1) reduce the amount of taper on the spool to increase its travel versus flow rate, and (2) to select a reed switch with a closer differential. The magnet position differential between switch *closed* to switch *open* for the reed switch first used was 0.085 in. A number of reed switches have been purchased which have a position differential of from 0.010 to 0.050 in. A switch was selected from this group with a position differential of 0.027 in. and was used for the next series of tests. The results of these tests indicate a flow differential between switch *open* to switch *closed* of 0.55 gal/min with the repeatability of switching action to be on the order of 0.01 gal/min.

4. Conclusion

Based on the results of these tests several prototype switches are being built, and after they have been thoroughly bench-tested, they will be installed in place of the existing switches for further test in the system.

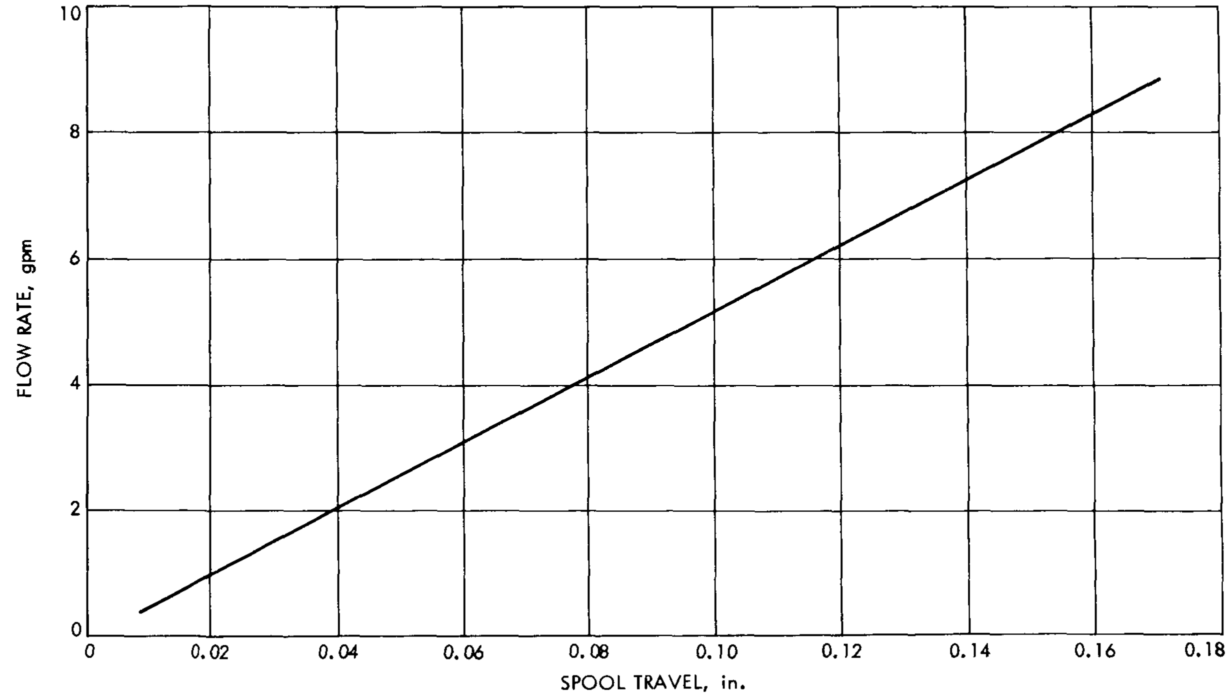

Fig. 22. Spool position versus flow rate

VI. Network Development and Operations

A. DSN Time-Synchronization Subsystem Performance, *H. W. Baugh*

A precision clock-synchronization network is being established to meet Deep Space Network (DSN) requirements. The immediate goal for this system is to synchronize all stations committed to *Mariner* Mars 1969 to within 20 μs, and provide correlation to the National Bureau of Standards (NBS) to within 5 μs for the DSN as a whole.

The system being used is described in SPS 37-43, Vol. III, pp. 92–106 and SPS 37-45, Vol. III, pp. 72–75. Some preliminary results of the field experiments are described in SPS 37-47, Vol. II, pp. 90–102 and SPS 37-50, Vol. II, p. 165.

Time-synchronization transmissions are continuing on a routine basis whenever the master station, Venus Deep Space Station (DSS), and the participating stations have a common view of the moon during their normal working periods. Schedules and predicts are sent to the receiving stations several weeks in advance and followed up with a weekly teletype message giving the anticipated transmission schedule for the next week. Participation by the NBS has been hampered due to a lack of personnel to commit to the operation on a formal basis. Both the Pioneer and Tidbinbilla DSSs handled time synchronization operations as routine duties until the Pioneer DSS was shut down for major station reconfiguration.

The principal objective of the receiving station at Pioneer DSS was to provide a check on the operation of the master station and the ephemeris. Since such a check is considered to be an essential part of the operation of the system, the time-synchronization antenna and receiver are to be moved to the Mars DSS late in August. Operations are scheduled to resume in early September.

The experimental time-synchronization system has been providing very consistent timing information. For example, Fig. 1 shows the results of time-synchronization measurements made on 16 out of the first 17 days of July, 1968. The data points were corrected for known adjustments of the Tidbinbilla DSS clock, and for the measured offsets at Venus DSS, so that the plot essentially shows the drift rate of the Tidbinbilla DSS Rubidium Frequency Standard with respect to the U.S. Naval Observatory (USNO). A straight-line fit to the data shows a slope of 6.61 μs/day, which is in good agreement with measurements made by very-low frequency (VLF) receiver and by comparisons with the Mount Stromlo Observatory.

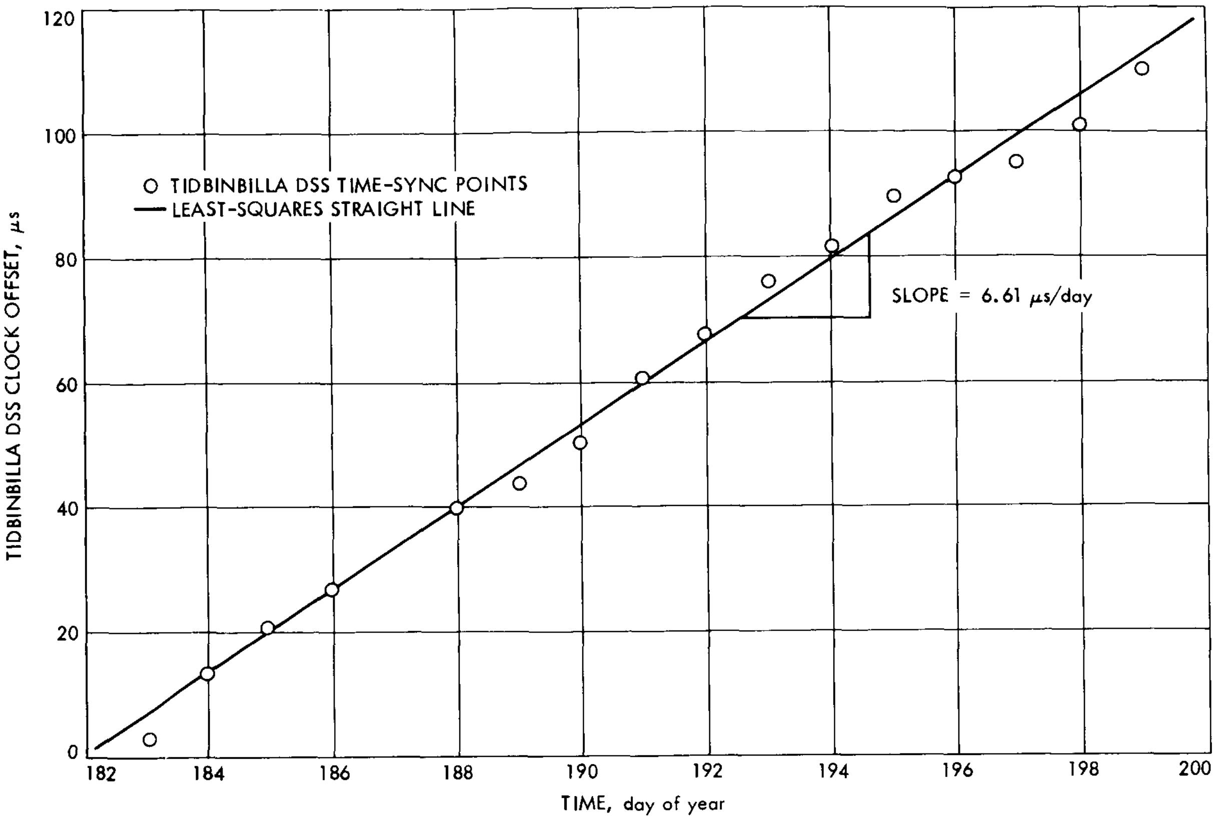

Fig. 1. Tidbinbilla DSS relative clock offset via moon-bounce time sync

The variations of the data from the straight line have a standard deviation of 2.54 μs, which corresponds very closely to the probable errors of the individual data points involved in each day's experiment.

The absolute accuracy of the system appears to be well within the desired limits, although a bias of approximately 10 μs has been noted. The most direct measurement of this bias has been by comparison of a 1 pulse/s "tick" sent by microwave from Pioneer DSS to Venus DSS. If microwave delays are constant, the delay between the Pioneer DSS time tick and the tick used in the time-synchronization system provides a continuous monitoring of the relative phases of the two clocks. The delay has been checked by means of a traveling clock visit to each station. The closure error of all these measurements is about 10 μs. Similarly, when a check was made at NBS (Boulder) by means of the traveling clock, the error closure was exactly 10 μs with the same sign.

The conclusion to be drawn is that there is either a 10-μs delay in the transmitter equipment (not otherwise accounted for), or in all three sets of receiver equipment. Both possibilities are equally likely since all of the coders are clocked by pulses at 10-μs intervals. This bias may be offset in the transmitter control program, just as ephemeris errors and other calibration errors may be handled, until the actual cause is found and corrected.

One source of instability in the system has been the Venus DSS clock, which is a relatively old unit pre-dating the frequency and timing subsystem (FTS) I. Steps are being taken to increase its stability, reliability and flexibility. An HP K02-5060A clock, using a cesium-beam frequency standard, has been installed and may be used immediately for setting the station clock just before a transmission. The next step will be to provide a countdown chain of Hi-Rel Modules to derive all essential timing signals from the cesium standard, and to provide a digital means for making fine adjustments in the phase of the clock signals. A final step will be to provide a full clock system based on FTS II designs so that the entire station may operate on cesium-based timing signals.

The performance of the cesium standard, to be known as MB-1, has been checked by the Goldstone Standards Laboratory. At the present time, the drift rate of MB-1 relative to NBS is on the order of 50 ns/week.

Present plans for converting the experimental system to an operational facility, other than the clock changes noted above, include the purchase of a second cesium clock to provide backup capability, and a very low frequency receiver that will permit independent checks to be made of the stability of the frequency standards used in the time-synchronization system. The network is to be expanded by the installation of time-synchronization receivers at the Woomera DSS, the Johannesburg DSS, one of the stations in Spain, and perhaps at the USNO.

VII. DSIF Development and Operations

A. Maximum Available Output Power for Transmitters, *R. C. Chernoff*

The transmitter subsystem installations at the Pioneer, Mars, Canberra and Robledo Deep Space Stations (DSSs) are rated at 20-kW RF output power. These transmitters all use the Model 5K70SG klystron as the final power amplifier. The manufacturer's test data for this klystron indicates that considerably more than 20 kW output can be attained at beam voltages higher than the normally specified 18 kV. For example, Fig. 1,[1] which is from the manufacturer's data sheet for this klystron type, shows that the power output at 21 kV is typically 30 kW. Since the maximum available beam voltage from the presently used transmitter power supply is between 21 and 22 kV, it is apparently feasible to operate the transmitter at or near the 30-kW output power level should spacecraft distance or characteristics require it. This feasibility was recently checked by operating the transmitter at the Mars DSS at 21.7 kV, the maximum power supply output voltage. The results and operating conditions are summarized in Table 1.

The experimental setup is shown in Fig. 2. It will be noted that the RF water load is situated at the end of a 15-ft (approximately) waveguide run after a harmonic filter and a waveguide switch so that calorimetric power

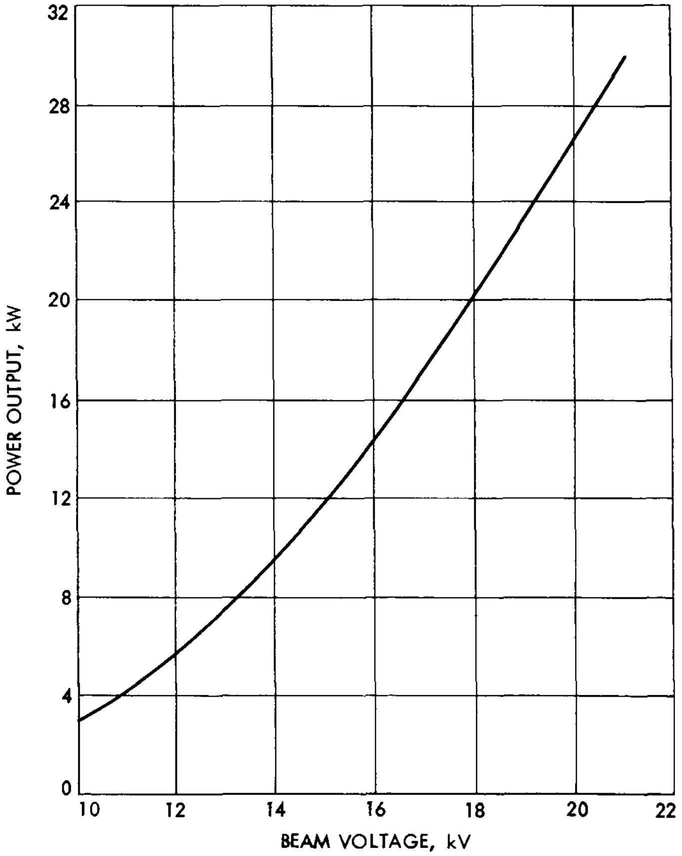

Fig. 1. Power output vs beam voltage

---

[1] Used here with the permission of Varian Associates.

Table 1. Klystron operating conditions

Function	Level
RF output power (calorimetric measurement)	31.5 kW
Frequency	2100 MHz
Beam voltage	21.7 kV
Beam current	2.85 A
Filament voltage	7.5 V
Filament current	11.0 A
Magnet current	17.6 A
Saturation drive power	180 mW
Saturated gain	52.4 dB
Collector dissipation	62 kW
Efficiency	51%
Saturated −1-dB bandwidth	20.1 MHz

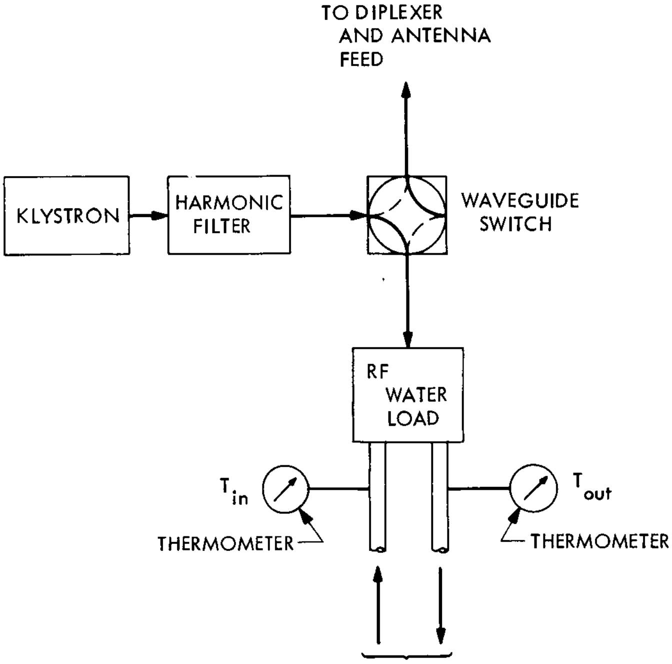

Fig. 2. Maximum transmitter output power measurement set-up

measurement is less than the klystron output by the insertion loss of the waveguide system between the klystron output flange and the load. This insertion loss was not measured, but it is expected to be less than 0.2 dB and greater than 0.1 dB. The output power referred to the klystron output flange is, therefore, greater than 32.2 kW and less than 33.0 kW.

The fluid used in the water load was a mixture of 24.5 wt % ethylene glycol and 75.5 wt % water. Specific heat and density of this mixture was found with the aid of Ref. 1 and used in calculating the RF power absorbed by the load. Since the VSWR of the load is less than 1.10:1.00, no correction for mismatch loss was necessary.

Reference

1. *Glycols.* Edited by G. O. Curme and F. Johnston. Reinhold Publishing Corp., New York, 1953.

B. Pulse-Gate Carrier Level Attenuation for Receiver Calibrations, *R. C. Bunce and A. C. Shallbetter*

1. Introduction

Low signal-level measurement, such as the received spacecraft incident-power level at the Deep Space Network (DSN) tracking stations, has been significantly improved in recent years by techniques such as the Y-factor method (Ref. 1). The major limitation of these techniques is in the accuracy of establishing relative carrier levels. For example, over 30% of the rms measurement error of received spacecraft power in the DSN is attributable to the relative level accuracy of the test transmitter signal used for obtaining the receiver signal-level calibration. This error, typically ±0.25 dB rms, is primarily associated with the test transmitter attenuator dial and is inherent in any dial-setting or mechanically-actuated attenuation process. Also, these adjustments are difficult to automate, and manual control is usually necessary in order to obtain even the aforementioned order of accuracy.

As a result, commercial amplitude modulators using voltage-controlled p-intrinsic-n (PIN) diodes modulators have recently been investigated by JPL (SPS 37-50, Vol. II, pp. 69–70). While these devices are easily automated (attenuation is a function of applied dc current), temperature and time-drift effects place them outside the desired accuracy range of calibrated attenuators; however, their accuracy and repeatability is improved when they are used as rapid-action on/off switches.

This characteristic suggested their use as a pulsed-gate to generate an amplitude-modulated carrier with an envelope consisting of square-pulses of variable width and repetition rate. If the pulse-form factor is constant from pulse to pulse, then the voltage amplitude of the carrier component of the modulated spectrum [as seen by the receiver automatic gain control (AGC) loop] is directly proportional to the duty cycle. Both the pulse width and pulse-repetition frequency (PRF) are functions of time and are resolvable to many orders of magnitude beyond other inherent error sources. The constancy of the pulse-form factor is related to the repeatability of the PIN modulator switching characteristic and the shape of the PIN modulator bias pulse, both of which have inherently low error potential. This lack of obvious sources of significant error led to an experimental verification of this method.

2. Pulse-Gate Attenuation Theory

The ideal waveform obtained by pulse-gate amplitude (absorption) modulation is shown in Fig. 3 and can be expressed as

$$E(t) = A_0 \cos \omega t + \sum_{n=1}^{\infty} A_n \left[\cos (\omega \pm 2\pi nf)t \pm \phi n\right] \qquad (1)$$

where

E = voltage

ω = carrier frequency (S-band), rad/s

f = the PRF, Hz

$= \frac{1}{T_1}$

ϕ_n = the nth sideband pair phase, rad

A_0 = the carrier component, V rms

$$= \left(E_1 \frac{T_2}{T_1} + E_2\right)\frac{1}{2^{1/2}}$$

$$\approx \frac{E_1}{2^{1/2}}\frac{T_2}{T_1} \qquad \text{if } E_2 \ll E_1 \frac{T_2}{T_1}$$

A_n = the nth sideband pair, V rms

$$\approx \frac{E_1}{2^{1/2}}\frac{T_2}{T_1}\left[\frac{\sin n\pi \frac{T_2}{T_1}}{n\pi \frac{T_2}{T_1}}\right] \qquad \text{if } E_2 \ll E_1 \frac{T_2}{T_1}$$

t = time

T = time period between pulses

T_2 = pulse duration (or width)

Assuming that E_2 is very small compared to the minimum value of $E_1 (T_2/T_1)$, the waveform leads to the "picket fence" spectrum, shown in Fig. 3, with the pulsed carrier component voltage level reduced to T_2/T_1 of its unmodulated value. The first sideband pair appears at a frequency interval equal to that of the PRF. When using the method as an AGC calibration procedure, restricting the PRF to values larger than the one-sided predetection filter bandwidth (approximately 1 kHz in the DSN receivers) results in only the carrier component appearing at the receiver AGC detector. Amplitude-pulsing, in effect, spreads out the carrier power bursts into a large number of discrete components with a sin x/x envelope. When the ratio T_2/T_1 is small, the first few sideband pairs are essentially equal in amplitude to the carrier component.

The modulated carrier component amplitude, A_0, is a function of the ratio of the pulse duration to the pulse

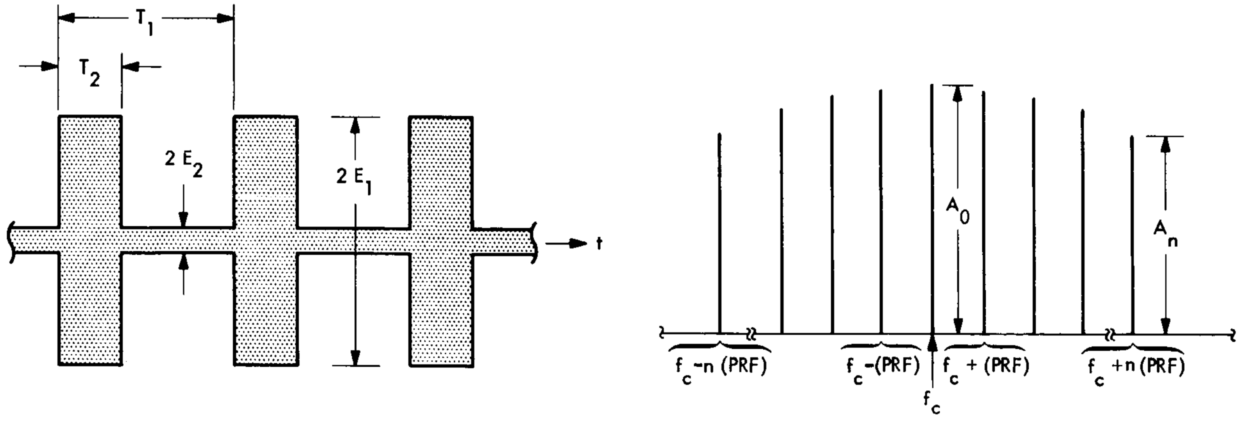

MODULATION ENVELOPE

CARRIER FREQUENCY (f_c) SPECTRUM

Fig. 3. Pulse-gate modulation waveform and spectrum

repetition time

$$A_0 = K \frac{T_2}{T_1}$$

or

$$A_0 = KT_2 \, (PRF) \tag{2}$$

The change in modulated carrier component amplitude, expressed as a ratio in decibels, is then

$$\Delta A_0(dB) = 20 \log \left(\frac{T_2}{T_{2_0}} \frac{PRF}{PRF_0} \right) \tag{3}$$

where

T_{2_0} = initial value of pulse duration time

PRF_0 = initial PRF

and if the pulse duration is maintained constant, then the change in carrier component amplitude is a function of the PRF

$$\Delta A_0(\mathrm{dB}) = 20 \log \left(\frac{PRF}{PRF_0} \right) \tag{4}$$

The initial, or reference, value of the modulated carrier component must be determined by an accurate method such as the Y-factor technique. The PRF and pulse width can then be selected to provide initial, or reference, values corresponding to this reference carrier level. Maintaining the pulse width fixed after obtaining the reference level, the carrier level can be expressed as

$$A_0(\mathrm{dBmW}) = A_{0_Y}(\mathrm{dBmW}) + \Delta A_0(\mathrm{dB}) + \epsilon_1(\mathrm{dB}) + \epsilon_2(\mathrm{dB}) \tag{5a}$$

$$= A_{0_Y}(\mathrm{dBmW}) + 20 \log \left(\frac{PRF}{PRF_0} \right) + \epsilon_1(\mathrm{dB}) + \epsilon_2(\mathrm{dB}) \tag{5b}$$

where

$A_{0_Y}(\mathrm{dBmW})$ = carrier component reference level determined by Y-factor method

$\epsilon_1(\mathrm{dB})$ = measurement errors in determining carrier reference level

$\epsilon_2(\mathrm{dB})$ = measurement errors in pulse modulation method of relative level adjustment

Measurement errors ϵ_1(dB) in determining the carrier reference level total 0.18 dB rms (Ref. 1).

Measurement errors ϵ_2(dB) are contributed by the inaccuracy of the PRF and the variations in the pulse waveshape. If the PRF is synthesized from the station standard, the only factor contributing to measurement error is the instability of the pulse waveshape. This instability is a function of both the pulse width and amplitude.

The effect of small variations in the pulse width can be determined by differentiating Eq. (5b) to obtain

$$\frac{d\,A_0(\mathrm{dBmW})}{d(T_2/T_{2_0})} = \frac{20}{\ln 10} \left(\frac{T_{2_0}}{T_2} \right) = 8.68 \frac{T_{2_0}}{T_2} \tag{6}$$

If the instability of the pulse width, T_2, is maintained to a value less than one part in 1000 (0.1%), the variation in the level of A_0 will be less than 0.01 dB.

The instability of the pulse amplitude, due to time and temperature drift, is a function of the bias level. These variations are minimized when the minimum attenuation bias is greater than +5 V. For the particular modulator under test, the variation of attenuation was less than ±0.002 dB for pulse amplitude variations of ±0.1 V. The temperature coefficient at approximately room temperature for the unmodified PIN modulator was found to be nearly 0.02 dB/°C; therefore, for practical applications, some temperature compensation or ambient temperature control is necessary. However, a special version of the modulator using passivated diodes has recently been developed. Temperature effects with this item are not as great, although a full evaluation of the improved type has not yet been conducted. The preliminary manufacturer's specification is 0.002 dB/°C at minimum attenuation.

3. Experimental Results

In order to establish the accuracy of the pulse-gate carrier level attenuation method, the laboratory receiver/exciter subsystem configuration was modified to act as a precision narrow-band carrier level reference (Fig. 4). A precision attenuator was inserted, together with external impedance stabilization, in the 50-MHz IF path as a level-increment standard. Receiver gain was adjusted manually during phase-lock to provide a reference level at the correlation amplitude detector output of 1.0000 V dc. A low-pass resistance–capacitance filter was placed at the output of the detector to reduce the noise level at

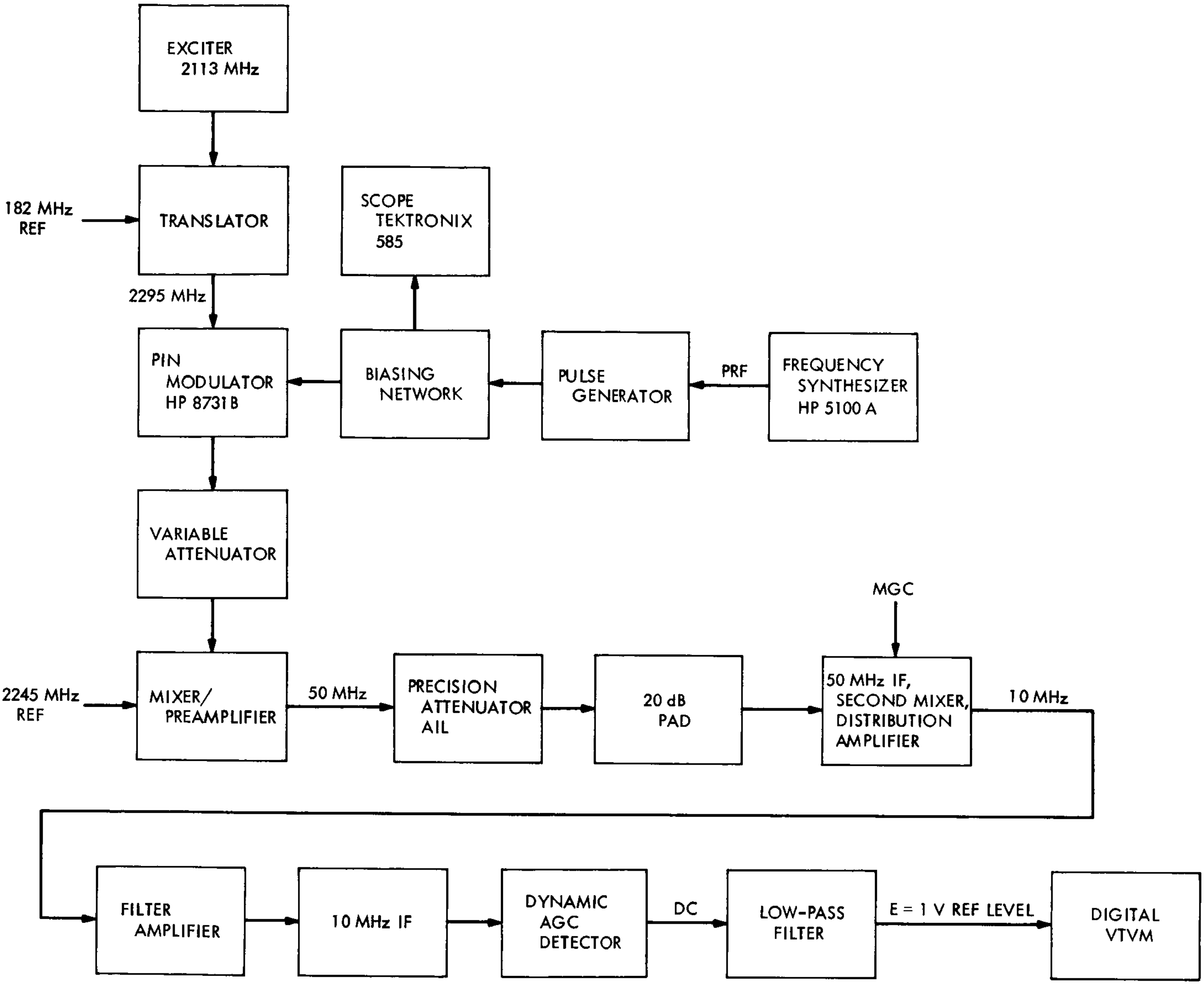

Fig. 4. PIN modulator test set-up

the digital vacuum-tube voltmeter (VTVM) input. A commercial pulse generator was triggered by a synthesizer, and the resulting pulse was applied to the bias input of the modulator.

During the run, the pulse-width in the switching region was held constant at 1.0 μs, within 0.1%, by careful adjustment of the pulse generator. The digital VTVM 1-s counts were noise variable, typically, over a range of 0.2–0.3 mV. Both of these instabilities represent a maximum measurement error of ±0.01 dB.

The carrier (peak pulse amplitude) at the receiver input was adjusted with the translator attenuator for about −100 dBmW. The noise power, referred to the mixer/preamplifier bandwidth, is about −104 dBmW. The signal-to-noise ratio (SNR) during carrier-on periods was thus at a nominal value of 4 dB within the subassembly. This is sufficiently low to avoid receiver saturation effects on the pulsed carrier. Peak power output from the mixer was about −50 dBmW. The minimum attenuation used during the run between the mixer output and the 50-MHz IF amplifier input was 50 dB, resulting in a maximum peak-carrier level of −100 dBmW at the IF strip input. The low SNR assured that the IF amplifier and following distribution amplifier, even at maximum gain (about 50 dB), would not be operating closer than 30 dB to the nonlinear region during pulse peaks.

A slight rounding of the modulated waveform at the distribution amplifier output results as an effect of the passband to this point (about 9 MHz minimum). The averaging effect of the predetection filter produces a steady carrier when the PRF is greater than the one-sided predetection filter bandwidth.

During the qualification run, the detector output voltage, E, was used as the monitoring voltage. The PRF was varied over an equivalent 30-dB range in 1-dB steps. The precision attenuator was simultaneously adjusted in 1-dB increments. The accompanying value of E was recorded, and its variation from the reference value at PRF_0 was computed. This variation, ϵ, was statistically averaged and found to have an rms value of 0.017 dB. Since this variation is on the same order of magnitude as that of the precision attenuator and oscilloscope waveform monitor, it is apparent that, under the controlled circumstances described, the pulse-gate modulation technique did not produce errors distinguishable from expected errors inherent in the measuring equipment.

The results of the run, with data expressed in decibels, are shown in Fig. 5. The noise variation on the detected output became too large for accurate sampling beyond the 30-dB test range.

The pulse-gate carrier level attenuator method was then applied to generate an AGC curve using the Y-factor technique to establish a reference. A calibrated Y-factor detector (developed at JPL) was connected to the laboratory receiver noise-figure output. The noise power, referenced to the receiver input in the detector bandwidth, was calculated at −124.20 dBmW using the receiver-measured noise figure of 10.2 dB. The pulsed carrier was then generated and fed into the receiver input through the translator attenuator. The PRF was adjusted to 194.962 kHz and the translator attenuator varied until the noise figure detector indicated a 3-dB increase (SNR = 1). This established a reference of −124.20 dBmW for a PRF of 194.962 kHz; the frequency was chosen to provide a convenient scale referenced to PRF of 100.000 kHz for −130 dBmW [20 log(194.962/100.000) = 5.80 dB]. The PRF was then adjusted to vary the carrier level from −120 to −151 dBmW. The results are shown in Table 2 and Fig. 6.

4. Conclusions

Pulse-gate carrier level attenuation gives promise of providing essentially error-free effective carrier level increments for narrow-band microwave receiver calibration purposes. The method has been verified over a 30-dB range and is usable beyond this range as long as the

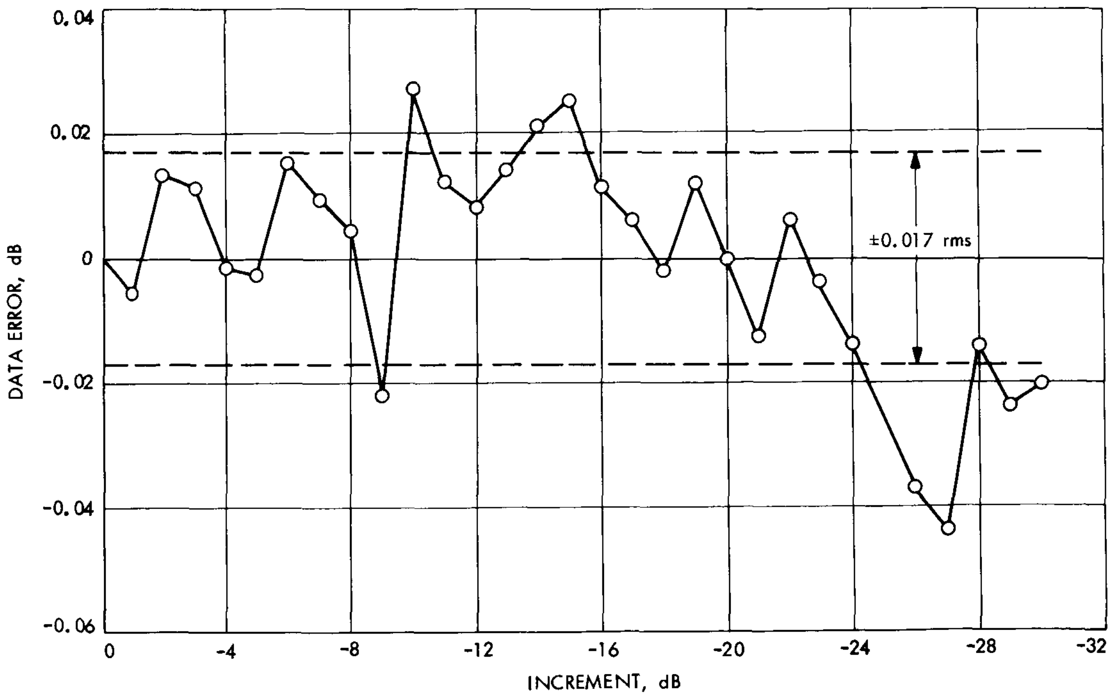

Fig. 5. Pulse-gate carrier level attenuation qualification run data

Table 2. AGC curve test data

Frequency, Hz	Level, dBmW	AGC, V
316,230.0	−120.0	−6.03
194,962.0	−124.2	−5.71
177,830.0	−125.0	−5.64
100,000.0	−130.0	−5.20
56,233.0	−135.0	−4.71
31,623.0	−140.0	−4.16
17,783.0	−145.0	−3.54
12,589.0	−148.0	−3.08
10,000.0	−150.0	−2.70
8,912.5	−151.0	−2.40

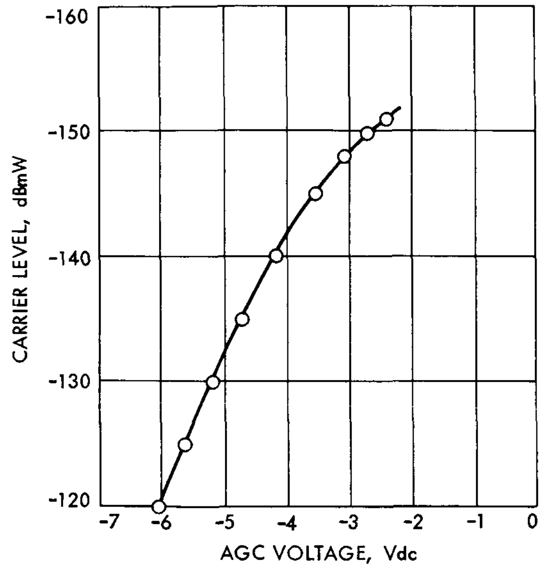

Fig. 6. AGC curve

carrier peak power (during pulse-on periods) remains well below receiver saturation. The application is bounded by the following considerations:

(1) For greatest accuracy, the absolute (unmodulated) carrier level and duty cycle should be selected so that the receiver operates in its linear range.

(2) The minimum PRF should be greater than the one-sided bandwidth of the receiver predetection filter.

(3) The accuracy of the method is a direct function of the stability of the pulse waveshape.

(4) The method probably cannot be used, except as a transferable reference, when test conditions normally require a wideband-modulated continuous-wave carrier.

Reference

1. Stelzried, C. T., Reid, M. S., and Nixon, D. L., *Precision Power Measurements of Spacecraft CW Signal With Microwave Noise Standards*, Technical Report 32-1066. Jet Propulsion Laboratory, Pasadena, Calif., Feb. 15, 1968.

C. Wideband Phase Detector for the RER and SDA Subsystems, *C. E. Johns*

1. Introduction

The present S-band receiver–exciter ranging (RER) and subcarrier demodulator assembly (SDA) subsystems use phase-sensitive detectors throughout. Their operating frequencies extend from 100 kHz to 22 MHz, depending on their particular use and location within the subsystem. As improved or new subsystems are being developed, the phase detector performance requirements become more stringent.

To meet the need for improved performance, a wideband detector has been developed that will operate at any of the frequencies presently used, or planned for near-future use, in RER and SDA subsystems.

The design features of the phase detector are as follows:

(1) Wide operating frequency range to allow phase detector use at any input frequency between 50 kHz and 25 MHz.

(2) Wide input-to-output signal bandwidth (dc to 1.3 MHz at the −1-dB point) for use in the receiver telemetry channel and as the data detector in the SDA.

(3) Low unbalance voltages, at the output terminal, caused by incoming noise, reference drive level variations, or temperature changes, (±3-mV maximum).

(4) Small amount of signal phase shifts caused by high noise levels at the signal-input terminal or temperature changes (2 deg maximum).

(5) Ease of alignment and test.

2. Circuit Description

A schematic diagram of the detector is shown in Fig. 7. To obtain the wide operating frequency range, untuned

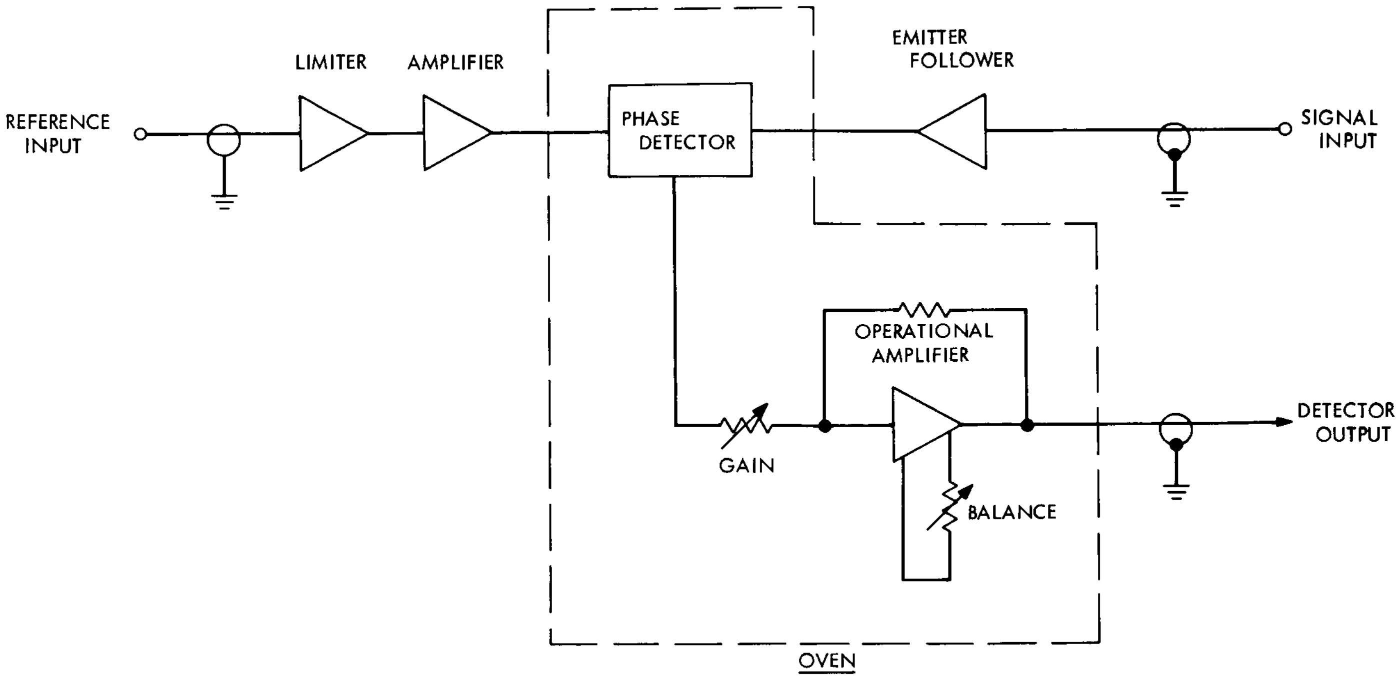

Fig. 7. Wideband phase detector block diagram

amplifiers are used for the signal amplifier and reference limiter–amplifier. The signal amplifier consists of a linear emitter–follower with a frequency response that is constant to within 1 dB from 50 kHz to 30 MHz. When the detector is to be used within a phase-locked loop, limiting for the signal input is accomplished within the preceding IF amplifier. The reference limiter–amplifier operates over the same range with very little change in electrical characteristics.

The phase-sensing portion of the detector is a commercially available double-balanced mixer suitable for printed circuit applications. It contains wideband input transformers (50 kHz to 200 MHz) and four matched diodes. The output port of the mixer is untuned and has a flat response from dc to 200 MHz.

Because of the mixer's relatively low output voltage capability (200-mV peak), it is followed by a stable, wideband commercial operational amplifier. The amplifier's gain is adjusted for a 5-V peak signal output voltage across a 1000-Ω load. The 1000-Ω load impedance was selected to make the detector compatible with present SDA requirements. The 5-V peak signal output is obtained with an input signal of +8 dBmW. The detector, however, maintains a linearity of 4 to 6 dB above this level.

The no-signal (reference input only) balancing of the circuit is accomplished by adjustment of a single potentiometer connected to the amplifier offset adjustment terminal that allows zeroing the normal amplifier offset voltage and, simultaneously, the inherent unbalance voltage at the mixer output. Therefore, the complete alignment of the detector (gain and balance) is accomplished by two potentiometer adjustments.

To reduce the dc unbalance due to temperature variations, the mixer and operational amplifier are installed in a commercial oven that maintains a constant 65°C internal temperature. The signal amplifier and reference limiter–amplifier are located external to the oven. A single thermistor is used in the reference amplifier stage to compensate for the characteristics of the silicon diodes used in the limiter stage and to maintain a relatively constant reference signal level to the bridge. The limiter–amplifier output level varies less than 0.2 dB over the temperature range of 0 to 50°C. The limiting level also remains within ±0.2 dB for reference input level variations of +7 to +10 dBmW.

3. Performance

Figure 8 is the frequency response between the signal input and output terminals. To obtain this response, the reference frequency was held at a constant 10 MHz and the signal varied above and below the reference frequency. The output signal is the resulting difference

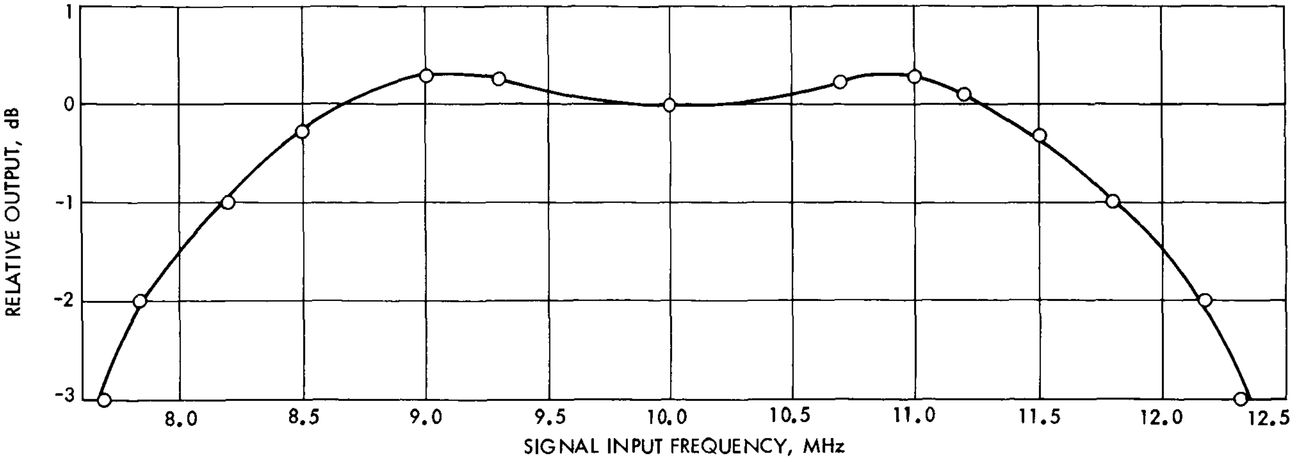

Fig. 8. Phase detector signal frequency response

between signal and reference. As shown, the −1-dB bandwidth exceeds the original design criterion of 1.3 MHz.

The reference (no signal) unbalance voltage, measured over the temperature range of 0–50°C, was less than ±0.6 mV. In addition, the reference input level was varied between +7 and +13 dBmW at each test temperature, and the total unbalance was less than ±1 mV.

Signal phase shift with large noise-to-signal ratios was measured in noise bandwidths of 100, 500, 4500, and 45,000 Hz and 3 MHz. In each bandwidth, the noise level was adjusted to 2 dBmW and the signal to −29 dBmW. The reference phase was varied in 5-deg increments to allow plotting the zero voltage crossing at the detector output. The plots were then compared to a no-noise plot to determine the phase shift. The worst case phase shift in any noise bandwidth was less than 1 deg.

Also, the no-signal noise unbalance (noise bias) was measured in each bandwidth, with a noise level of +2 dBmW. The maximum unbalance was 0.5 mV in the 100- and 500-Hz bandwidths.

As a comparison of performance, let the ratio of the detector peak output voltage, V_p, to the total unbalance voltage, V_u, be the detector figure of merit, FM, i.e.

$$FM = \frac{V_p}{V_u}$$

The present 10-MHz detectors used within the RER have a peak output voltage capability of 30 V and a total specified maximum output unbalance voltage (due to temperature, reference level variations, etc.) of 225 mV. Then

$$FM = \frac{30}{0.225} = 133$$

and

$$FM\,(\text{dB}) = 50\,\text{dB}$$

The present wideband detector used within the SDA has a 5-V output capability and a specified maximum unbalance of 10 mV. Then

$$FM = \frac{5}{0.010} = 500$$

and

$$FM\,(\text{dB}) = 54\,\text{dB}$$

The new detector has a V_p of 5 V and a V_u of 3 mV maximum. Then

$$FM = \frac{5}{0.003} = 1663$$

and

$$FM\,(\text{dB}) \approx 64\,\text{dB}$$

The improved FM allows the detector to operate without degradation of performance, with a signal-to-noise ratio 10 dB greater than the type presently used within the SDA.

4. Conclusion

The new detector performs well within the established design criteria. Its electrical performance excels any of the detectors used within the present RER or SDA subsystems and, because of its wideband RF input, it can be used for several applications in future systems.

D. DSS Control and Data Equipment, *E. Bann, A. Burke, J. Woo, D. Hersey, and P. Harrison*

1. Antenna Pointing Subsystem, Phase I

The antenna pointing subsystem, phase I (APS I) is being implemented in the deep space stations (DSS) for the purpose of providing computer control over the antenna servo subsystem. The APS I provides improved spacecraft acquisition capability through an on-line computed ephemeris or a precomputed drive tape. A more detailed description of the APS I characteristics has been given in SPS 37-38, Vol. III, pp. 74–76.

Installation of APS I equipment at the Echo, Woomera, Canberra, Johannesburg, Robledo, and Cebreros DSSs will be completed by October 1968.

2. Telemetry and Command Processor, Phase II

The telemetry and command processor (TCP) is currently being updated to the phase IIC configuration, as part of the multiple mission telemetry system (MMTS). The updating, discussed in SPS 37-46, Vol. III, pp. 230–234, consists of expanding the core memory of the SDS 920 computers in the TCP to 16,000 words and the addition of analog racks containing multiplexers, analog-to-digital converters, and special interface equipment.

The installation and checkout of the TCP IIC equipment has been completed at the Echo, Woomera, Johannesburg, Cebreros, Cape Kennedy DSSs, and Configuration testing area (CTA) 21. Installation at the Mars DSS will begin in early September 1968. Installation at the Canberra and Robledo DSSs is scheduled to begin in December 1968.

High-speed data modification kits for TCP communications buffers, to maintain compatibility with the NASCOM error encoder–decoder equipment, have been distributed to the overseas stations and have been installed and checked out at Echo DSS and CTA 21.

3. Station Control and Monitor Console, Phase II

The station monitor and control consoles (SMCC) at the Echo, Mars, Woomera, Johannesburg, Cebreros, and Cape Kennedy DSSs are to be upgraded to the Phase II configuration. This upgrading is to be accomplished by several modifications, the first of which is the incorporation of the program alarm and control panel and cabling for the X-Y recorder. For a description of the program alarm and control panel and associated units, see SPS 37-51, Vol. II, pp. 123–126.

The program alarm and control panels, and the associated power supplies and digital circuitry, have been completed for five stations. Based upon the current delivery schedules for the cables, the installation and checkout of the modification at the Echo DSS, and shipment of the kits to the Woomera, Johannesburg, Cebreros, and Cape Kennedy DSSs will be accomplished by the end of August 1968.

4. Frequency and Timing Subsystem

The production of those equipments required to convert the frequency and timing subsystem (FTS) from phase I to phase II configuration is under way for five stations. The subsystems are presently scheduled to be installed at the stations during September and October 1968.

E. DSS Reconfigurations, *E. Thom, T. Burns, R. Latham, and R. Weber*

1. Introduction

During the period of April–August 1968, the deep space stations (DSSs) committed to the *Mariner* Mars 1969 project (Echo, Woomera, Johannesburg, Robledo, and Cape Kennedy DSSs) have undergone a reconfiguration in preparation for that project. The reconfiguration consisted of block upgrades of several subsystems, a rearrangement of the control and communications rooms to provide space for several new cabinets of equipment and improve operator and maintenance efficiency, and the performance of major maintenance to some of the older equipments. The work performed on each subsystem is described in this article.

2. Receiver-Exciter

The phase I or phase II receiver–exciter at each station was upgraded to phase IIIC. This change consists of replacing various modules to provide a much more versatile frequency selection capability. In addition, each station received a complement of subcarrier demodulator assemblies and a test equipment assembly. This equipment provides the coherent subcarrier detection capability necessary for the multiple-mission telemetry system (MMTS) committed to *Mariner* Mars 1969.

3. Transmitter

The transmitter power supplies at the Echo, Woomera, and Johannesburg DSSs received major maintenance.

4. Digital Instrumentation Subsystem

The phase I digital instrumentation subsystem (DIS) at each station was upgraded to phase II. This consisted of removing the SDS 910 computer, expanding the core memory of the SDS 920 from 8,000 to 16,000 words, and adding several peripheral devices such as a line printer and remote typewriter.

5. Antennas

The antenna structures at the Echo and Woomera DSSs were strengthened by the addition of members, replacement of members with others having stronger sections, and by changing the bolt pattern and type of bolts at the joints. The drive skids were altered to provide increased polar wheel travel, the servo pump was replaced with a larger unit, and the servo electronics were modified to provide better response control and greater monitor capability. The Johannesburg DSS antenna underwent rebolting, realignment, surface resetting, drive skid and gear segment resetting, and a new cable wrapup installation.

6. Station Monitor and Control Console

The station monitor and control console (SMCC) at each station was upgraded from phase I to phase II to provide additional display equipment consistent with the increased capability of the DIS II to provide performance monitor information.

7. Telemetry and Command Processor

The telemetry and command processor (TCP) computer at each station was upgraded to the phase IIC configuration by the addition of two interface racks containing analog-to-digital converters and by expansion of the core memory to 16,000 words.

8. Frequency and Timing Subsystem

The frequency and timing subsystem (FTS) at each station will be upgraded to phase II as soon as the modification kits become available. This will include the X-band time synchronization.

9. Antenna Pointing Subsystem

The SDS 910 computer (removed from the phase I DIS) and an interface cabinet were added to each station (except the Cape Kennedy DSS) to provide an independent antenna pointing subsystem (APS).

10. Communications

Each station's communications equipment has been consolidated into a separate communications room and arranged in a Goldstone duplicate-standard (GSDS) configuration. The communications control group, new high-speed data modems, block multiplexer, and communications junction module have been supplied to all stations; the DSIF/GCF interface (DGI) computer will be supplied to the Echo, Woomera, Johannesburg, and Robledo DSSs when available.

11. Control Room Arrangements

The control rooms at each station were reconfigured both to group equipment functions and types together, in order to permit greater operator and maintenance efficiency, and to provide floor space for the new equipments. Considerable planning was done to allow for anticipated future changes and growth.

12. Johannesburg DSS Unique Changes

Unlike the other stations in the DSIF, the Johannesburg DSS was a non-GSDS station in that it did not have the ranging, SMCC, and TCP. Also, some of its equipment [i.e., tactical intercom, FTS, tracking data handling (TDH), analog instrumentation, and antenna servo] had been installed during the station's L and L/S-band era and was inadequate for *Mariner* Mars 1969 support.

The station's communication system used Siemens teletype equipment which was not capable of handling the new 100 words/min rate. As a result of these anomalies, the station underwent an extensive reconfiguration program to (1) install the new equipment, (2) replace the obsolete equipment with standard equipment, and (3) replace the Siemens teletype equipment with Teletype Corp. equipment. In addition, the antenna structure was overhauled, which involved skid rework, resurfacing of the dish, rebolting, installation of the cable wrapups, and replacement of the hydraulic pumps.

Equipment planned for the station, but not yet available for installation, include the DGI computer, the updated version of the FTS, and the X-band timing equipment. The DGI should be installed by November 1968, the X-band timing equipment by February 1969, and the FTS II late in 1968. With these exceptions, the station should now be considered a standard station.

13. Cape Kennedy DSS Unique Changes

Experience has shown that past methods of DSIF/spacecraft compatibility testing at the Cape Kennedy DSS have been very time consuming and expensive and have produced results not completely consistent with all the various requirements. As a result of this experience, computer programs and necessary hardware have been developed to allow future compatibility testing to be performed by computer methods.

a. Computer programs

Ranging Delay. Measures ranging delay and removes a previously measured zero delay to provide a spacecraft delay.

Ranging Threshold. Permits printout of ranging data associated with ranging threshold. The ranging downlink carrier loop threshold is run automatically.

Tracking Rates and Acquisition. Provides uplink frequency control to test tracking rates and acquisition frequencies. It also performs best-lock measurements at signal levels controlled at the SMC.

Spectrum Analysis. Plots the RF spectrum and spurious signals in graphic form on the DIS line printer.

Uplink Threshold. Prints command threshold information as the uplink signal level is changed from the SMC and performs uplink RF threshold measurements.

Dynamic Test. Computes parameters for a circular earth orbit and utilizes them to control uplink–downlink signal levels and frequencies.

Phase Jitter. Samples analog data, which is then converted to rms degrees and compared to a previously entered constant.

Downlink Test. Prints telemetry threshold data as the downlink signal level is decreased from the SMC, and determines the downlink RF threshold by decreasing the downlink signal level until receiver 1 automatic gain control (AGC) voltage goes positive.

b. Hardware additions

Parallel-input (PIN) modulators. PIN modulators have been installed in the microwave subsystem and the exciter output. These modulators are used as remote-controlled attenuators and provide the capability to control the transmitted and received signal levels. Control of these modulators is accomplished either manually or by the computer digital-to-analog converter.

SMC control panel. A control panel added to the SMC is used to control the SMC frequency display with a binary-coded decimal-type degi-switch and clear button and to control the PIN modulators. This is done with four degi-switches; three of these degi-switches allow a decibel change of up to 99.9 dB, and one controls the rate of change from 0.1–0.9 dB/s. The control panel also has provisions for a plus or minus direction of change and selection of uplink and downlink receiver 1 and downlink receiver 2 signal levels.

SMC frequency display. A unit has been added to the SMC to display the following S-band frequency information: (1) receivers 1 and 2 VCO frequency, downlink frequency, and signal level, (2) predicted exciter VCO frequency from receiver 1 VCO, (3) transmitter uplink frequency, and (4) up-link and downlink PIN modulator attenuation.

Ranging. As there is no TDH subsystem at the Cape Kennedy DSS, a special cable was fabricated to provide the ranging data input to the DIS. The 0- and 90-deg ranging clock doppler outputs were connected to spare isolation amplifiers and the outputs routed through the system junction module to the DIS analog-to-digital converter inputs. Also, a precision phase shifter was added to provide for more accurate calibrations.

14. Testing Program

Each station, near the end of its reconfiguration period, was subjected to a series of configuration verification tests, system performance tests, and uncommitted *Pioneer* VIII tracks to establish its operational readiness.

F. Magnetic-Tape Logistics Support Program,

D. Lowell

1. Introduction

The tracking-and-data-acquisition magnetic tape needs of the projects served by the DSIF necessitate coordination. In January 1967, a program was initiated to perform this coordination. The prime objectives of the program are as follows:

(1) To ensure that all mission tape needs are met by proper tape deployment.

(2) To keep the purchasing of new tapes to a minimum.

Secondary objectives are as follows:

(1) To determine how many tapes were recorded for each mission.

(2) To ensure reliability of tapes that are reused.

(3) To determine the number of times a tape may be reused.

2. General Procedures

Analog instrumentation, digital, and video, are the three tape types most used by the DSIF. Normal analog instrumentation procedure is to record mission data on two tape recorders. One of these tapes, the prime tape, is then sent to the cognizant project. The other is held at the deep space station (DSS) pending notification that data on the prime tape have been processed. When notification has been received, the backup tape may be degaussed and reused. At the discretion of the project, prime tapes may also be released for reuse. Digital tape procedure is similar to that of analog instrumentation except that the digital backup tapes are often not made since the analog recording is usually the backup tape. All video tapes are sent to the project and are not reused.

Each time an analog instrumentation or digital tape is recorded, a sticker is placed on the reel for recording the number of times that a reel has been played. As long as a reel of tape does not leave a station, it may be used up to five times. Tape that has been used five times is automatically returned for recertification. Any used tape having obvious defects, such as tape stretching or excessive oxide binder shedding, is shipped to salvage.

Tapes sent to a project are subjected to a number of factors that may degrade tape reliability, such as:

(1) Handling in transit.

(2) Temperature in transit.

(3) The number of times that the tape must be played back to reduce the data.

(4) The aging of the oxide binder and polyester backing.

Therefore, any tapes released from a project for reuse are recertified before being placed in the DSIF supply system.

The recertification facilities are located at the Goldstone DSCC and JPL for the analog instrumentation and digital tapes, respectively.

Temperature-indicating decals are being placed on all tape ordered in 1968 to determine the maximum temperature that each reel is exposed to. Starting in December 1967, the Ames Research Center has provided data evaluation sheets on each reel of tape recorded for the *Pioneer* missions. Part of the evaluation provides information on tape dropouts. The evaluation sheets will be correlated with temperature information to determine the probable reliability of used tape.

3. Specific Utilization

a. Analog instrumentation tape. Tape usage varies with the mission requirements. Lunar missions require recording at high data rates. However, most lunar missions require less than 30 days of recording. Planetary missions have low data rates but may require years of recording. The DSIF presently records approximately 1,000 reels of analog instrumentation tape per month. Of these tapes, 40% are sent to the project and 60% are retained at the station as redundant recordings awaiting data verification of the prime tapes and degauss authorization.

The number of tapes recorded and the percentage of tapes sent to the project are expected to remain the same for the next several years, until the high-speed data lines are completed. Real-time data monitoring of the high-speed data lines will not be performed by project to validate data that has been received at JPL. At the end of each pass, tapes recorded at a deep space station will be played back to fill in missing data. After all possible data have been recovered, a degauss authorization will be given and there will be no need to ship tapes to the project.

b. Digital tape. The DSIF records two types of digital tapes: (1) telemetry and command processor (TCP), and digital instrumentation subsystem (DIS). The TCP format records spacecraft telemetry, whereas the DIS format records station parameters. Both tapes are presently shipped to JPL. When the high-speed data lines are completed and real-time data monitoring initiated, the TCP tapes will be handled like analog instrumentation tapes and used for fill-in data after the pass is completed. These tapes will be degaussed after all possible data have been recovered. The DIS station parameter tapes will continue to be shipped to JPL for analysis of DSS performance. The DSIF is presently recording 50 reels of digital tape per month in the DIS format. (Presently, the *Pioneer* mission does not use the TCP telemetry format. The next TCP telemetry format recording will be *Mariner* Venus 67 in November 1968.)

c. Video tape. The *Surveyor* and *Lunar Orbiter* were the only missions requiring a video-type tape recorder. Approximately 200 and 300 reels of video tape were recorded for each *Surveyor* and *Lunar Orbiter* mission, respectively. Completion of these lunar missions has ended video recording by the DSIF.

4. Inventory Control Methods

Three items are required in order to implement the magnetic-tape logistics support program: (1) the estimated project requirements, (2) the station tape usage projections, and (3) a report from the station on actual usage.

Estimated project requirements are made for 3- and 6-mo periods and updated every month. The 3-mo estimate is to permit shipping tape by sea freight and the 6-mo estimate is required for procurement.

Each DSS submits a monthly report indicating tape usage by project, the number of backup recordings awaiting project release authorization, and the number of reels available for recording. A comparison of the tape available and the estimated project requirements determines the quantity of tape to be shipped each month. The inventory part of the tape management program is being computerized and integrated into the DSIF logistics program.

G. Spare Parts Inventory Listing, *J. Manis*

A spare parts list, entitled "The Cognizant Operations Engineers Parts List" (COEPL), is being compiled at the Goldstone DSCC to facilitate allotment of spares by permitting provisioning at the system level instead of at the present subsystem level. The COEPL will list all spares (i.e., sets, assemblies, subassemblies, modules, and piece parts) used by the DSN repair depot and deep space stations to repair operational equipment. The COEPL will not list parts that are part of assemblies always repaired by a manufacturer.

The COEPL is compiled and maintained by the use of a data retrieval program and an SDS 900 series computer. The program offers a simplified data filing method and extremely flexible data formatting for retrieval. All data pertinent to a part is entered on a three-card series of format cards. Data for the COEPL is obtained from the cognizant operations engineers and from a variety of documents now used in lieu of a comprehensive parts list.

Approximately 4,000 parts have been listed to date. The COEPL will be put into effect when it contains enough information to effectively evaluate spares at the S-band system level.

VIII. Design and Implementation of Technical Structures and Utilities

A. Johannesburg DSS Antenna Mechanical Maintenance, *J. Carpenter*

Since the Johannesburg DSS will be used for *Mariner* Mars 1969 mission support, certain modifications were necessary to upgrade the station to the GSDS configuration and to improve reliability before the scheduled 1969 structural upgrade. Therefore, efforts were made to correct failure-prone areas in the hour angle drives, declination drives, cable wrapup, and dish surface.

The hour angle and declination drives had zero running clearance over two-thirds of the bull gear and total indicated readout (TIR) was out-of-tolerance by 0.160-in. maximum. To correct this condition, the drive pinions were moved apart and aligned to the center gear segments of the bull gear. The remaining segments were removed and reset to an average running clearance of 0.028 in.

To eliminate the danger of in-service cable failure, the cables were removed and new cable trays and wrapups were installed. This effort included running copper lines for the transmitter and air-conditioning chiller units.

After the surface reskinning was completed, the dish surface was optically checked and found to be 0.750 in. out-of-tolerance from a true parabola. This condition was corrected by shimming approximately half the panel attach points and resetting panel clips to an rms setting of 0.050 in. The overall rms value for the surface was set at under 0.085 in. Then the cassegrain cone attach ring, television package, and hyperbola were reset optically for the new dish surface. To restore structural integrity until the 1969 upgrade, rebolting of the structure with high-strength bolts was carried out, on a non-interference basis, in critical areas subject to such factors as joint stress reversals and high deceleration inputs.

B. Upgrade/Retrofit Projects for 85-ft HA–dec Antennas, *J. Carlucci, R. McKee, and W. Kissane*

The existing three-legged 85-ft hour-angle–declination (HA–dec) antenna structures at the Pioneer, Echo, Woomera, and Johannesburg DSSs are being upgraded/retrofit to meet the strength, stiffness, reliability, and configuration requirements imposed by the Mark II S-band tracking system. The upgrade/retrofit projects at the Echo and Woomera DSSs have been completed. The Echo DSS antenna is shown in its upgraded configuration in Fig. 1. The retrofit portion has also been completed at the Pioneer and Johannesburg DSSs. The upgrade portion at the Echo DSS is scheduled for completion by December 1968. The upgrade at the Johannesburg DSS is currently scheduled for completion during the period between September 1969 and January 1970.

Fig. 1. Echo DSS 85-ft antenna in upgraded configuration

The upgrade activities at the Echo and Woomera DSSs were as follows: The HA was extended from ±90 to ±96 deg. At the Echo DSS, a new high-performance S-band surface was installed with an overall rms setting of under 0.055 in. At the Woomera DSS, the existing L-band surface was reskinned and reset to an overall rms setting of under 0.085 in. (The surfaces at the Pioneer and Johannesburg DSSs will be the same as that at the Woomera DSS.) New HA and dec cable wrapup assemblies and tray runs, ladders and walkways, and stiffer adjustable drive skid mounts were installed. Rebolting with the new high-strength interference bolts and reinforcement of the structures were performed to obtain the required stiffness for pointing and sufficient strength to prevent structural failures of the type previously experienced due to current severe operational usages and high deceleration inputs.

The retrofit portion of the upgrade/retrofit projects included the installation of new two-level air-conditioned electronics rooms within the dec wheel, new HA and dec counterweight cage assemblies, new elevation bearings improved in strength and pointing-affecting tolerances, new truss-type quadripods, new cassegrain assemblies hardware, improved electro-optical group hardware, new servo group plumbing and hydraulic hardware, and all other required antenna mechanical support hardware.

C. Construction Progress at the Goldstone DSCC,

W. Lord and B. Sweetser

Occupancy by JPL personnel took place immediately after the on-schedule completion of the Mars DSS operations support building (Fig. 2) on August 12. The design of the building uses to advantage the sloping terrain at the Mars DSS. The building is two stories high on one side and one story high on the other, thus providing convenient ground-level access to both floors. The rectangular cable tunnel connects with the building such that the top of the tunnel may be used as a loading dock.

The cable room, mechanical equipment room, and a 20- × 48-ft communications room are located on the lower floor, and a 40- × 90-ft control room and four operations offices are located on the upper floor. Lightweight, but very stiff, fabricated trusses and removable floor panels were used in the construction of the control room. The control room is free of supporting columns. The cable room serves as a large plenum for air-conditioning the equipment racks placed over openings provided by the removable control-room floor panels.

D. Power System Modifications at the Mars DSS,

J. A. Barnet

Various modifications to the existing Mars DSS underground power distribution system are required at this time due to the recent completion of the operations support building and the installation of the high-power transmitter. All work is being performed on a noninterference basis to the mission-support schedule of the station.

With the existing system, power is supplied from two 2.4-kV sources: a commercial power substation owned by Southern California Edison Company and a JPL diesel-generator powerplant. Either commercial power "E" (electronics) and "U" (utility) or generator power "E" and "U" is selected by 2.4-kV selectivity switchgear for each of the site distribution circuits.

Fig. 2. Mars DSS operations support building

With the modifications, selective 2.4-kV circuits will serve the four 500-kV-A substations that provide either commercial "E" or "U" or generator "E" or "U" 480-V service to the operations building and the generator building. Circuits selected by the 2.4-kV selectivity switchgear will be distributed through an underground duct bank to the 2.4-kV high-power-transmitter switchgear. This switchgear will provide one circuit to the 3500-hp, 400-Hz high-power-transmitter motor-generator set and a second circuit to the 1500-kV-A substation. The 480-V secondary supply of this substation will serve the starter motor for the 3500-hp motor-generator set, the heat exchanger, and the auxiliary support equipment via distribution panels.

E. Advanced Power System Planning, *L. Kushner*

1. Introduction

Advanced DSIF power planning is directed toward the requirements of the proposed DSN Mark III system. This system will require 400+ kW of transmitter power, as compared to the 20-kW requirement of the Mark II system. The Mark III system is planned for implementation at the existing 210-ft-antenna Mars DSS and at the Robledo and Tidbinbilla DSSs following construction of the proposed 210-ft antennas at these stations.

2. Mars DSS Mark III System

The existing power demand at the Mars DSS is approximately 1500 kW. Four 500-kW diesel generators supply the required power during critical mission periods, and a commercial power substation supplies the power during non-critical mission periods. The proposed Mark III system will increase the power demand to approximately 5000 kW. It is planned to increase the capacity of the diesel-generator powerplant to 5750 kW (including a spare unit) for critical mission periods and the capacity of the commercial power substation (7500 kV-A) for non-critical periods.

The development of the Mark III system at the Mars DSS is planned on a non-interference basis to the mission-support schedule of the station. Mark II power generation and distribution systems will be used in their existing configuration and expanded where required to become a functional part of the Mark III system. The proposed additions for the Mars DSS Mark III system are shown in Fig. 3.

3. Robledo DSS and Tidbinbilla DSS Mark III Systems

A major factor under consideration for implementation of the Mark III system at the Robledo and Tidbinbilla DSSs once the proposed 210-ft antennas are constructed

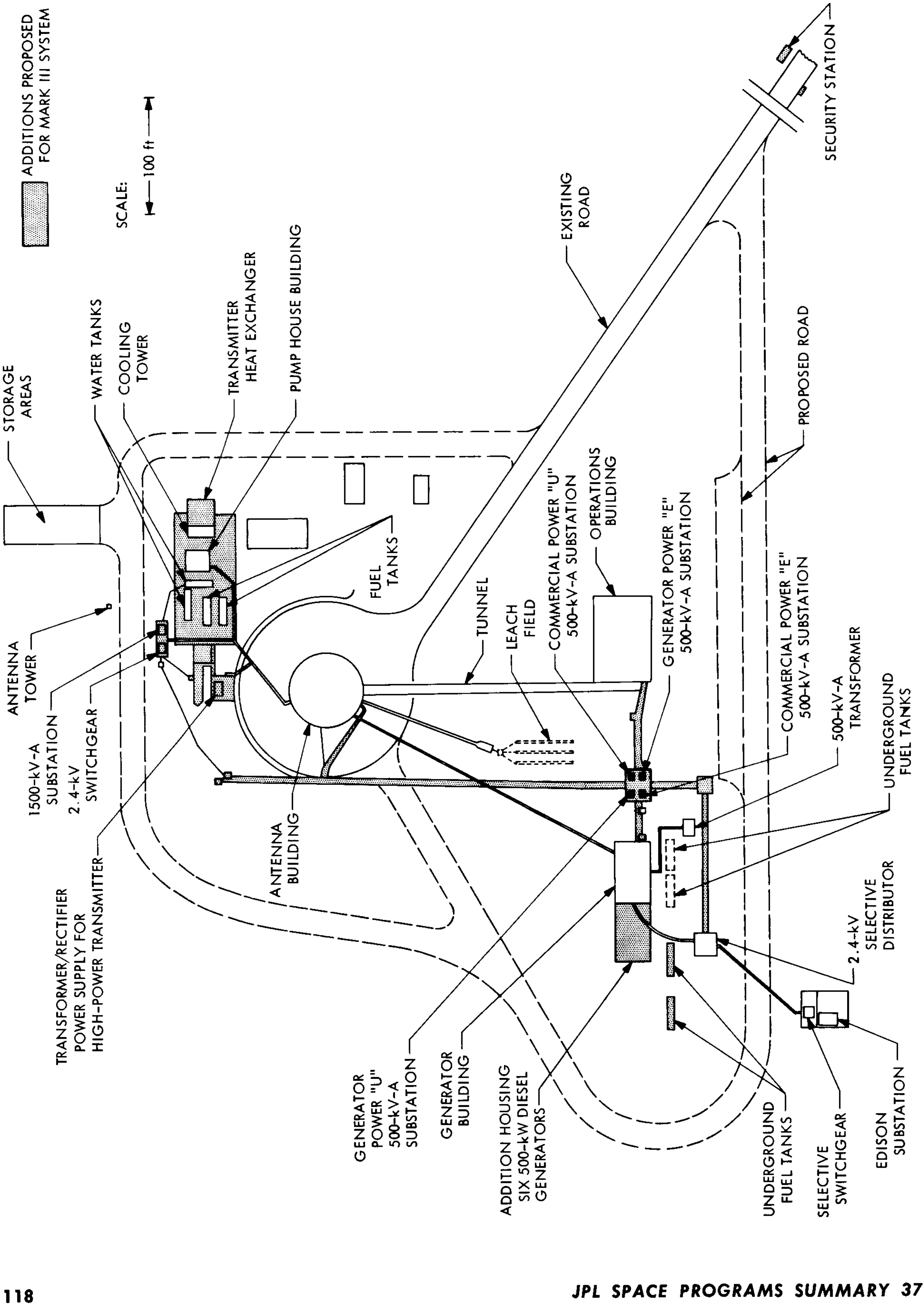

Fig. 3. Proposed additions for Mars DSS Mark III power system

is the integration of a 50-Hz commercial power service. The principal advantage would be the economy of the system, since the cost of commercial power is approximately one-tenth that of locally generated power.

All existing DSSs are oriented for 60-Hz power. The overseas 85-ft-antenna DSSs are served with 60-Hz power from local diesel-generator power plants during both critical mission periods and non-critical non-mission periods; no commercial power service is utilized. All DSSs within the United States have locally generated 60-Hz power during critical mission periods integrated with 60-Hz commercial power during all other periods. The average power demand for the 85-ft-antenna DSSs is approximately 600 kW.

Two schemes for the Mark III power system resulting from the advanced planning conducted thus far are discussed below:

a. Scheme 1. This study scheme provides for converting commercial power from 50 to 60 Hz and integrating it with locally generated 60-Hz power. Several modifications to the power systems concept for this scheme are refinements over the existing Mark II system and the Mark III system proposed for the Mars DSS.

A single-bus distribution system would be used instead of the more costly double-bus [electronics ("E") and utility ("U")] system. The single bus would use a single power service and provide transient isolation and regulation to sensitive electronics equipment by means of local regulators. The advantage of a single-bus system becomes evident when the amount of electronics power required for a DSS is compared to the overall Mark III power loads.

For the Mark II system, separate power generation bus and distribution systems for the electronics equipment and the utilities were necessary because the electronics equipment load represented approximately 23% of the station power requirements (70 kW out of 310 kW total). The electronics equipment load for the Mark III system would represent approximately 2% of the station power demand (90 kW out of 5090 kW total).

b. Scheme 2. This scheme is a modification of the powerplant concept for scheme 1. During critical-mission periods, the 50-Hz service would originate from a local powerplant. Two-speed generator units have been considered for the powerplant: one speed for 60-Hz loads and the other speed for 50-Hz loads (including the 3500-hp high-power-transmitter motor-generator power supply). Selective switching would permit transfer of the units between the 60-Hz and 50-Hz busses. Selective switching would also be used for transfer to commercial power during non-critical periods and to generated power during critical periods.

An additional consideration was the use of the commercial power service as backup to the local powerplant during critical mission periods. This would require parallel operation of the powerplant with the commercial power service, using an induction-type voltage regulator for load adjustment between generated power and commercial power.